Manipulating Microbubbles: Steering Ultrasound Contrast Agents Using Acoustic Radiation Forces

Alicia Clark

A dissertation
submitted in partial fulfillment of the
requirements for the degree of

Doctor of Philosophy

University of Washington

2018

Reading Committee:

Alberto Aliseda, Chair

Michalakis Averkiou

Nathan Sniadecki

Program Authorized to Offer Degree:
Mechanical Engineering

University of Washington

Abstract

Manipulating Microbubbles: Steering Ultrasound Contrast Agents Using Acoustic Radiation Forces

Alicia Clark

Chair of the Supervisory Committee:
Dr. Alberto Aliseda
Mechanical Engineering

Ultrasound contrast agents are micron-sized bubbles that are used for ultrasound imaging enhancement and that can potentially be used for targeted drug delivery applications. One strategy to manipulate them inside the cardiovascular system is to use the Bjerknes force, caused by the phase difference between a transmitted ultrasound pressure wave and the microbubble volume oscillations induced by the pressure wave. Although the mechanism causing this force is well established, the balance between ultrasound-induced forces and hydrodynamic forces is poorly understood when the microbubbles are immersed in physiologically-realistic Reynolds and Womersley number flows. In this thesis, experiments were conducted in a cylindrical tube under steady and pulsatile flows over a range of Reynolds and Womersley numbers relevant to drug delivery in the systemic circulation. Two experimental setups were developed: one in which the microbubbles were imaged using a clinical ultrasound imaging system, and a second in which they were imaged by high-speed video using a long distance microscope. In the ultrasound experimental setup, a commercial L15-7io transducer was used to image microbubbles in quiescent, steady, and pulsatile flows. These experiments were extended in the optical experimental setup to explore higher Reynolds numbers. In the optical experiments, individual microbubble trajectories were captured at high magnification and high temporal resolution to determine the relationship between acoustic and

hydrodynamic forces. The relative scaling of these forces was computed for different acoustic pressure amplitudes and pulse repetition frequencies. The Bjerknes force scaled linearly with pulse repetition frequency and quadratically with acoustic amplitude. The displacement of the microbubbles due to the ultrasound decreased with increasing Reynolds number suggesting a threshold for clinical applications due to the residence time of microbubbles in the ultrasound beam.

TABLE OF CONTENTS

LIST OF FIGURES

LIST OF TABLES

ACKNOWLEDGMENTS

I would like to thank my advisor Dr. Alberto Aliseda for his help and guidance throughout my dissertation research. His extensive knowledge of fluid mechanics has always inspired me and instilled in me a great excitement for the topic.

I would like to thank Dr. Michalakis Averkiou for being a ‘second’ advisor to me during the last year of my PhD. He helped me learn the basic principles of ultrasound and encouraged me to focus on the fundamentals first. He also welcomed me into his lab and allowed me use of their equipment for my final experiments. His passion for ultrasound is truly inspiring.

I would like to thank Dr. Matt Bruce for serving as a mentor during the last couple years of my dissertation. Working together with you in the lab was the first time I got to use an ultrasound system, and I will always thank you for that.

I would like to thank Dr. Thomas Matula for introducing me to the ultrasound community at the University of Washington. His passion for research and innovation is evident.

I would like to thank Drs. Nathan Sniadecki and Nirnimesh Kumar for serving on my dissertation committee. Their advice and support throughout my dissertation has been very helpful.

I would also like to thank the National Science Foundation Graduate Research Fellowship Program for supporting my throughout the first couple years of my research. It gave me the freedom and flexibility to participate in multiple lab projects which instilled in me a great love of research.

Finally, I would like to thank all of my family, friends, and labmates for supporting me along this very long journey. I would not be where I am today without having each and every one of you.

DEDICATION

To my family and friends and everybody else who has supported me throughout this journey.

Chapter 1

INTRODUCTION

Ultrasound (US) is a safe and noninvasive real-time imaging methodology commonly used in medical applications due to its low cost and availability. However, there are tissues within the human body where low contrast makes it difficult to obtain ultrasound images that are valuable for diagnostics. This limitation has led to the development of lipid-coated gas microbubbles that can be injected into the circulation to increase the contrast in ultrasound images. These microbubbles, with diameters between 1 and 10 μm, are known as ultrasound contrast agents (UCAs). Besides increasing contrast, microbubbles can be used in a wide range of clinical applications which will be introduced throughout this chapter.

The scattering produced by the microbubbles increases the signal-to-noise ratio at the US receiver due to the large impedance difference between the microbubbles and the surrounding tissue [39]. Figure 1.1 shows a set of ultrasound images of the liver taken at different times before and after injection of UCAs. The left image shows the liver imaged using only US and no microbubbles. It is apparent that there are two liver lesions, but the contrast in the image is too low to determine the type of lesions that are present. The center image shows the liver imaged after microbubbles have been injected into the bloodstream. The liver lesions are now more clearly delineated. Finally, the right image, taken at a later time, shows the accumulation of microbubbles in the liver region. With the help of microbubbles, the types of the liver lesions can be readily identified. This image sequence demonstrates the use of microbubbles in clinical settings.

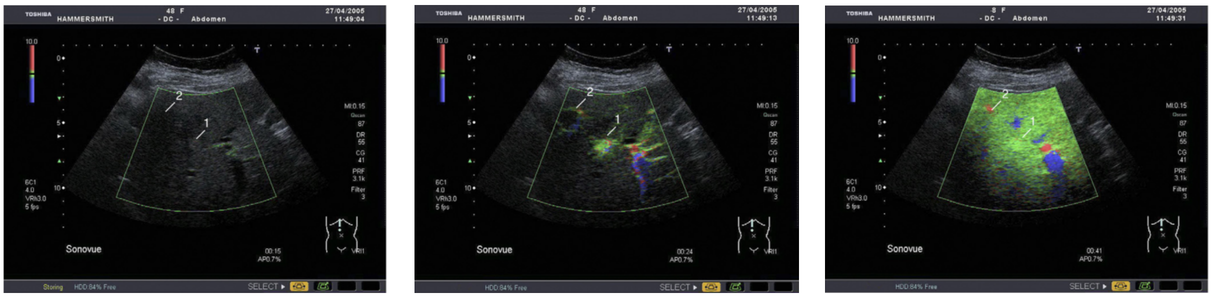

(a) (b) (c)

Figure 1.1: Ultrasound imaging of the liver at three different times: (a) US only, (b) microbubbles first introduced into the bloodstream, and (c) accumulated microbubbles at a later time (Reprinted from [19] with permission from Elsevier).

1.1 Therapeutic Applications of Ultrasound Contrast Agents

The use of microbubbles combined with US has many potential therapeutic applications, such as cancer chemotherapy, temporarily opening the blood brain barrier (BBB), thrombolysis, and targeted drug delivery [86]. We will focus on thrombolysis and targeted drug delivery since they are more relevant to the scope of this research. In both of these UCA applications, the Bjerknes force (produced due to the phase lag between the fluctuating US pressure waves and the microbubble volume oscillations) is manipulated to steer the microbubbles towards a targeted area.

The mechanical index (MI) is a metric used to define the potential for harmonic pressure waves to induce inertial cavitation [80]. Increasing MI can lead to exceeding a threshold where significant bioeffects, mechanical or thermal, therapeutic or pathologic, can be present. It is defined as:

$$MI = \frac{PNP}{\sqrt{f_c}} \tag{1.1}$$

where PNP is the peak negative pressure in MPa and f_c is the center frequency in MHz of the pressure wave. At low MI (less than 0.05), the microbubble oscillates in the linear regime with small amplitudes and scatters sound mostly at the transmitted frequency. At slightly higher MI (between 0.05 and 0.1), the microbubble becomes more resistant to compression than to expansion (non-inertial cavitation). The oscillations of the microbubble are in the nonlinear regime in this MI range. Finally, at higher MI (between 0.3 and 0.6), the microbubble undergoes forced expansion and compression. This leads to inertial cavitation [34]. It is important to note that the above operating ranges can be reached using clinically-available ultrasound frequencies and intensities, since they are well below the Food and Drug Administration (FDA) limit (MI $<$ 1.9). Figure 1.2 shows the oscillation of a 3 μm bubble due to the introduction of an US pressure field. Due to the high mechanical index of the US in this image sequence, the microbubble oscillates in size and then implodes due to the fluctuating pressure as time progresses during the excitation (frames E and F).

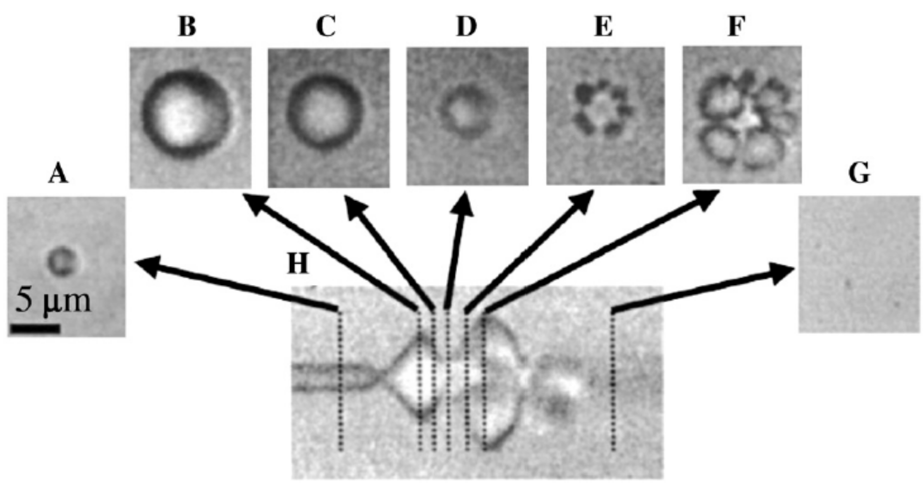

Figure 1.2: Streak image showing the oscillation of a 3 μm bubbles (image A) over time. The dash lines correspond to the above images showing the changes in the bubble (Reprinted from [34] with permission from Elsevier).

Figure 1.3 shows how a microbubble responds to different center frequencies (and thus MIs). The MI is higher for the 1.5 MHz transducer, since the MI is inversely proportional to the square root of the US center frequency, and, therefore, inertial cavitation of the microbubble occurs (refer to image 3). At the lower MI (3.5 MHz), however, the microbubble oscillates in size but does not undergo inertial cavitation. The MI of excitation is a very important consideration in both targeted drug delivery and thrombolysis, as it determines the safety of the insonation and therefore strongly correlates with the translational potential of a specific strategy for biomedical research.

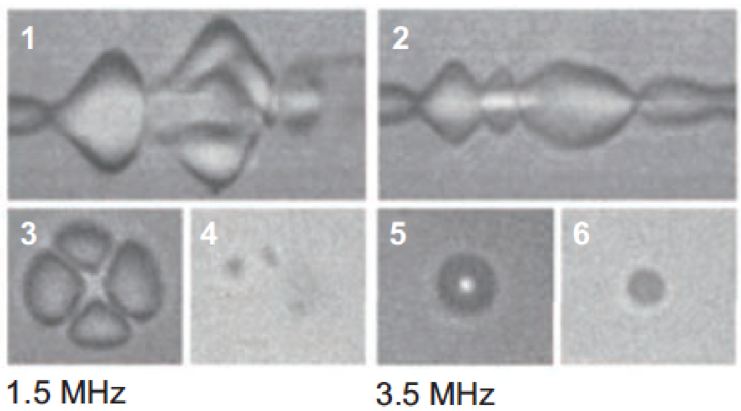

Figure 1.3: Streak images showing the change in microbubble size over time: (1) and (2). Images (3) and (5) show the peak expansion of the microbubble. Images (4) and (6) show the remnants of the microbubble after the end of ultrasound insonation. Images are shown at center frequencies of 1.5 MHz and 3.5 MHz (Republished with permission from [30]; permission conveyed through Copyright Clearance Center, Inc.).

1.1.1 Thrombolysis

A promising application of UCAs is thrombolysis, or the destruction of a thrombus using microbubbles and thrombolytic drugs. When a branch of a bifurcation is occluded, it is very difficult to deliver drugs to the occluded area. The use of US, in combination with drug-loaded microbubbles, can help increase the speed of drug delivery since the drug-coated UCAs can be directed towards the thrombus by steering them through the Bjerknes force (at a clinically-acceptable MI between 0.05 and 0.3). Additionally, the microbubbles can be used to help destroy the thrombus at a higher MI. Once the UCAs are in the occluded region, the mechanical index (MI) of the ultrasound can be increased, leading to the collapse of the microbubbles at the site of the thrombus through inertial cavitation, with dispersal of the thrombolytic drug loaded onto the bubble coating [22]. In addition to delivering the anti-thrombolytic drug, the cavitation of the microbubbles produces a high speed jet (up to 700 m/s) that helps to break up the fibrin mesh that gives a thrombus its mechanical toughness. Inertial cavitation of UCAs can also increase the permeability of the thrombus tissue to allow thrombolytic drugs to penetrate deep into the thrombus.

Additionally, US and UCAs can be used to accelerate the transport and penetration of tissue plasminogen activator (tPa) into the thrombus. Molina et al. [55] observed that using US together with UCAs leads to vessel recanalization more frequently than tPA with US or UCAs alone, suggesting that thrombolytic drug may not be necessary in the destruction of the thrombus. This would be beneficial because tPa has been known to lead to hemorrhagic stroke and GI bleeding, among other complications.

1.1.2 Targeted Drug Delivery

Another promising application of UCAs is targeted drug delivery [4, 26, 28, 34, 41, 48]. The use of UCAs and tPa, discussed in the thrombolysis section above, gives a brief example of how UCAs can assist in delivering drugs to a targeted area. We can now look at the mechanisms used in targeted drug delivery. First, it is very important to consider how the microbubbles will be used to transport the drugs. The drug can be injected into the bloodstream in saline solution along with the microbubbles (if it is soluble in water), it can be binded to the microbubble lipid coating (if it is soluble in lipids), or it can be loaded inside the microbubbles if it can be aerosolized in the microbubble gas content. Figure 1.4 shows these and other methods that can be used to transport drugs to the targeted region.

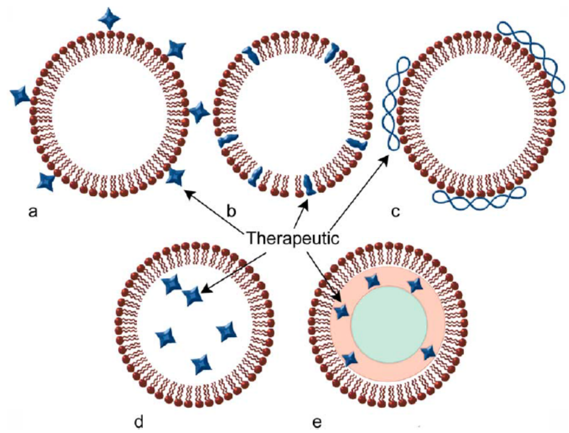

Figure 1.4: Different ways that microbubbles can be used to transport drugs. (a) Drugs are attached to the microbubble membrane, (b) drugs are embedded within the membrane, (c) materials such as DNA are covalently-bonded to the microbubble coating, (d) microbubbles are loaded with drugs or gas, and (e) hydrophobic drugs are dissolved into the lipid film that coats the microbubble (Reprinted from [86] with permission from Elsevier).

Figure 1.5 shows how these different methods can be used to help deliver thrombolytic drugs. The image to the left shows freely circulating microbubbles and drugs in the vessel. US is used to force the microbubbles to cavitate, which increases the permeability of the arterial wall (sonoporation). Drugs can then easily pass through the intima layer of the vessel wall to treat the targeted tissue inside the vessel wall or a nearby organ fed by this vessel. The center images show drug-loaded microbubbles inside a blood vessel. As the microbubbles are destroyed by cavitation, they release drugs into the vessel. The drugs are delivered locally. Finally, the images on the right show microbubbles that contain surface ligands which can bind to specific endothelial cell receptors. The microbubbles bind and accumulate in the targeted region of the vessel. The bubbles are then forced to cavitate and release the drugs that had been loaded onto them.

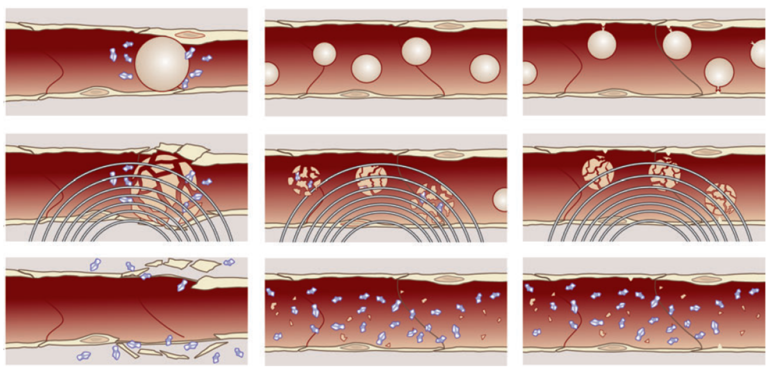

Figure 1.5: Use of microbubbles to deliver drugs in vessels. (Left) freely circulating microbubbles and drugs, (Center) microbubbles loaded with drugs, and (Right) microbubbles with surface ligands to bind to specific endothelial cell receptors (Republished with permission from [30]; permission conveyed through Copyright Clearance Center, Inc.).

Targeted drug delivery uses the Bjerknes force (MI between 0.1 and 0.3) to steer the microbubbles to the targeted area. When the microbubbles have reached the targeted area, the amplitude of the US can be increased to cause inertial cavitation of the microbubbles due to the increased energy deposited on the microbubbles by the US pressure. The cavitating bubbles can then increase the permeability of the vessel walls so drugs can be transported across the endothelial barrier to the vessel wall and surrounding tissue.

1.2 Research Problem

Previous research has focused on exploring the dynamics of bubbles under ultrasound excitation in a stagnant fluid, whether in an infinite domain (a large water tank) or next to a wall in strong confinement (in a capillary blood vessel). However, **there has not been**

much attention to research conducted to explore the dynamics of microbubbles in vessels at physiologically-realistic flow rates. Some interesting questions arise when looking at how microbubbles will behave in high Reynolds number physiologically-realistic flows under the influence of strong, non-linear hydrodynamic forces:

- How do the dynamics of microbubbles under ultrasound excitation change when there is inhomogeneous (sheared) and pulsatile flow around them (in millimeter-scale or larger vessels)?

- How do we properly model the interaction between the microbubbles and the flow around them, specifically the coupling of volume oscillations with hydrodynamic lift and drag?

- Do the ultrasound-induced forces have the ability to modify microbubble trajectories, overcoming the dominance of drag and altering lift, to transport microbubbles towards the vessel walls or a specific branch in a bifurcation?

This thesis primarily focuses on the dynamics of the microbubbles in high Reynolds and Womersley number flows, under the influence of ultrasound within clinical frequencies and intensities (low MI), to gain a greater understanding of the dynamics of microbubbles in conditions similar to those found in the human circulation under drug delivery conditions.

Chapter 2

REVIEW OF RELATED RESEARCH

2.1 Linear Oscillator

An initial model of the behavior of microbubbles can consist in treating microbubbles as linear oscillators, with inertia, damping, and an elastic restoring force. Historically, this brought a significant improvement in our understanding of bubble acoustics. Early models created to study both the undamped and damped behavior of a gas bubble used the bubble gas pressure/density relationship in the ideal gas law, surface tension, and liquid density and viscosity; heat transfer, gas and liquid compressibility, gas and vapour mass transport, etc. were additionally considered as modern models became more refined in the last fifty years (such as [20, 21, 27, 52, 57, 61, 70, 72, 73, 75] and references within). Here, the undamped model developed by Minnaert [54] is first described because it produced a very good approximation for the resonant frequency of an uncoated microbbuble, introducing important concepts that represent a useful starting point for future interpretation of our experimental work [45].

2.2 Undamped Linear Oscillator

Minnaert [54] extended the work of Lord Rayleigh [75] on the dynamics of a void cavity in a liquid to be the first to predict the natural frequency of a spherical gas bubble in a liquid undergoing small-amplitude simple harmonic motion. His calculations assumed:

- Spherical gas bubbles
- Negligible heat conduction and radiation

- Negligible surface tension

- Inertia only in motion of water (not in the gas motion inside the bubble)

- Incompressible liquid

- Uniform pressure for the gas inside the bubble (infinitely small Mach number for the gas motion inside the bubble)

Equation 2.1 shows the predicted *Minnaert resonance frequency*:

$$f_{res} = \frac{1}{2\pi}\frac{1}{R_0}\sqrt{\frac{3\gamma P_o}{\rho_l}} \tag{2.1}$$

where f_{res} is the resonance frequency of the bubble oscillations, R_0 is the equilibrium radius of the bubble, γ is the ratio of specific heats for the gas, P_0 is the ambient pressure, and ρ_l is the density of the surrounding fluid. For air bubbles in water at an ambient pressure of approximately 1 atmosphere, Equation 2.1 can be simplified to:

$$f_{res} = \frac{1}{2\pi}\frac{1}{R_0}\sqrt{\frac{3\gamma P_{air}}{\rho_{water}}} \approx \frac{3[MHz]}{R_0[\mu m]} \tag{2.2}$$

It is important to note that this result, limited as it is by the assumptions described above (negligible surface tension, heat conduction, viscosity, compressibility, etc), is still very useful because it provides a quick approximation of the value for the resonance frequency of different size bubbles. This represents a reliable starting point for determining the ultrasound frequency that will be most effective at steering microbubbles due to the primary Bjerknes force. Table 2.1 shows an example of resonance frequency values for uncoated microbubbles in the size range of UCAs.

Bubble Diameter (μm)	Resonance Frequency (MHz)
1	6.00
2	3.00
3	2.00
4	1.50
5	1.20
6	1.00
7	0.86
8	0.75
9	0.67
10	0.60

Table 2.1: Resonance Frequency at Different Bubble Diameters

2.3 Nonlinear Equations for Pulsating Bubbles

Linear models give a good first approximation of the dynamics of a microbubble; however, nonlinear models need to be developed to better understand and more accurately predict the behavior of microbubbles under strong non-linear effects, such as surface tension, surface viscosity in the coating layer, large amplitude deformation close to resonance, etc. When the behavior of the bubble is nonlinear, the expansion and compression of the bubble are not symmetric when the bubble is subjected to a harmonic ultrasound pressure field. The Rayleigh-Plesset equation is the most commonly-used starting point for nonlinear dynamics governing the time evolution of a bubble under volume (spherically-symmetric) oscillations.

2.3.1 Rayleigh-Plesset Equation

The Rayleigh-Plesset equation was developed through the work of Plesset [70], from the seminal work of Rayleigh. Later, it was extended by Noltingk and Neppiras [61], Neppiras and Noltingk [57], and Poritsky [72], generalizing some of the simplifying assumptions made by the two original authors. The extended equation, commonly referred to as the RPNNP equation, for the bubble radius $R(t)$ and its time derivatives is shown in Equation 2.3:

$$\rho_l \left(R\ddot{R} + \frac{3\dot{R}^2}{2} \right) = \left(P_0 + \frac{2\sigma}{R_0} - P_v \right) \left(\frac{R_0}{R} \right)^{3\kappa} - \frac{2\sigma}{R} - \frac{4\mu\dot{R}}{R} - P_\infty - P\left(t, z\right) \tag{2.3}$$

where:

- $\rho_{liq} \left(R\ddot{R} + \frac{3\dot{R}^2}{2} \right)$ represents the inertia of the liquid on the surface of the bubble (mass times acceleration and kinetic energy, per unit surface),

- $\left(P_0 + \frac{2\sigma}{R_0} - P_v \right)$ represents the initial pressure inside the bubble, where σ is the surface tension and P_v is the vapor pressure,

- $\left(\frac{R_0}{R} \right)^{3\kappa}$ represents the polytropic expansion term that gives the ratio of actual over initial pressure inside the bubble, as a function of the bubble radius. κ is the polytropic expansion coefficient of the gas inside the bubble where $\kappa = 1$ for a constant bubble temperature and $\kappa = \gamma$ for an adiabatic process,

- $\frac{2\sigma}{R}$ represents the effects of surface tension,

- $\frac{4\mu\dot{R}}{R}$ represents the viscous stress in the liquid on the surface of the bubble, where μ is the viscosity of the surrounding fluid,

- P_∞ represents the hydrostatic pressure far from the bubble,

- $P(t, z)$ represents the pressure excitation (ultrasound pressure wave propagating through the liquid).

The predictions from the Rayleigh-Plesset equation for small amplitude volume oscillations can be obtained from linearization of the equations for a harmonic response out of phase with the harmonic excitation. Two limits can be established from the linearized solution: when surface tension is negligible and when surface tension dominates.

- Small Amplitude Behavior

  The resonance frequency of the bubbles can be predicted from the Rayleigh-Plesset equation for small amplitude behavior when surface tension is negligible:

  $$f_0 = \frac{1}{2\pi}\frac{1}{R_0}\sqrt{\frac{3\kappa P_0}{\rho}} \tag{2.4}$$

  This result matches the solution developed by Minnaert, except it does not make the assumption that the bubble behaves adiabatically [45]. Thus, the frequency depends on the polytropic expansion coefficient (κ); here κ replaces the ratio of specific heats for the gas, γ.

- Surface Tension Dominates

  The resonance frequency of the bubbles can also be predicted by Equation 2.3 when the surface tension dominates. Under normal atmospheric conditions, and for surface tension between air and water, the size of the bubbles must be $< 5\ \mu$m in order for surface tension to dominate.

  $$f_0 = \frac{1}{2\pi}\frac{1}{R_0\sqrt{\rho}}\sqrt{3\kappa\left(P_0 + \frac{2\sigma}{R_0} - P_v\right) - \frac{2\sigma}{R_0} + P_v - \frac{4\mu^2}{\rho R_0}} \tag{2.5}$$

  This result now includes the effects of surface tension and viscosity.

The Rayleigh-Plesset equation is very useful for modeling nonlinear bubble oscillations; however, the model starts to break down when the bubble is driven near its resonance frequency.

Crum and Prosperetti [20] experimentally predicted the behavior of bubbles for three different gases with a wide range of polytropic values. They found that their experimental results matched fairly well with theoretical predictions when the bubble was not oscillating near its resonance frequency; however, they suggested that the RPNNP model needs to be modified to account for large amplitude pulsations of the bubble near resonance. The Rayleigh-Plesset equation has difficulty predicting a bubble near its resonance frequency due to the following assumptions:

- First, the RPNNP assumes that the liquid is incompressible. When the bubble oscillation amplitude is large, the compressibility of the liquid can no longer be ignored.

- Next, the assumption that the behavior of the gas inside the bubble can be modeled as polytropic is no longer valid. At large oscillation amplitudes, the polytropic assumption does not accurately account for the energy losses due to the heating and cooling of the gas.

- Finally, the assumption that the bubble is always spherical is not good because the bubble can become unstable at large oscillation amplitudes, and lose its spherical symmetry when higher order deformation modes are excited [29].

2.4 Dynamics of Microbubbles in Microvessels

The research work described above focused on the dynamics of bubbles in infinite domains; however, the resonance frequency of microbubbles is strongly affected by the surrounding media. Therefore, to understand the behavior of microbubbles and UCAs under large amplitude volume oscillations inside the blood vessels, as is required to predict the steering of microbubbles by ultrasound-induced forces in medical applications, it is necessary to study the oscillation of microbubbles in cylindrical confinement (inside a tube).

Oguz and Prosperetti [62] first presented a numerical study on the natural frequency of gas bubbles inside a liquid-filled, finite-length, rigid-walled tube. The bubble diameter was small compared to the tube diameter, as is the case of interest in this study where we focus on large arteries with diameters of the order of millimeters or larger. Oguz and Prosperetti determined that viscous dissipation in the liquid flow along the tube surface can not be considered negligible and that viscous losses are significant for bubbles smaller than 10 μm.

Sassaroli and Hynynen [76] also presented a numerical model to predict the resonance frequency and damping of microbubbles in blood vessels. They determined that the natural frequency of the microbubbles is not only dependent on the bubble radius but also on the parameters of the blood vessel such as radius and length. They also showed that the resonance frequency in small blood vessels is lower than predicted in a free-bubble model. This suggests that ultrasound can potentially be used in a range of frequencies lower than the frequencies currently used in therapeutic and diagnostic applications for UCAs between $1-6$ μm (such as those approved for injection into the human vasculature).

While the studies by Oguz and Prosperetti [62] and Sassaroli and Hynynen [76] have been insightful, they do not capture the dynamics of a microbubble in non-rigid vessels. Qin and Ferrara furthered their work by looking at the behavior of microbubbles in compliant vessels [74]. They developed a lumped-parameter model to study the effects of compliant microvessels on microbubble behavior. They modeled the problem in COMSOL using an axially symmetric Navier-Stokes model. They looked at the behavior of microbubbles in two different size vessels: 8 μm and 40 μm.

For the larger 40 μm vessel, the results agree well with the results obtained from the Rayleigh-Plesset equation. This is to be expected since the microbubble diameter is much smaller than the vessel diameter; in this case, the vessel wall effects do not significantly affect the dynamics of the microbubbles. However, in the 8 μm vessel, the effects of the vessel walls are immediately apparent. The oscillation amplitude decreases in the smaller vessel and the oscillation amplitude following the driving cycle (~ 1 μs) is reduced by 67.8%. This is a significant reduction, which shows that there is need for better numerical models of bubble oscillations in small microvessels. It was also observed that the oscillation frequency increases in smaller microvessels. The oscillation frequency of a 3 μm diameter bubble was found to be 2.73 MHz in the 40 μm vessel and 3.17 MHz in the 8 μm vessel. Additionally, Qin and Ferrara also determined that the viscosity of the liquid has a larger effect on oscillation amplitude (due to viscous damping) in smaller vessels than in larger vessels.

2.5 Dynamics of Microbubbles in Blood

Little work has been done examining the dynamics of microbubbles in blood, which is potentially important for future clinical applications. Owen et al. [66] performed experiments in a 200 μm tube to exam the targeting efficiency of magnetic microbubbles in both saline and whole blood. Their experiments did not use ultrasound to steer the microbubbles, but they instead used a magnetic field to attract the microbubble towards the tubing wall. They showed that less microbubbles are able to accumulate near the tubing wall (due to the magnetic force) in blood than in saline, which they suggest is due to the presence of cells in the blood that act to impede microbubble motion. Other studies have also shown that the concentration of red blood cells (hematocrit) in the blood can alter the targeting efficiency of microbubbles [14, 56]. Finally, studies have considered the effectiveness of targeting based on the relative size of the microbubbles to the red blood cells, showing that microbubbles that are approximately 2 μm in diameter are more effective in targeting applications[12, 13, 56]. Targeting was also shown to increase in pulsatile blood flow versus blood flow that was steady.

The limited amount of research done on this topic suggests the importance of the research performed in this dissertation. While we do not directly explore the dynamics of microbubbles in blood, we introduce a framework to further explore the behavior of microbubbles in physiological vessels using clinical ultrasound technology. This will enable further understanding of the interaction between microbubbles and blood cells and determine effective clinical strategies moving forward. This dissertation shows that the concentration of microbubbles, as well as the size of the blood vessel these microbubbles are traveling in, is extremely important for ultrasound steering applications, and we hypothesize that this will be also true *in vivo*. As shown in [66], it is expected that microbubble dynamics in blood will be more interesting in smaller vessels, where the blood behaves with non-Newtonian rheology and the vessel wall interferes with the oscillations of the microbubbles. However, minimal effect of surrounding cells is expected in larger vessels, the focus of this dissertation.

2.6 Bjerknes Force

The presence of a force acting on bubbles due to a harmonic pressure field (acoustic radiation force) was first proposed by Bjerknes [6]. The Bjerknes force occurs due to the phase difference between the incoming ultrasound pressure field and the volume oscillations of the bubble induced by the US. Eller [27] proposed an expression for the Bjerknes force acting on a bubble in a standing acoustic wave. He showed that a bubble with a diameter larger than the value of the resonant diameter will experience a force towards the pressure nodes in a standing wave, whereas a bubble with a smaller diameter will be forced towards the pressure antinode. Figure 2.1 shows the working of this mechanism with a sketch.

The primary Bjerknes force is defined as the net force, time-averaged over a cycle of the ultrasonic pressure excitation, acting on the bubble.

$$F_{Bjerknes} = \langle V(t) \nabla P(r,t) \rangle \tag{2.6}$$

where $V(t)$ is the bubble volume and $\nabla P(r,t)$ is the pressure gradient acting on the volume.

An analytical expression for this force can be derived using a standing wave field. The pressure field can be defined as:

$$P(y,t) = P_\infty + 2P_A sin(ky) cos(\omega t) \tag{2.7}$$

where P_∞ is the hydrostatic pressure as defined above, P_A is the amplitude of the pressure wave, $k = \frac{2\pi}{\lambda}$ is the wave number, λ is the wavelength, and $\omega = 2\pi f$ is the angular frequency. The gradient of the pressure field is taken, to obtain:

$$\nabla P(y,t) = 2kP_A cos(ky) cos(\omega t) \tag{2.8}$$

Radial oscillations are defined as a function of time assuming that $2P_A \ll P_\infty$:

$$R(t) = R_0 - \xi cos(\omega t + \alpha) \tag{2.9}$$

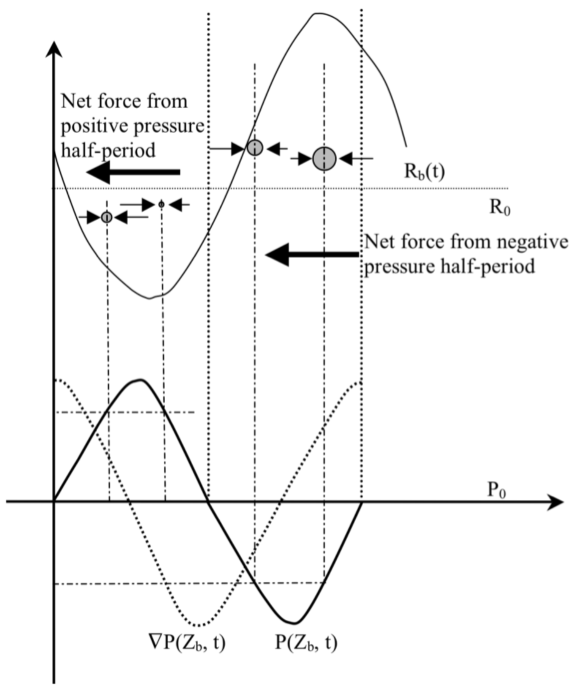

Figure 2.1: Sketch of the mechanism responsible for the Bjerknes force in a standing wave for a bubble larger than the resonant diameter for the frequency of excitation. The net force, over each half period, is shown in the direction of propagation of the wave (towards the pressure antinodes in a standing wave).

where R_0 is the equilibrium radius of the bubble, ξ is the amplitude of the radial oscillations which we assume to be $\ll R_0$, and α is the phase of the oscillating radius.

The volume can now be defined as:

$$\begin{aligned} V(t) &= \tfrac{4}{3}\pi R(t)^3 \\ &= \tfrac{4}{3}\pi \left(R_0 - \xi cos(\omega t + \alpha)\right)^3 \end{aligned} \tag{2.10}$$

where $\xi = \xi_0 sin(ky)$. A first-order approximation of the above equation gives:

$$\begin{aligned} V(t) &= \tfrac{4}{3}\pi R_0^3 - \tfrac{4}{3}\pi R_0^3 \left[\big(3\xi_0\big)/\big(R_0 sin(ky) cos(\omega t + \alpha)\big)\right] \\ &= V_0 \left(1 - \tfrac{3\xi_0}{R_0} sin(ky) cos(\omega t + \alpha)\right) \end{aligned} \tag{2.11}$$

The Bjerknes force can be solved for by substituting equations 2.8 and 2.11 into 2.6.

$$F_{Bjerknes} = \left\langle \left(V_0 \left(1 - \frac{3\xi_0}{R_0} sin(ky)cos(\omega t + \alpha) \right) \right) \left(2kP_A cos(ky)cos(\omega t) \right) \right\rangle \tag{2.12}$$

For bubbles smaller than the resonance size ($\alpha = 0$), we obtain:

$$F_{Bjerknes} = \frac{3P_A k \xi_0 V_0 sin(2ky)}{2R_0} \tag{2.13}$$

For bubbles larger than the resonance size ($\alpha = \pi$), we obtain:

$$F_{Bjerknes} = -\frac{3P_A k \xi_0 V_0 sin(2ky)}{2R_0} \tag{2.14}$$

The force is positive when α is between 0 and $\pi/2$, and negative when α is between $\pi/2$ and π. Equations 2.13 and 2.14 give the expression for the Bjerknes force in a standing wave field for bubbles smaller and larger than the resonance size. Bubbles larger than the resonance size will travel towards the pressure nodes of the standing wave; whereas, bubbles smaller than the resonance size will travel towards the pressure antinodes (as evidenced by the difference in sign in the above equations).

The force can be evaluated similarly in a traveling wave (derivation shown in [24]) to yield:

$$F_{Bjerknes,trav} = \frac{2\pi P_A^2 D R_0}{\delta_{tot} \rho_0 c \omega_0 T} \tag{2.15}$$

where D is the duration of the transmitted pulse, δ_{tot} is the damping constant, ρ_0 is the density of the surrounding fluid, c is the speed of sound in the surrounding fluid, ω_0 is the resonant frequency of the bubble, T is the pulse repetition period (the reciprocal of the pulse repetition frequency), and P_A and R_0 are the same as described previously. This equation gives insight into the scaling of the Bjerknes force, which is useful for the experiments addressed in this thesis. The Bjerknes force varies linear with both pulse duration and pulse repetition frequency (and thus the duty cycle) and quadratically with the pressure amplitude. Additionally, the bubbles are displaced away from the ultrasound transducer; they do not travel towards pressure nodes and antinodes as in the standing wave field.

Finally, for completeness, the incoming ultrasound pressure field causes the bubbles to oscillate, which alters the local pressure field around the bubbles. This produces a secondary Bjerknes force that causes bubbles to be attracted to or repulsed from one another, if they are sufficiently close to one another. When the microbubbles are attracted to one another due to the secondary force, stable clusters form [21, 24, 67]. While conducting the experiments in this dissertation, these microbubble clusters were not observed in any of the experiments, except in between experiments at very low flow rates (when the flow was almost stationary). Typically, the magnitude of the secondary Bjerknes force is much smaller than the primary Bjerknes force, so it will not be discussed in this dissertation. However, it should be mentioned that the magnitude of the secondary force can become significant in smaller vessels where the spacing between microbubbles is significantly reduced compared to the experiments in this thesis that mimic large arterial flows [24].

Chapter 3

METHODS

The following chapter presents details of the experimental developments carried out in this thesis. The first part of this chapter covers information regarding the two different types of microbubbles used in the experiments. The second part of the chapter describes the two experimental setups that have been developed to image the microbubbles: an acoustic setup that uses a clinical ultrasound scanner to image the microbubbles and an optical setup that uses a high-speed camera to image the microbubbles. The final two sections of this chapter discuss the importance of material selection for the flow phantom and the working fluid in order to minimize index of refraction effects (in the optical imaging) and to minimize ultrasound attenuation and scattering (in both imaging modalities).

3.1 Microbubble Information

Two different types of microbubbles were used in the experiments conducted to examine the Bjerknes force acting on the microbubbles: an in-house recipe used in the Averkiou lab and commercially available Sonazoid microbubbles (GE Healthcare, Amersham, UK).

The in-house microbubbles, composed of DPPC (1,2-dipalmitoyl-sn-glycero-3-phosphocholine) and DSPE-PEG (1,2-distearoyl-sn-glycero-3-phosphoethanolamine-N-[methoxy(polyethylene glycol)-2000]) (Avanti Polar Lipids Inc, Alabaster, AL) in a 95:5 molar ratio, were prepared as previously described in [17, 84]. The microbubbles were activated in a two-step process. First, two needles were inserted into the headspace in the microbubble vial, shown in Fig. 3.1 (a). One of the needles was used to inject perfluorobutane gas into the vial; the other needle allowed any air inside the vial to be expelled. The microbubbles were then activated via high frequency shaking in a VIALMIX medical shaker (Lantheus Medical Imaging, Inc., Billerica, MA) for 15 seconds. After agitation, the microbubbles were then drawn out of the vial using the same two needle system, shown in Fig. 3.1 (b). Now, one needle was attached to a syringe to withdraw microbubbles instead of the gas. The other needle was used to vent the vial to maintain a constant pressure during the microbubble withdrawal. Typically, 2 mL of the concentrated microbubble solution were withdrawn from the vial and then diluted further depending on the desired concentration of microbubbles in the experiments.

(a)

(b)

Figure 3.1: Example of experimental procedure to activate in-house microbubbles. (a) Air inside the vial is expelled using perfluorobutane gas. Note: gas canister is not to scale. (b) The microbubbles are withdrawn using a syringe.

The Sonazoid microbubbles were activated according to the manufacturer's instructions. The microbubbles were withdrawn from the vial using the same method as the in-house microbubbles. As before, 2 mL of the concentrated microbubble solution was withdrawn from the vial and then diluted further depending on the desired concentration of microbubbles in the experiments.

The size and the concentration of the in-house microbubbles in the dispersion were determined with a Multisizer 3 (Beckman Coulter, Brea, CA). The microbubbles have a mean diameter of 4.868 μm and a concentration of 1.735×10^9 bubbles/mL. The Sonazoid microbubbles had a mean diameter of 2.6 μm and a concentration of 1.2×10^9 bubbles/mL [81].

3.2 Transducer Characterization

A Panametrics-NDT V303 single element circular transducer (Olympus NDT, Waltham, MA) was placed in a rectangular water tank to characterize its pressure output at a range of input voltages. Figure 3.2 shows the experimental setup used to characterize the pressure output. The V303 transducer was submerged and its acoustic output was recorded using a needle hydrophone. Data was collected using LabVIEW VIs (National Instruments, Austin, TX) that controlled both the positioning of the hydrophone (x, y, and z directions) and the recording of the voltage measured by the hydrophone, which was directly correlated to pressure using a calibration curve.

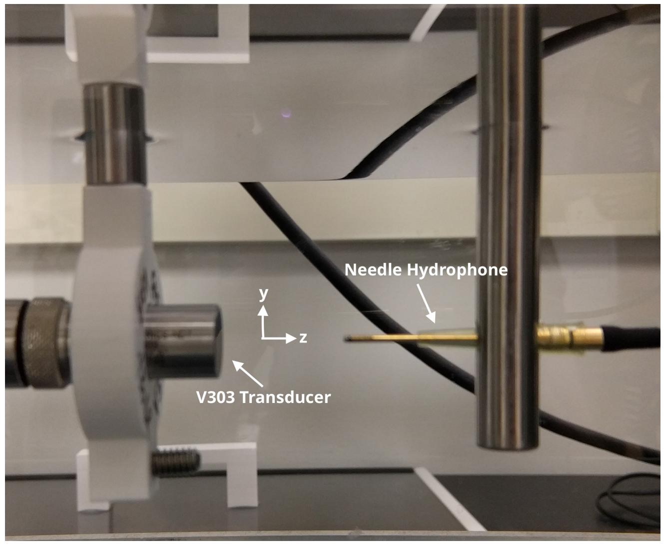

Figure 3.2: Image showing the positioning of the pushing transducer and needle hydrophone in the water tank used for acoustic measurements.

Hydrophone measurements were taken at both the Rayleigh distance and the Rayleigh distance divided by π. The Rayleigh distance is the point where the ultrasound beam transitions from the nearfield to the farfield, and the Rayleigh distance divided by π is the distance where the pressure amplitude is maximum. Equation 3.1 shows the Rayleigh distance, R_0.

$$R_0 = \frac{ka^2}{2} \tag{3.1}$$

where k is the wavenumber and a is the radius of the transducer.

The following curves were produced with the settings shown in Table 3.1.

Frequency	1 MHz
Amplitude (pulse generator)	100 mV
Number of Cycles	20
Trigger Interval	5 ms
Duty Cycle	0.4 %
R_0	84.5 mm
R_0/π	26.9 mm

Table 3.1: Ultrasound parameters for propagation curve and beam patterns

3.2.1 Propagation Curve

Figure 3.3 characterizes how the pressure amplitude changes axially away from the transducer, with zero on the figure's x axis corresponding to the surface of the transducer. The maximum pressure occurs at approximately 26.8 mm, which corresponds to the R_0/π.

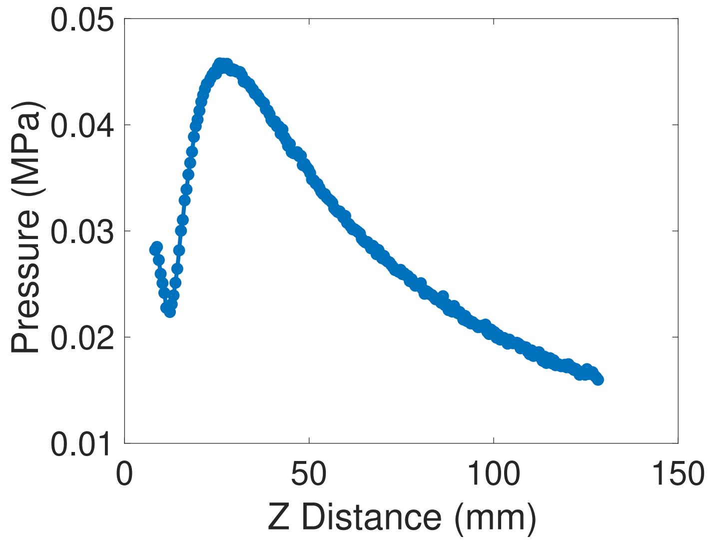

Figure 3.3: Propagation curve showing the pressure amplitude as a function of distance away from the transducer. The peak occurs at 26.8 mm, approximately the Rayleigh distance divided by π (R_0/π).

3.2.2 2D Beam Patterns

Figure 3.4 shows both the 2D beam pattern and the 1D beam pattern (along the x axis of the water tank) at two different locations along the z axis: R_0/π and R_0. At R_0/π, the maximum pressure amplitude is about 0.046 MPa and the beam width (at the -6 dB down points) is approximately 6.5 mm (or about 0.25 inches). At R_0, the maximum pressure amplitude is 0.024 MPa and the beam width is approximately 15 mm (or about 0.59 inches). Therefore, at R_0, the maximum pressure amplitude is about half of the maximum amplitude at R_0/π. Conversely, the beam width is about 2.3x as large as the beam width at R_0/π. This trade-off between pressure amplitude and beam width needs to be carefully considered in the experiments. Since the transducer is unfocused, it is important to be acting near its maximum pressure output along its axis. However, to see a pushing affect over a wider area, giving the microbubbles more time to interact with the ultrasound beam, it is worth considering taking a small loss in pressure amplitude to have a larger beam width.

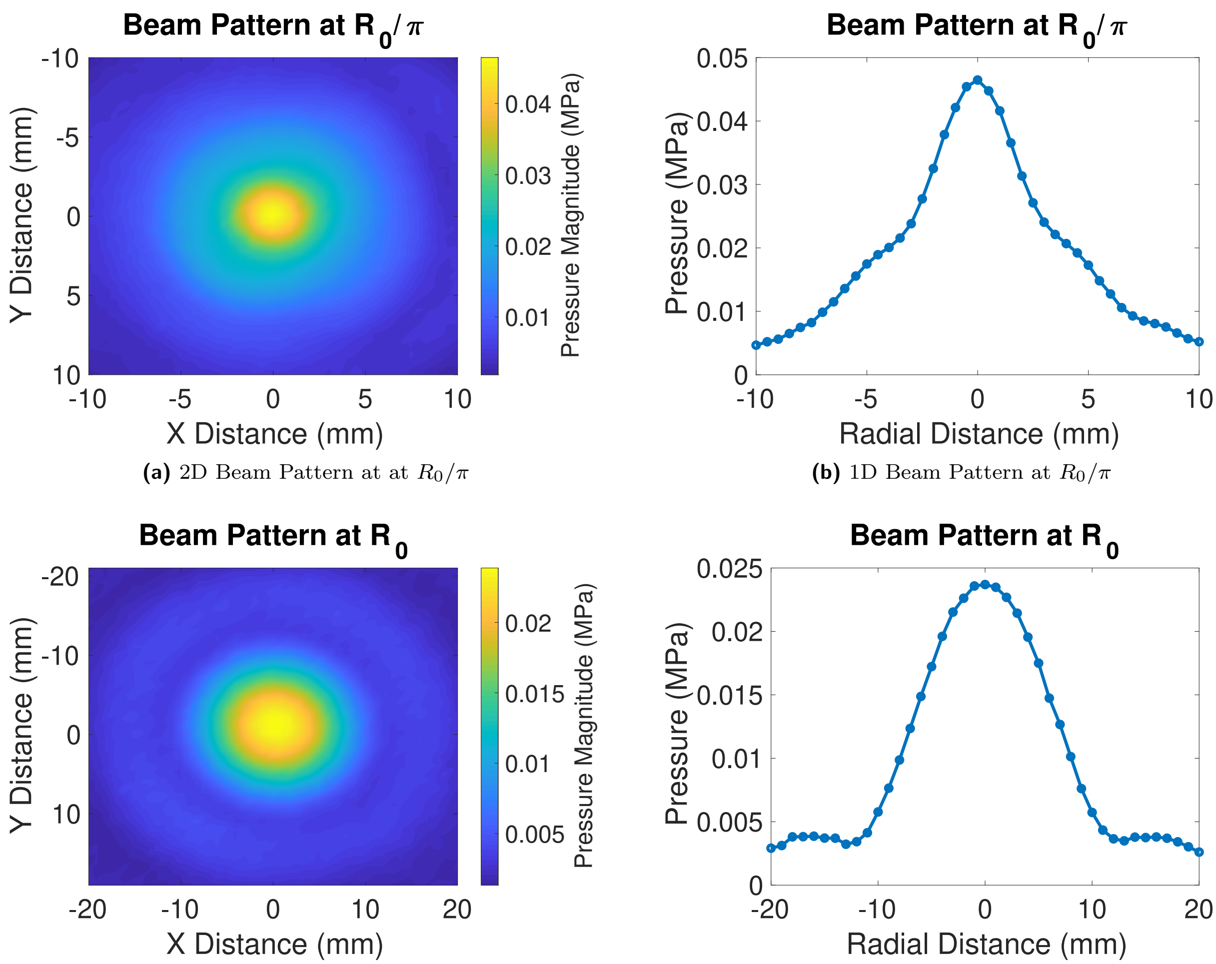

(a) 2D Beam Pattern at at R_0/π **(b)** 1D Beam Pattern at R_0/π

(c) 2D Beam Pattern at R_0 **(d)** 1D Beam Pattern at R_0

Figure 3.4: Beam patterns: (a) 2D beam pattern in the xy-direction in the water tank at R_0/π. (b) 1D beam pattern along the x-direction in the water tank at R_0/π. The pressure amplitude is greater and the beam is narrower at this location. (c) 2D beam pattern in the xy-direction in the water tank at R_0. (d) 1D beam pattern along the x-direction in the water tank at R_0. The pressure amplitude is smaller but the beam is wider at this location. Note: Axis dimensions are different since data was only taken between -10 and 10 mm in (a) and (b), where it was taken between -20 and 20 mm in (c) and (d).

3.3 Experimental Setups

Two experimental setups were developed to examine the response of microbubbles to ultrasound excitation at a range of flow rates (Reynolds numbers), pressure amplitudes, and ultrasound pulse-repetition frequencies (PRFs). The initial experimental setup used ultrasound as the imaging modality since commonly available tubing materials that are transparent to ultrasound are not optically transparent. The flow rates that could be explored in this experimental setup were limited due to the acquisition rates available in clinical ultrasound systems. Due to this limitation, another experimental setup was developed using optical imaging as the imaging modality. This allowed faster acquisition rates (on the order of kHz in the optical imaging versus Hz in clinical ultrasound scanners). Additionally, the resolution of the optical imaging was better (of the order of μm in optical imaging at high magnification versus $O(mm)$ in the ultrasound system), which allowed for closer examination of bubble behavior based on microbubble size.

3.3.1 Ultrasound Imaging

An experimental setup using an ultrasound imaging probe was developed to examine the forces acting on ultrasound contrast agents in a variety of flow conditions: a quiescent fluid environment, uniform flow, and pulsatile flow. Using ultrasound as an imaging modality increases the translatability of this research to future animal and human models, both in vivo and ex vivo.

The ultrasound experimental setup was created inside a rectangular acrylic tank (50.8 cm $\times$ 25.4 cm in cross-sectional area) equipped with two three-axis positioning systems: one to translate the pushing transducer and the other to translate the imaging probe. Fig 3.5 shows a schematic of the experimental setup. The sides of the tank were covered with acoustic attenuators to minimize reflections from the tank walls. Silicone tubing, chosen for the part of the phantom to be imaged due to its favorable acoustical properties, was held between two 3D-printed holders attached to adjustable optical posts.

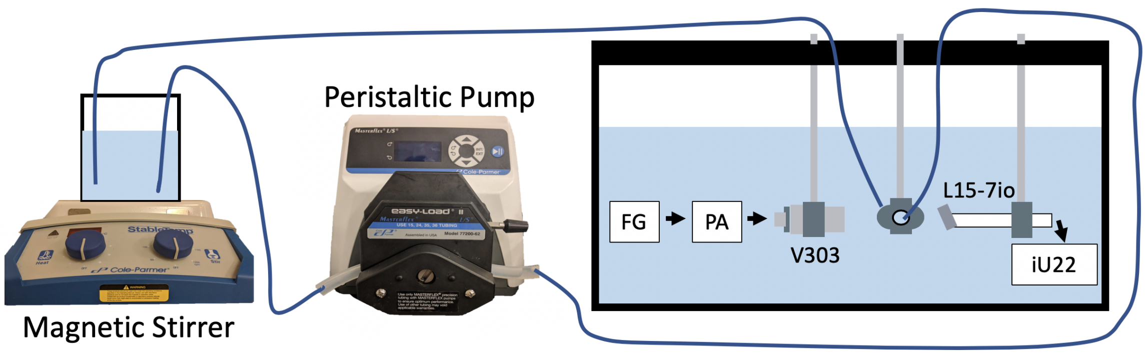

(a)

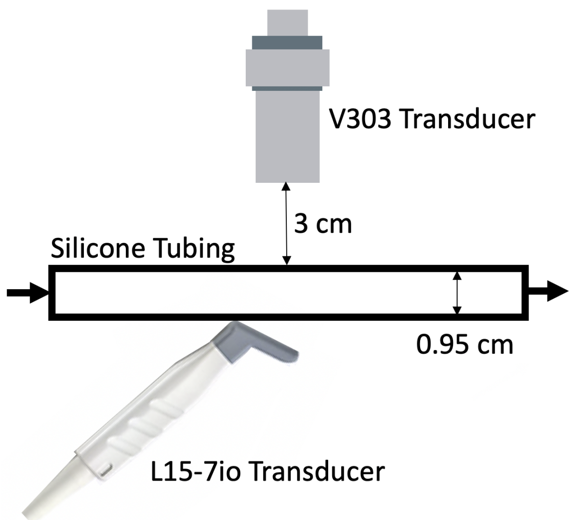

(b)

Figure 3.5: Ultrasound experimental setup. (a) Entire water tank setup including the magnetic stirrer and peristaltic pump. The V303 pushing transducer is controlled using a function generator (FG) and power amplifier (PA) to run experiments at a variety of cycle lengths and pressure amplitudes. Not shown: optional pulse dampener used for uniform flow experiments. (b) Close up view of the experimental setup showing the alignment of the pushing transducer and imaging transducer with respect to the silicone tubing.

A V303 pushing transducer was held with the same holder and optical post setup to facilitate aligning the pushing transducer with the silicone tubing. However, unlike the tubing, the pushing transducer could be finely adjusted using a three axis positioning system. A pulse-echo method was used to align the V303 transducer with the silicone tubing. The height of the transducer was adjusted until the amplitude of the reflection was maximized; this corresponded to the center of the tubing. Additionally, the transducer was rotated along its axis to make sure the transducer was perpendicular to the tubing, marked by an increase in amplitude of the reflected signal. Figure 3.6 (a) shows an example of the signal found using the pulse-echo method. In this case, one can see that the reflection of the tubing occurs at 40.3 microseconds, which corresponds to a distance of approximately 3 cm. This signal was maximized during alignment to make sure the imaging transducer was exactly perpendicular to the silicone tubing. Using this information and the known transducer pressure field, we can estimate pressure amplitudes at the tubing wall and inside the tubing.

Image sequences were taken using an iU22 ultrasound scanner and an L15-7io broadband linear array transducer (Philips Healthcare, Bothell, WA). The imaging transducer was held using a custom 3D-printed holder attached to an optical post. This transducer could also be adjusted in three dimensions using a motorized three axis positioning system, which could be controlled via a LabVIEW VI on a desktop computer. A region of interest (ROI) analysis was performed to align the imaging transducer with the silicone tubing. Figure 3.6 (b) shows the ROI that was selected in the ultrasound loop. The ROI was chosen to encompass the entire top wall of the tubing (both the outside and inside position of the top tube wall). The intensity in this ROI region was then analyzed over the entire ultrasound loop, as shown in Figure 3.6 (c). The maximum intensity found in the ROI corresponds to the vertical center of the tubing wall. The vertical position of the imaging probe was then adjusted so that it was located at the intensity peak (tube center).

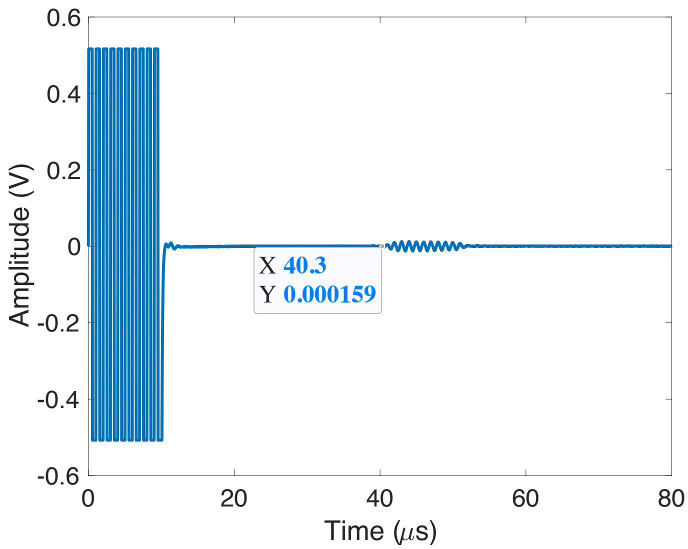

(a)

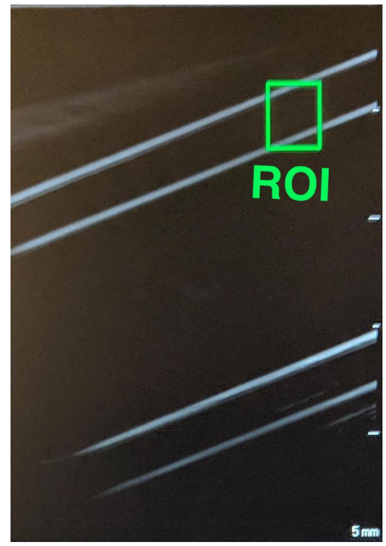

(b)

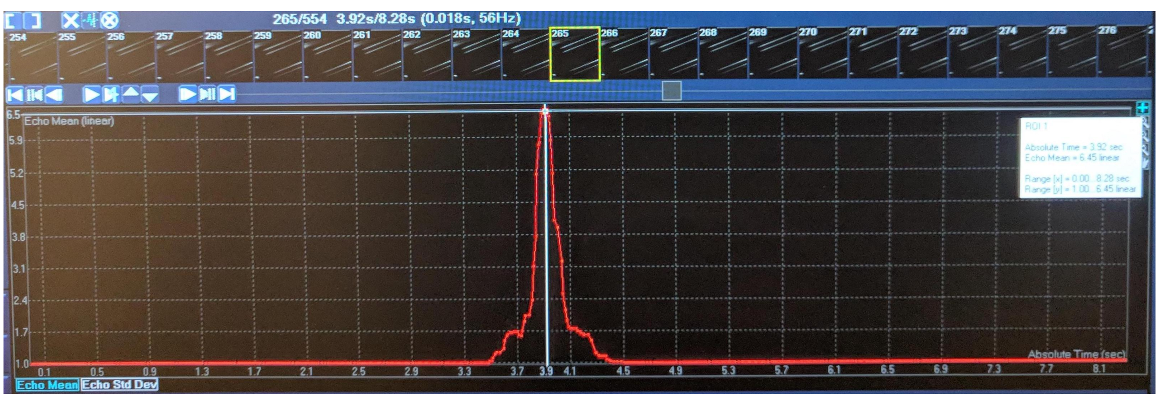

(c)

Figure 3.6: Techniques used to align the V303 pushing transducer and the L15-7io imaging transducer to the center of the silicone tubing. (a) An example waveform obtained using the pulse echo method to align the pushing transducer to the silicone tubing. This method also gives the distance between the front of the pushing transducer and the wall of the silicone tubing. (b) An example ROI used for alignment of the imaging transducer to the silicone tubing. (c) A plot of image intensity over time, where the peak intensity corresponds to the center of the silicone tubing.

A selected concentration of microbubbles could be introduced to the flow loop by injecting them into a beaker on a magnetic stirrer. The microbubbles were stirred for approximately 30 seconds and then the flow was started to pump the microbubbles through the flow loop and into the imaging section of the flow loop. The flow was driven by a MasterFlex L/S peristaltic pump (Cole-Parmer, Vernon Hills, Il) that was able to produce flow rates between 0.034 and 100 mL/min, corresponding to Reynolds numbers between 1 and 2500 in the 9.5 mm ID silicone tubing. To create uniform (non-pulsatile) flow in the experiments, a pulse dampener was added to the experimental setup.

This experimental setup allowed for exploration of the response of microbubbles to ultrasound at a variety of flow conditions and ultrasound settings. However, the range of flow parameters that could be explored was limited due to the acquisition rate in clinical ultrasound systems. In the experiments reported in this thesis, they typically ranged between 30 and 110 fps. Additionally, the concentration of microbubbles per fluid volume had to be extremely low so that individual microbubbles could be tracked. Despite these limitations, these experiments provided great insight into the behavior of microbubbles under ultrasound excitation at a small range of physiologically relevant Reynolds numbers, extending previous experimental studies, and a variety of ultrasound parameters, which provided guidance for the optical experiments.

3.3.2 Optical Imaging

An experimental setup using a high-speed camera was developed to examine the forces acting on ultrasound contrast agents in uniform flow at higher Reynolds numbers than the ultrasound experimental setup. Using optical imaging as the imaging modality increases the acquisition rate and resolution of the images enabling individual microbubbles to be easily tracked and their sizes measured with greater accuracy, even at higher Reynolds numbers. A Phantom V12 high-speed camera (Vision Research, Wayne, NJ) and a K2/SC long-distance lens (Infinity, Boulder, CO) were used to image microbubbles in a uniform flow created by a hydrostatic pressure difference between two reservoirs, at magnification levels similar to those available in a typical upright microscope system (2 to 20X). Table 3.2 shows the different lens setup options.

	STD	CF-2	CF-4
Primary Magnification	0.95X-0.31X	2.29X-0.71X	5.33X-4.27X
Field of View (1/2" sensor) (mm)	6.74-20.5	2.8-4.7	1.20-1.50
Numerical Aperature	0.051-0.02	0.136-0.099	0.204-0.172
Working Distance (mm)	360-980	138-205	55-63

Table 3.2: K2/SC objective options (adapted from [37]).

In this experimental setup, microbubbles were injected upstream of the tube or vessel phantom via a syringe. Next, microbubble images of the flow inside tubing that mimics a small artery (2-8 mm in diameter) were collected using the CF-2 objective. However, due to the magnification, it was difficult to track individual microbubbles using the CF-2 objective. Therefore, the CF-4 objective was used for greater magnification of the microbubble flow, which was essential for tracking individual microbubble paths. These images were backlit using a fiber optic illuminator (Model MI-150, Edmund Optics, Barrington, NJ). Figure 3.7 shows an example of the long distance lens setup with fiber optic illumination and Polytetrafluoroethylene (PTFE) tubing. Both PTFE tubing and silicone phantoms were used in the optical experimental setup. The PTFE was chosen because its index of refraction was very similar to the index of refraction of water, so we could use water as the working fluid as done in the ultrasound experiments. The silicone phantoms were developed to look at microbubble behavior in patient specific geometries and explore the possibility of steering bubbles towards a selected downstream branch of a carotid bifurcation. However, a much more viscous glycerine/water solution needed to be used to match the index of refraction of the silicone.

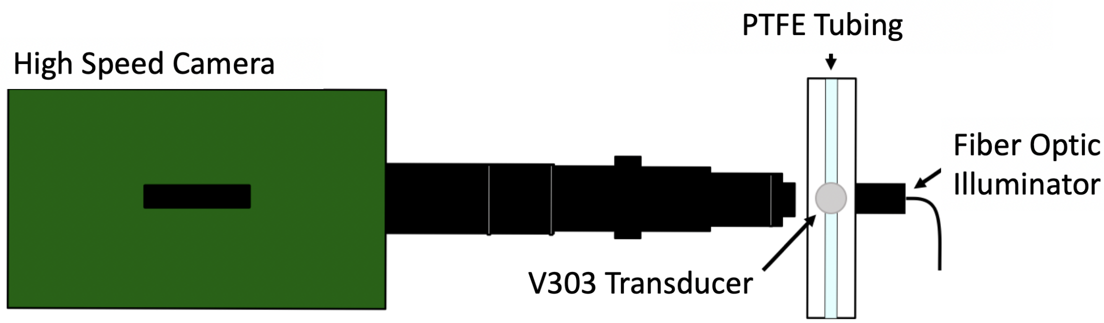

(a)

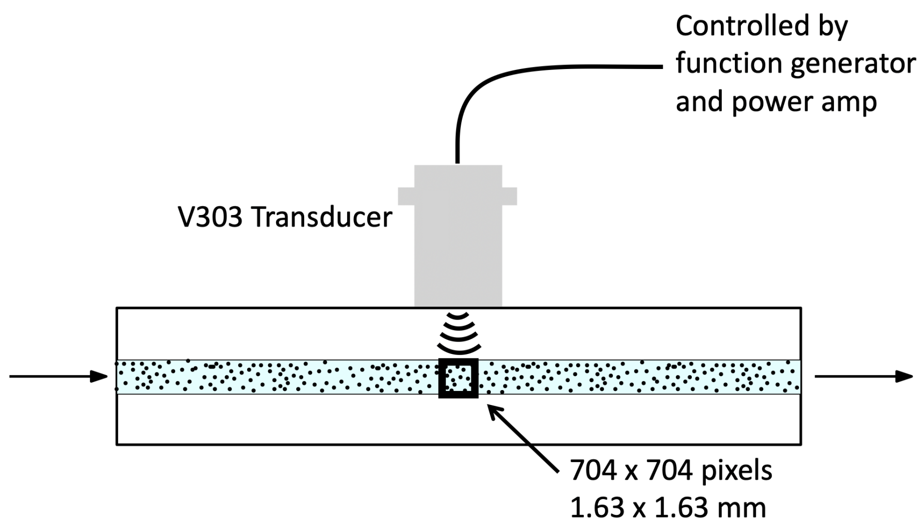

(b)

Figure 3.7: Optical experimental setup. (a) Top view of the experimental setup showing the alignment of the high-speed camera, fiber optical illuminator, and pushing transducer. The V303 pushing transducer is controlled using a function generator and power amplifier to run experiments at a variety of pulse repetition frequencies (PRFs) and pressure amplitudes. Not shown: the reservoir system used to drive the flow. (b) Close up side view of the experimental setup showing the alignment of the pushing transducer with the PTFE tubing. The imaging field of view (1.63×1.63 mm) is also shown.

Polytetrafluoroethylene (PTFE) Tubing

PTFE tubing (1.65 mm ID, 0.048 mm wall thickness, Zeus Industrial Products, Inc., Orangeburg, SC) was used for the first set of optical experiments because of its favorable optical properties. It should be noted that while it worked well optically, it was not a good match acoustically: there was approximately a 10% loss of the ultrasound signal through the tube. Despite this limitation, it was still used for the optical experiments since it was a readily available tubing material and the effect of the ultrasound could still be seen in the tube (without any noticeable detection of standing waves). The PTFE tubing was held inside a rectangular acrylic box (14 cm L $\times$ 4 cm W $\times$ 4 cm H). The box was designed to be very narrow since the working distance of the long distance lens with the 4X objective was between 55 and 63 mm. Additionally, the tubing was positioned such that the ultrasound transducer could be placed approximately 2.7 cm from the top of the tube wall (see Fig. 3.7), corresponding to the location of the maximum pressure amplitude of the transducer (Rayleigh distance divided by π, R_0/π, for the V303 pushing transducer).

Silicone Phantom

The PTFE tubing was used in the first set of optical experiments. However, this research also considered patient specific geometries for future translational applications ex-vivo or in-vivo. Therefore, Sylgard 184 was used to create flow phantoms for use with the optical experimental setup. This material was chosen because it has a proven track record for model casting in the literature [9, 31, 35, 71]. In addition to a straight tube silicone phantom, a silicone phantom of a carotid artery was created, since this aligned well with future experimental plans of steering the microbubbles in an anatomically relevant bifurcation (the carotid bifurcation) to induce a strong bias where the bubbles would preferentially pass through one of the branches (the internal carotid) over to the other one (external carotid) in a proportion much higher than the flow rate split ($\approx 60/40$).

A model of the carotid artery was developed using patient-specific 3D Ultrasound (B-mode) measurements obtained from our clinical collaborators. The 3D US data was segmented and a 3D surface reconstruction of the lumen (in .STL format) was created using MeshMixer, a 3D modeling program. The model of the carotid artery was printed with polylactic acid (PLA) filament. An image of a 3D-printed carotid artery is shown in Figure 3.8. The test parts were printed at normal resolution since this provided a nice compromise between print quality and print duration.

Figure 3.8: Image of a 3D printed carotid artery.

Two methods were used to smooth the ridges on the printed parts. The parts were first sanded down until the ridges were removed. However, this method was very time consuming and did not lead to a perfectly smooth surface. XTC-3d (Smooth-On, East Texas, PA), an epoxy-coating, was next used to coat the printed part. It cured to a hard coating that could then be sanded if necessary to bring the surface of the part back to its initial size, augmented slightly by the addition of the epoxy layer. Figure 3.9 shows the results of each method.

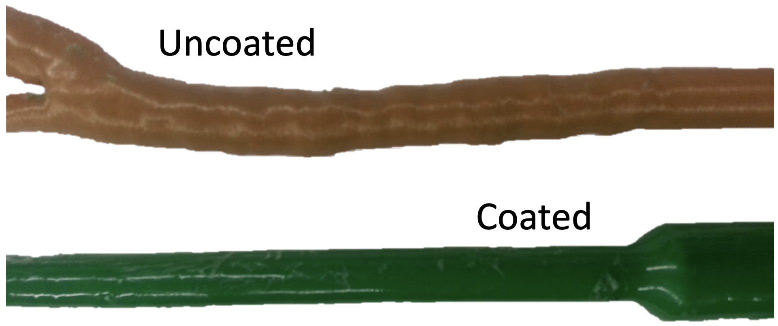

Figure 3.9: Image showing two 3D printed parts: one with a sanded surface and a another coated with XTC-3. The surface of the uncoated part still has small ridges from the 3D printing even though it was sanded. The surface of the coated part is much smoother because the epoxy-coating fills in the ridges.

Once sufficiently smoothed and with the right dimensions, the part was then cast into silicone. Traditional casting methods, such as lost wax casting, use a four step process to create a silicone flow phantom. Figure 3.10 visually shows the steps in this process. The first step of this process involved creating a 3D model of the artery (green 3D printed part). This model was then cast in a molding polymeric material (Oomoo 25, Smooth-On). Once the material cured, the model was gently removed from the molding material by cutting the mold into two pieces. The mold was then resealed and wax was poured into it. This creates another copy of the original model (pale yellow carotid) that could be casted in PDMS (Sylgard 184, Dow-Corning, Auburn, MI) and melted out of the final transparent phantom, leaving an open volume equal to the lumen of the original artery in the medical images. This method can be shortened to a two step process if the geometry of the artery is fairly simple. For the straight tube, the 3D-printed part was cast directly into the clear silicone. The silicone was then placed in the oven at 100 °C for 35 minutes to cure. Once cured, the printed part could be removed from the phantom. This is done by breaking the printed part towards its center, so it can easily be pulled out from both sides of the artery.

Figure 3.10: Steps in lost wax casting.

3.3.3 Index of Refraction Experiments

Once the experimental setup was developed, the next step was to determine the working fluid to be used in the experiments. The proper choice of fluid was important to minimize refraction effects caused by the index of refraction mismatch between the tubing and the working fluid. Budwig [10] provides a nice review of optical properties of glass, plastics, and aqueous solutions. Nguyen et al. [58] reviewed previous fluids that had been used as blood analogs in cardiovascular models. They found that most of these fluids were dangerous and/or expensive, and did not match the kinematic viscosity of blood well. They, therefore, developed empirical relationships to determine the index of refraction and kinematic viscosity of non-toxic fluids that could potentially be used as blood analogs. The fluids that they explored were: D-limonene, diethyl phthalate, methyl salicylate, mineral oil, ethanol, glycerine, and water. Buchmann et al. [8], Geoghegan et al. [31], Hopkins et al. [35] used a mixture of water and glycerine as a blood-analog fluid . We chose to further explore mixtures of glycerine and water for use in our experiments because glycerine was easy to obtain, safe, and relatively inexpensive.

Hopkins et al. [35] used a grid method to determine the correct fluid ratios needed to match the index of refraction of the working fluid and the test section. We used a similar method to determine the correct fluid to use with the Sylgard 184 phantom used in the optical setup experiments. Figure 3.11 shows different ratios of distilled water and glycerine inside of the tube and also air (0% glycerin-0% water). It was shown that a ratio of 60% water to 40% glycerine gave the best results for our phantom, which closely agrees with the 61% water to 39% glycerine ratio used by Geoghegan et al. [31].

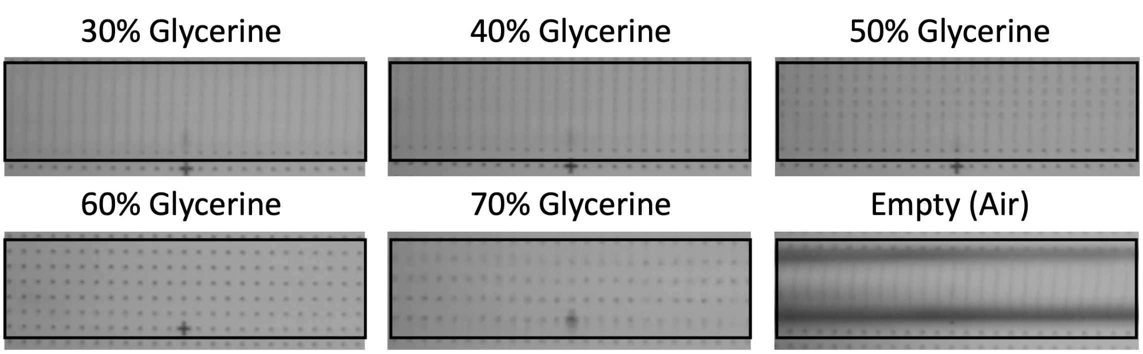

Figure 3.11: Montage of index of refraction test images for different glycerine/water ratios in Sylgard 184. From the images, it is apparent that a 60% glycerine-40% water (wg.) ratio is index matched to the Sylgard 184 material.

Table 3.3 shows the materials used in the optical imaging experiments and their ultrasound properties: c is the speed of sound in the material, SG is the specific gravity of the materials, Z is the acoustic impedance of the material, and n is the index of refraction of the material. Sylgard 184 (a similar material to the silicone tubing used in the ultrasound experiments) has favorable acoustic properties since its acoustic impedance is similar to water. Previous research has shown that there are other materials that also work well for ultrasound imaging, such as hydrogels, but these materials have much shorter shelf lives and are not as durable [11, 40, 53, 60, 71, 92]. Additionally, ultrasound phantom development is still an area of active research, so there may be other promising material options available in the future.

Material	c (m/s)	SG	Z (MRayl)	n
Water at 25°C	1497	0.998	1.49	1.33
Glycerine at 25°C	1904	1.26	2.34	1.47
Acrylic	2750	1.19	3.26	1.49
Sylgard 184	1027	1.05	1.04	1.41
PTFE	1400	2.20	3.08	1.35

Table 3.3: Properties of selected materials taken from [64].

3.4 Important Nondimensional Parameters Considered for Experimental Development

There are two main nondimensional parameters that will be considered throughout this dissertation: the Reynolds number and the Womersley number. These two nondimensional numbers can be used to inform our experimental parameters so that our flow conditions are matched to relevant cardiovascular conditions. For example, we can match the Reynolds and Womersley numbers in our experimental setup to the Reynolds and Womersley numbers found in actual arteries (similitude).

The Reynolds number, relating the inertial to the viscous forces, is defined as:

$$Re = \frac{\rho v L_c}{\mu} \tag{3.2}$$

where ρ is the density of the working fluid, v is the average velocity, L_c is the characteristic length ($L_c = D$ in a tube), and μ is the dynamic viscosity of the working fluid. In typical cardiovascular applications, the Reynolds number is approximately 1 in small arterioles to approximately 4000 in the largest artery, the aorta [42]. When the Reynolds number is small ($Re_D < 2300$), the flow is laminar. Above this value, the flow starts to transition to turbulence. In our experiments, we will explore Reynolds numbers between approximately 75 and 700.

The Womersley number, relating the unsteady and viscous forces, is defined as:

$$Wo = \alpha = \frac{D}{2}\sqrt{\frac{\omega}{\nu}} \tag{3.3}$$

where D is the diameter of the tube, $\omega = 2\pi f$ is the angular frequency of the flow pulsations, and ν is the kinematic viscosity of the working fluid. The Womersley number is another nondimensional number commonly used in biological systems such as blood flow in arteries. When α is small (O(1) or smaller), the flow pulsations are very small and the flow will have sufficient time to develop in the tube, giving rise to a canonical Poiseuille profile. When α is larger, the flow does not have as much time to develop in the tube and the velocity profile will be flatter.

Finally, another nondimensional parameter to consider in our ultrasound experimental setup is the Dean number, defined as:

$$De = Re\sqrt{\frac{D}{2R_c}} \tag{3.4}$$

where Re is the Reynolds number introduced above, D is the diameter of the tube, and R_c is the radius of curvature along the tube. At low Dean numbers ($De < 40 - 60$), the flow in the tube maintains a Poiseuille profile. However, at slightly higher Dean numbers

($40 - 60 < De < 64 - 75$), the flow starts to become unstable and the flow profile shifts towards the outer wall of the tube [32, 83]. This will be seen in when we characterize flow profiles using the ultrasound experimental setup in Chapter 5.

Chapter 4

PARTICLE TRACKING

Particle tracking is a method to reconstruct the trajectories of each microbubble in the flow by matching the locations of the bubble's centroid in sequential frames in the video. The bubble trajectories give us the foundational data to explore the effects of hydrodynamic and ultrasound-induced forces on microbubbles. The bubbles will rise due to buoyancy, move with the flow due to hydrodynamic drag, and be driven to the vessel's center due to hydrodynamic lift, when ultrasound is not present. When ultrasound excitation is active, however, the effects of the primary and secondary acoustic radiation forces noticeably modify the bubble trajectories. It is, therefore, important to be able to accurately capture the bubble trajectories so that we can understand how the bubbles behave with and without ultrasound, and quantitatively model the forces acting on them as a function of the flow (hydrodynamic) and ultrasound parameters.

4.1 Image Processing

The first step in the particle tracking algorithm is the post-processing of the microbubble images extracted from either the ultrasound images or the high-speed optical images acquired from the experiments. This is done via an image segmentation method known as thresholding. A basic thresholding algorithm will replace each pixel value in an image with a black or white pixel depending on how it relates to the specified threshold value. For an 8-bit, greyscale image, with a pixel range of 0 (black) to 2^8-1 or 255 (white), a pixel would be assigned a black pixel if it is below the specified threshold or a white pixel if it was above the specified threshold value. It is necessary to threshold the images to separate the foreground of the image (the microbubbles) from the background.

There are two thresholding methods available: global thresholding and local thresholding. Global thresholding is typically used when the histogram of the image intensities is approximately Gaussian or if the histogram has two distinct peaks. Whereas, local thresholding is typically used when the histogram is not clean and there are large illumination gradients across the image.

4.1.1 Processing iU22 Images

A global thresholding algorithm was used to post-process the microbubble images (each slice from a DICOM loop) from the iU22 ultrasound system. A four step process was used to segment the microbubbles and obtain their centroid locations (as well as area, eccentricity, etc.). First, individual DICOM loops were read into MATLAB and were converted into a greyscale image stack. A temporal average was then performed on the image stack to get a background image. This background image was then subtracted from each of the images in the greyscale image stack. The resulting images could then be thresholded using a value selected to separate the foreground from the background in the images. Finally, microbubble locations could be determined using MATLAB's regionprops algorithm. This process is shown in Fig. 4.1.

As can be seen in Fig.4.1 (d), this process works very well for finding the locations of microbubbles in the ultrasound images. It should be noted, however, that the performance of the algorithm is largely dependent on the concentration of microbubbles in the images. If the microbubble concentration is too large, it is nearly impossible to discern individual microbubbles since there is large overlap between the microbubbles in the images. Consequently, the concentration of microbubbles in the experiments were carefully controlled to make sure there were no more than approximately 100 microbubbles per image. This allowed the centroids of each individual microbubble to easily be found, which could then be used in the tracking algorithm.

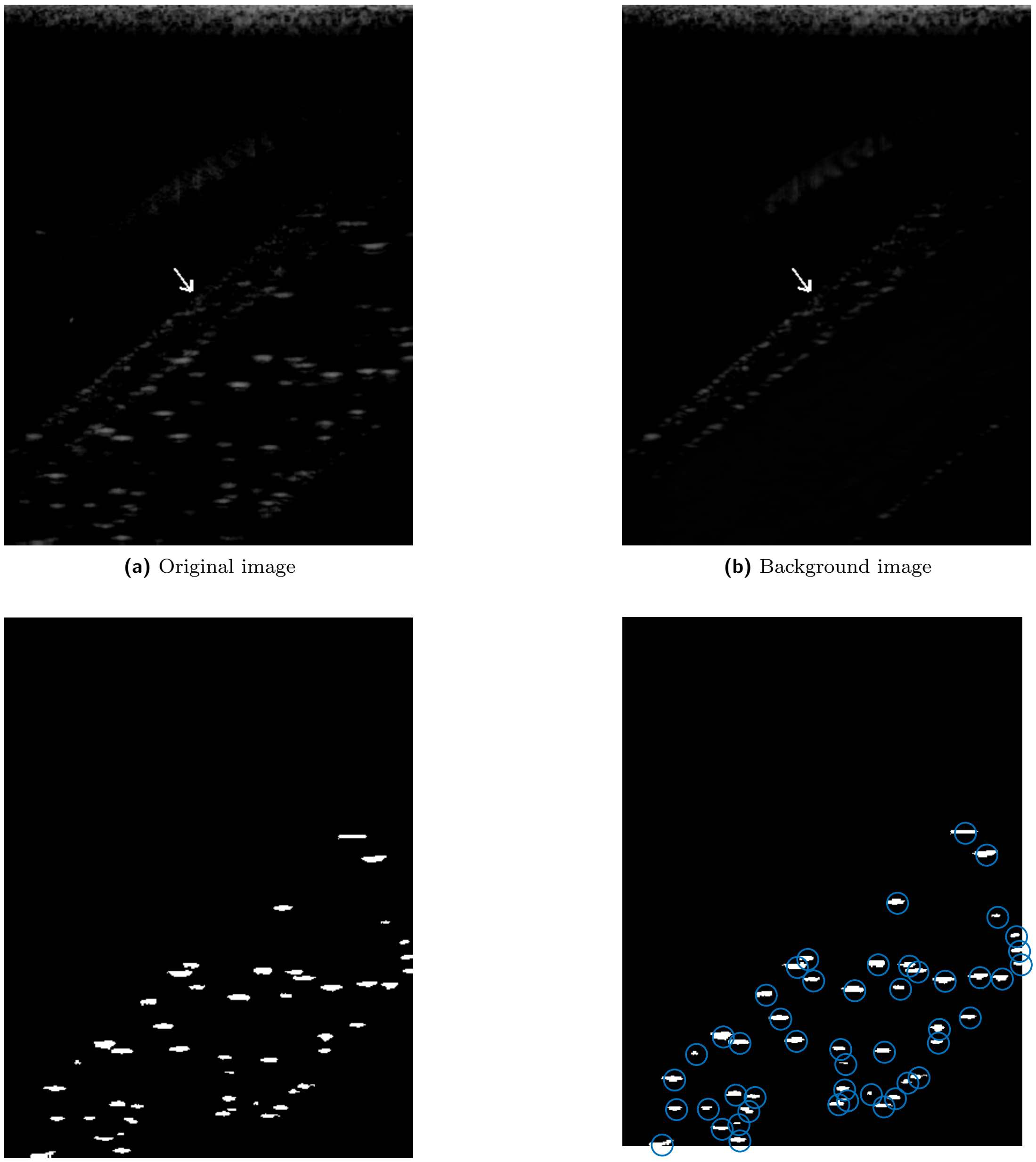

(a) Original image

(b) Background image

(c) Binarized image

(d) Detected bubble centroids

Figure 4.1: Ultrasound image analysis: (a) Original greyscale image taken from a DICOM loop from the iU22 imaging system. (b) The background image obtained when the DICOM stack is averaged over time. (c) The background subtracted and binarized image. A global threshold is used in MATLAB. (d) The resultant bubble centroids obtained using regionprops in MATLAB.

4.1.2 Processing Phantom Camera Images

A local thresholding algorithm was used to post-process the optical microbubble images due to the low contrast in the images and spatial and temporal variations in illumination.

Sauvola and Pietikäinen [77] proposed that the local threshold value T(x,y) be calculated as:

$$T(x,y) = m(x,y)\left[1 + k\left(\frac{s(x,y)}{R} - 1\right)\right] \tag{4.1}$$

where $m(x,y)$ is the mean and $s(x,y)$ is the standard deviation of the pixel intensities in a window centered around (x,y), R is the dynamic range (the ratio between the maximum and minimum pixel intensities) and is equal to 0.5 for a normalized image, and k is a constant between 0.2 and 0.5. The local values (mean and standard deviation) alter the local threshold depending on the level of contrast in the local region. At high levels of contrast, the standard deviation approaches R, and the local threshold $T(x,y)$ is approximately equal to the local mean intensity $m(x,y)$. If the contrast is low, the standard deviation is less than R, and the local threshold is lower than the local mean intensity. This removes the dark regions in the image.

Phansalkar et al. [69] extended this algorithm to look at low contrast dark regions as well. They proposed the following equation:

$$T(x,y) = m(x,y)\left[1 + pe^{-q\cdot m(x,y)} + k\left(\frac{s(x,y)}{R} - 1\right)\right] \tag{4.2}$$

where p and q are constants. These constants are selected based on information from the images. The value of q is chosen so that an intensity value above the maximum intensity of the objects of interest (in our case, the microbubbles) will cause the exponential term to go to zero and the equation to reduce to Equation 4.1. The value of p is chosen to tune the magnitude of the exponential term. If the value of p is low, the equation behaves similar to Equation 4.1. If the value of p is too high, the algorithm does not work correctly because too many background pixels are treated as objects of interest.

Equation 4.2 was implemented in Fiji (the most current implementation of NIH ImageJ) and was used to process the microbubble images acquired in the experiments. The default parameter values selected by Phansalkar et al. were used for the microbubble images because they provided accurate results validated by manually selecting microbubbles from a few selected images. In the future, it might be useful to further tune the constants in this model to extract more information from the microbubble images and not lose very small microbubbles or small clusters that do not have a circular aspect ratio. Figure 4.2 shows an example of processing a representative microbubble image using this algorithm.

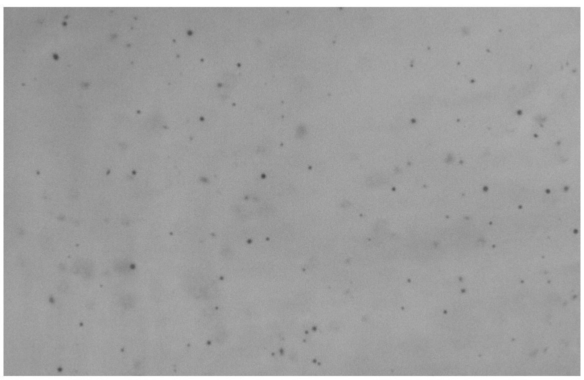

(a) Original image

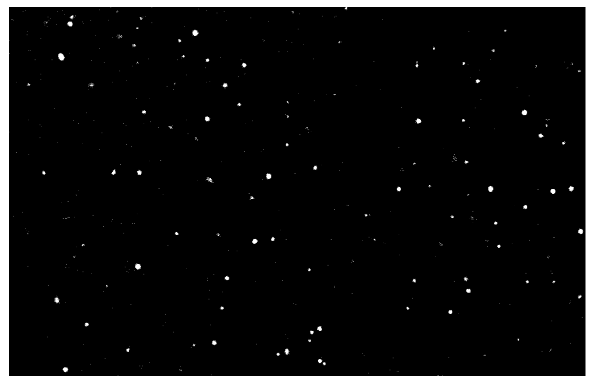

(b) Binarized image

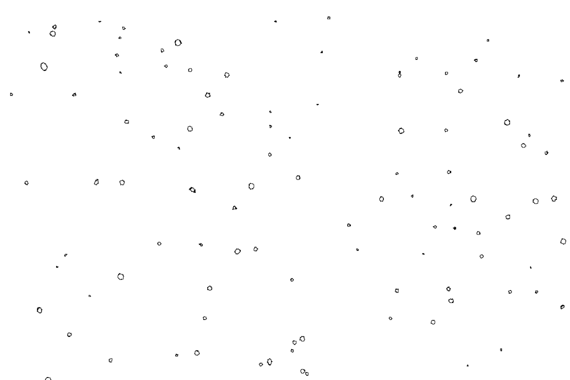

(c) Detected bubble centroids

Figure 4.2: Optical image analysis: (a) Original greyscale image taken using a high-speed camera. (b) The binarized image obtained using the Phansalkar local thresholding algorithm. (c) The resultant bubble centroids obtained using analyze particles in Fiji.

Figure 4.2 (c) shows that the algorithm in [69] accurately segments the particles from the background of the image. It should be noted that the algorithm performs best on the bubbles that are in focus; it does not capture the out of focus particles well. This is advantageous since it makes sure that we do not track out of plane particles (which may have a different velocity than in-plane microbubbles). Additionally, it was determined that the Phansalkar algorithm was less likely than other thresholding algorithms to capture noise in the image, which helps to remove some error in the tracking. This is particularly important when using the results of the image segmentation with the particle tracking code as false positives (nonexistent particles created by noise as artifacts in the images) can confuse the tracking algorithm and lead to false tracks and velocity/acceleration measurements. This is more deleterious to the measurements than missing particles because they are out of focus. Finally, once the image is segmented, Fiji is used to register the particles centroid location, its area (size), perimeter, aspect ratio (circularity), ellipticity (fitted ellipse), bounding box, etc. This microbubble information is used in the tracking algorithm, and can be used to further segment the microbubbles image signature in terms of their regularity, filtering out possible incomplete reconstructions of the microbubble tracks.

4.2 Enhancement of Particle Tracking Velocimetry Algorithms

The microbubble trajectories can be reconstructed by tracking in time their centroid locations determined by the segmentation described above in Sections 4.1.1 and 4.1.2. We introduce a method to improve Particle Tracking Velocimetry (PTV) algorithms. PTV is an experimental method used to measure the Lagrangian trajectories of individual particles over time. The trajectories are constructed by linking the particle positions from a sequence of images. Different PTV algorithms have been proposed in the literature, ranging from simply taking the nearest neighbor in the next frame to using multiframe schemes. Here we focus on the initialization of the Four-Frame Best Estimate (4BE) method introduced by Ouellette et al. that minimizes changes in acceleration to construct correct tracks. Previously, tracking algorithms have been initialized by using the particle's nearest neighbor in the next frame or by using a velocity guess to predict the particle's location in the next frame. We propose a more robust initialization, coupled with 4BE, that performs better than existing methods in the literature, in the sense of yielding a higher number of correct tracks. The performance of the proposed initialization method is compared to the 4BE method that uses nearest neighbor initialization by applying both methods on direct numerical simulation data from the Johns Hopkins Turbulence Databases (JHTDB). We show that the modified initialization greatly improves tracking in two canonical cases, homogeneous isotropic turbulence and turbulent channel flow (inhomogenous and anisotropic), greatly increasing the percentage of correct tracks found even under challenging seeding/particle displacement conditions.

4.2.1 Introduction

Particle Tracking Velocimetry (PTV) is a Lagrangian method that is commonly used in fluid dynamic experiments to capture information about individual trajectories. The particles can be flow tracers if one is interested in characterizing the flow itself (e. g. turbulence dispersion, turbulence statistics, characteristic times and lengths) or disperse-phase particles if one wants to study the behavior of a second phase in a multiphase flow (e. g. particle slip velocity or acceleration, response time, and preferential concentration) [85, 87]. The particle trajectories allow for measurements of velocity and acceleration of the disperse phase, and particles with different inertia allow for tracking of both phases to understand the underlying carrier flow dynamics. If there are enough tracks captured, average quantities can be estimated on a grid, yielding Eulerian maps (3D3C velocity field) and other common Eulerian metrics, such as second order structure functions [49]. The tracking scheme used for PTV is critical for accurate results, especially since error in the tracks between frames propagate to all other frames (unlike Particle Image Velocimetry (PIV) techniques where each velocity vector field can be computed independently of the previous time steps). For example, when an incorrect particle position is assigned to a track in one time step, not only does that track yield incorrect results but it also removes the incorrect position from its true track and leaves the rest of the positions of that particle "orphan" so they are more likely to be assigned to incorrect tracks themselves, which further propagates into future frames. Many PTV track-forming algorithms have been proposed in the literature [1, 15, 25, 46, 50, 63, 65, 89], and these methods vary based on the number of frames used to find particle trajectories (from 2 to N frames), the cost function used to assign particles to existing tracks, and also the initialization methods used to create new tracks.

Advanced PTV approaches, such as Shake-The-Box, have recently been developed and have shown great success at very high particle seeding densities [78], allowing Eulerian interpolation to produce instantaneous 3D3C velocity fields. Such methods, however, require advanced equipment (high power lasers with repetition frequencies in the kilohertz, multiple cameras, and specialized software) and their use is non-trivial. Shake-The-Box methods have very significant computational costs and have complex set-up configurations. Thus, there is a need for accurate multiframe PTV algorithms to resolve turbulent flows in which seeding density and time-resolution do not require the added complexity of Shake-The-Box, but where current methods have either low accuracy or low yield of correct trajectories. The method proposed can be used with only one camera (capturing particles in a thick plane or using shadowgraphy), multiple cameras (illuminating a volume and resolving 3D flow or particle statistics), and is open-source. Additionally, the inputs to the proposed tracking algorithm depend solely on known flow characteristics (e.g. the expected average displacement of particles between frames). Consequently, the proposed tracking method performs extremely well in multiple simple applications such as dispersion in a turbulent channel flow. An example application is 2D tracking with one camera and backlighting, where the 3D physical space is projected onto the 2D sensor of the camera. The method performs extremely well in this application, even at higher particle seeding densities or in flows where there are large particle displacements between frames.

Ouellette et al. [65] developed a four-frame particle tracking method for three-dimensional PTV and established a framework to evaluate the accuracy of four algorithms to extend multiframe tracks in particle tracking methods. Each algorithm differs in the number of frames used to find the most likely position of the particle in the next step of the track, or on the cost function used to evaluate which one of the possible matches best extends the current track. Of the four different track assignment methods and cost functions explored, the

Four-Frame Best Estimate method is shown to have superior performance in homogeneous isotropic turbulence. Each particle track is initialized by choosing the particle's nearest neighbor in the next frame. The nearest neighbor initialization method works well when there is zero average flow velocity and when the particles displacement between frames is small compared to the inter-particle distance. However, it starts to fail when the particles move a distance comparable to the minimum particle-particle distance between frames. Additionally, its accuracy decreases drastically if there is an average flow that is inhomogeneous, as the mean flow can systematically bring other particles near the location of the original particle in the previous frame. If the mean flow is homogeneous or varies with time or space in a smooth and simple manner, the user can introduce a velocity guess for nearest-neighbor initialization to correct for this bias, but this method is prone to errors in the tracking when there is unsteady flow or velocity gradients, even for a simple canonical flow such as Poiseuille. This leads to incorrect tracks being measured, or correct tracks being abandoned due to uncertainty between frames.

We focus on improving the 4BE method since it has been used extensively in turbulence research since its introduction [7, 16, 18, 44, 59, 82, 90]. To do so, we introduce a modified initialization coupled with the 4BE method to increase tracking performance and increase the "yield" of tracks as a percentage of possible tracks started by particles detected in the images, while maintaining the accuracy (percentage of correct tracks from the total number of tracks reported). The proposed modified initialization method uses a customizable search in frame $n+1$ to initialize multiple tracks from a single particle position in frame n. Each of these potential tracks are then followed through the next two frames $n+2$ and $n+3$, and the cost function for each potential track is minimized only after all possible trajectories for the original particle in frame n have been considered through the three next frames. The geometry of the initialization search region and the maximum number of track candidates that are started from a single particle can be adjusted to adapt them to a large variety of flow conditions.

Two direct numerical simulation (DNS) datasets, forced homogenous isotropic turbulence and turbulent channel flow, were used to validate this new PTV initialization method and to compare its performance to the 4BE with nearest neighbor initialization. The forced isotropic turbulence dataset was used to explore tracking in a canonical setting where there is zero average velocity. In contrast, the turbulent channel flow dataset was used to look at tracking when there is a non-zero, inhomogeneous average flow. Tracking performance was then analyzed using previously introduced metrics [50, 65]. For both datasets, we show that the modified method proposed reduces tracking error and increases the track number yield, with a moderate computational cost that is affordable with modern tools. Additionally, for the turbulent channel flow, the tracking error for the modified initialization method remains significantly smaller than the tracking error for the nearest neighbor initialization even for extreme values of the non-dimensional particle displacements between image frames.

The section is organized as follows: the Four-Frame Best Estimate tracking algorithm and the modified method proposed here are introduced in Section 4.2.2; the direct numerical simulation datasets used to validate the modified initialization method are briefly described in Section 4.2.3 (a); the results from the comparison between the initialization methods are then explored in Section 4.2.3 (b); and the conclusions from this study and potential for applications are summarized in Section 4.2.4.

4.2.2 Modified Four-Frame Best Estimate Lagrangian Tracking Method with Enhanced Track Initialization

The simplest Particle Tracking Velocimetry technique, using the position of particles in two consecutive frames and choosing the nearest neighbor in frame n+1 as the most likely position of the particle in frame n, may lead to wrong matches when increasing the number of particles in the field of view and/or the displacement of particles between frames. To overcome this limitation, multiframe particle tracking methods were developed such as the four-frame particle tracking method (4BE) developed by Ouellette et al. [65]. This four-frame method uses nearest neighbor initialization and built on previous multiframe tracking algorithms by trying to minimize changes in acceleration within a particle trajectory to improve tracking performance.

Briefly, the Four-Frame Best Estimate algorithm (4BE) uses four-frames (n, $n+1$, $n+2$, and $n+3$) to reconstruct particle trajectories, as illustrated in Fig. 4.3(a). Individual tracks are initialized by using the nearest neighbor method, which chooses as the second position in the track the particle that minimizes the distance between its location in frame $n+1$ and the original particle position in frame n. Once a track is started in this way, these first two locations in the track are used to predict the position $\tilde{x}_i^{n+2}$ of the particle in frame $n+2$:

$$\tilde{x}_i^{n+2} = x_i^{n+1} + \tilde{v}_i^{n+1} \Delta t \tag{4.3}$$

where x_i^{n+1} is the position of the particle in frame $n+1$, $\tilde{v}_i^{n+1}$ is the predicted velocity, and Δt is the time between frames. A search region is then defined around this predicted location in frame $n+2$ to look for particles that are candidates to continue the track. The tolerance in the search is set to be as small as possible (usually a few pixels) since it is aimed at finding a single particle whose actual location in frame $n+2$ is closest to the prediction from frames n and $n+1$. If no particle is found, the track is abandoned. If one particle is found, the track is continued with that particle. If more than one particle is found within this search region, each one can be used to predict a set of possible track continuations $\tilde{x}_i^{n+3}$ in frame $n+3$:

$$\tilde{x}_i^{n+3} = x_i^{n+1} + \tilde{v}_i^{n+1} \left(2\Delta t\right) + \frac{1}{2} \tilde{a}_i^{n+1} \left(2\Delta t\right)^2 \tag{4.4}$$

where $\tilde{a}_i^{n+1}$ is the predicted acceleration. A search region is defined around each of the $\tilde{x}_i^{n+3}$ possible track locations and actual particle locations found in those are used to extend the track candidates from frame $n+2$ to frame $n+3$. The 4BE algorithm chooses the most likely location of the particle and, therefore, the most likely track, by minimizing the cost function ϕ_{ij}^n:

$$\phi_{ij}^n = ||x_j^{n+3} - \tilde{x}_i^{n+3}|| \tag{4.5}$$

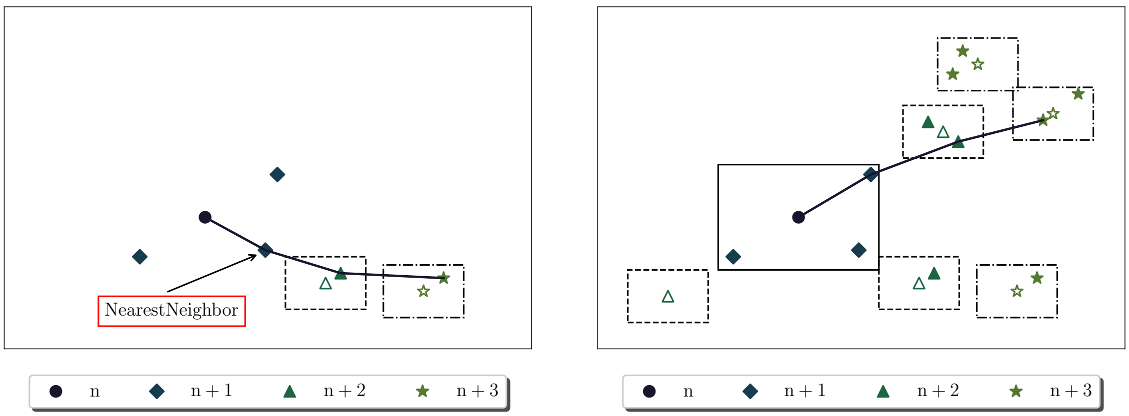

(a) (b)

Figure 4.3: Schematic comparison between tracking methods showing that our proposed tracking method with enhanced track initialization (ETI) produces a higher number of tracks and less probability of wrong tracks than existing nearest neighbor initialization (NNI) methods. Particle locations are denoted with filled symbols and predicted particle locations are denoted with hollow symbols. The track chosen by the PTV algorithm is overlaid on the actual and expected particle positions. (a) **4BE-NN** shows that the track is initialized choosing the particle position in frame $n + 1$ that is closest to the expected position of the original (n frame) particle. Only one track is initialized regardless of the information in frames $n + 2$ and $n + 3$. (b) **4BE-ETI** shows the initial search area for frame $n + 1$ (solid line box) and the three particle positions that are used to initialize three tracks in frame $n + 1$. The dotted line boxes represent search regions in frames $n + 2$ and $n + 3$ where the algorithm finds potential matches (in this example three candidates in frame $n+2$ and five follow-ups in frame $n+3$) and extends potential tracks into the next frames. The search region can be adapted to the flow conditions (inhomogeneous velocity and velocity fluctuations) for efficiency.

Equation 4.5 minimizes the distance between the actual particles x_j^{n+3} and their predicted locations $\tilde{x}_i^{n+3}$, which is equivalent to choosing the track candidate with the minimal change in acceleration of all the candidates set up in frame $n + 2$.

While 4BE with nearest neighbor initialization (4BE-NNI) is a very good compromise between low computational cost and tracking accuracy and efficiency, it discards many tracks that are incorrectly started by the nearest neighbor, thus prioritizing quick computational turn-around over the efficiency (the ratio of tracks detected to the total number of new particles where a track can be started). Additionally, there are certain cases where it can lose accuracy (the ratio of correct tracks to the total number of tracks completed). When the particle inter-frame displacement is comparable to the inter-particle distance for a significant number of particles (either because of high particle velocity fluctuations, or because of particle clustering reducing the inter-particle distance well below the median predicted from the volume fraction, or the combination of both), the percentage of bad tracks started with the nearest neighbor is high. These bad tracks will either be abandoned after frame $n + 1$ (low efficiency) or be completed erroneously in frames $n + 2$ and $n + 3$ (low accuracy).

We have developed the Enhanced Track Initialization (ETI) to complement the strengths of the 4BE method and overcome its challenges, thereby extending its applicability to highly turbulent and inhomogeneous flows with high particle density, the traditional barrier between PTV methods and time-resolved high spatial resolution Shake-The-Box-PTV or PIV. Figure 4.3(b) highlights the features of the 4BE-ETI algorithm. This method uses multiple particle locations in frame $n + 1$ (all particles found within the search region based on the estimated maximum particle displacements between two frames) to initialize, without prejudice for which one is more likely, multiple tracks. The shape and size of this initial search region is determined based on the flow characteristics (instantaneous velocity information at every point in the flow, velocity fluctuations in each direction, ...). This allows the algorithm to explore multiple possible trajectories for each particle and eliminates the assumption that the closest particle in the next frame is the only option when starting a track. Subsequent search regions in frames $n + 2$ and $n + 3$, used for track continuation, are smaller since the continuation search uses a better estimate of local particle displacement, based on the velocity and acceleration estimates from the positions found in frames n, $n+1$, and $n+2$. This decreases computational costs because it limits the number of particles found, and therefore the number of potential tracks to follow, thus limiting possible track continuations.

4.2.3 DNS Benchmark of Tracking Algorithm

Dataset Description

The performance (both in terms of tracking accuracy and efficiency) of the 4BE-ETI algorithm was analyzed and compared to the results from the traditional 4BE-NNI method using three-dimensional direct numerical simulations (DNS) available through the Johns Hopkins University Turbulence Databases [47, 68]. Two datasets were explored: forced homogeneous isotropic turbulence and turbulent channel flow [33].

The homogenous isotropic turbulence (HIT) dataset was selected to evaluate tracking when there was no mean flow. It is similar to both the DNS and the experimental datasets used to validate the original 4BE-NNI tracking algorithm [88]. The domain for the DNS of isotropic turbulence was $2\pi \times 2\pi \times 2\pi$, corresponding to a 1024^3 spectral grid, and used periodic boundary conditions. The Taylor-scale Reynolds number is $Re_\lambda = \frac{u'\lambda}{\nu} = 418$. In contrast, the turbulent channel (Channel) dataset was selected to evaluate tracking when there was a strong mean flow that is strongly inhomogeneous. The turbulent channel DNS domain was $8\pi \times 2 \times 3\pi$, with periodic boundary conditions. The friction velocity Reynolds number was $Re_\tau = \frac{U_c h}{\nu} = 10^3$.

To query the databases, the flow was initially seeded with about $50,000$ tracer particles throughout the entire volume. The particles were then advected through the domain for each time step based on the resolved DNS flow field [91]. The trajectories were then sampled in a subdomain, creating a time sequence of particle locations as their trajectories entered and left the measurement volume, as is typical in experiments. The 4BE tracking method, both with traditional NNI and the proposed ETI, was applied to the particle positions, and the tracking results were compared to the ground-truth trajectories from the DNS datasets.

Several subsets of each dataset were generated by increasing the time between frames, thus varying the particle inter-frame displacements. The number of particles in each subset was kept constant. A wide range of values of the non-dimensional displacement-spacing ratio ξ, defined as the ratio of the average distance each particle moves between frames to the average separation between particles in a given frame [50, 65], is used in this benchmarking of the tracking methods to evaluate their domain of applicability in terms of maximum particle density and maximum particle displacement between frames. When ξ is small, tracking is trivial because the particles move very little between frames and there are not many particles to consider for track continuation. However, as this non-dimensional displacement increases, tracking becomes more difficult because the particles move a large amount between frames and there are many particles that are candidates per frame to continue a track. The results of this study are shown over a wide range of ξ values, from trivial to very challenging, in terms of tracking difficulty.

Results

The performance of the different initialization methods was evaluated by looking at the tracking error, defined as [65]:

$$E_{track} = \frac{N_{imperfect}}{N_{total}} \tag{4.6}$$

where $N_{imperfect}$ is the number of tracks that contain at least one incorrect particle position (and correspondingly velocity and acceleration), while N_{total} is the total number of tracks in the dataset. A perfect track must start at the same point as the actual track and must contain no spurious locations. When E_{track} is zero, the tracking code perfectly tracks all the tracks in the DNS dataset. When E_{track} is close to or equal to one, the tracking code fails for almost every particle location, and most of the tracks in the dataset generated from the DNS are not recovered.

The results for the homogeneous isotropic turbulent flow are shown in Fig. 4.4. The Enhanced Track Initialization proposed here (4BE-ETI) performs better than the traditional nearest neighbor initialization (4BE-NNI) for this flow, where the mean velocity is zero and the inhomogeneity is low. For $\xi \lesssim 0.05$, the proposed 4BE-ETI method has zero tracking error. For $0.05 < \xi \lesssim 0.2$, the two methods follow a similar trend where the tracking error increases at approximately the same rate. For values frequently found in turbulent particle-laden flow experiments [2, 3, 5, 36] where clustering is common, $0.2 < \xi \lesssim 0.7$, the tracking error of the proposed 4BE-ETI method is half of the nearest neighbor's (4BE-NNI), extending the applicability of this multiframe PTV method. Finally, at very high ξ values ($\xi \gtrsim 0.8$), the error in the tracking reaches unacceptable values for both tracking methods tested.

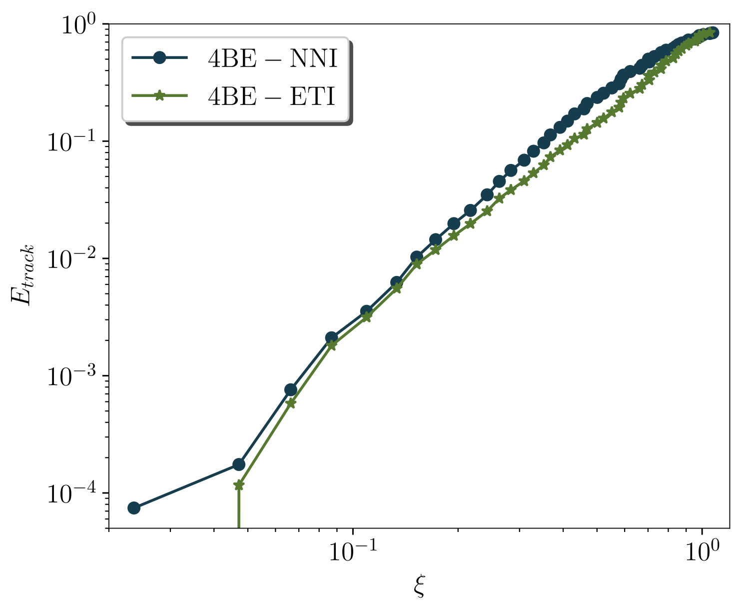

Figure 4.4: Tracking performance of the 4BE-ETI method, compared to the baseline 4BE-NNI, in forced homogeneous isotropic turbulence. At values of $\xi < 0.05$, the 4BE-ETI tracking error is zero.

Figure 4.5 shows the results of the tracking applied to the particles in turbulent channel flow. The 4BE-ETI performs significantly better than the 4BE-NNI for this anisotropic flow with spatially-variable non-zero mean velocity. For $\xi \lesssim 0.2$, there is zero tracking error when using 4BE-ETI method. For ξ values $0.2 < \xi \lesssim 0.7$, the tracking error is reduced significantly in the 4BE-ETI compared to the 4BE-NNI, up to an order of magnitude. Finally, at very high ξ values ($\xi \gtrsim 0.7$), where both methods failed in the HIT flow, the tracking error for the 4BE-ETI continues to be much smaller than for the 4BE-NNI, and has about 10-20% of incorrect tracks even at these high values of ξ. This shows significant advantage of the Enhanced Track Initialization method for inhomogeneous and anisotropic flows where the error is significantly smaller and usage of the method is possible even at high ξ values.

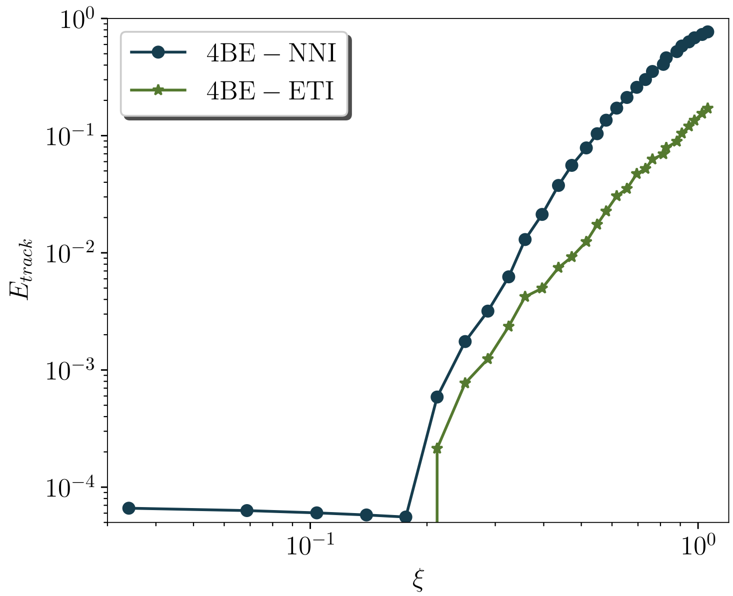

Figure 4.5: Tracking performance of the 4BE-ETI method, compared to the baseline 4BE-NNI, in a turbulent channel flow. At values of $\xi < 0.2$, the 4BE-ETI tracking error is zero.

However, from Figs. 4.4 and 4.5, we see that ξ is an incomplete metric to compare tracking performance in different types of turbulent flows where the mean flow magnitudes differ and the levels of inhomogeneity and anisotropy vary from negligible to dominant. The

4BE-NNI tracking algorithm has a lower tracking error up to higher ξ values in the turbulent channel than in the homogenous isotropic turbulence. This discrepancy is due to the fact that ξ does not correctly consider turbulent fluctuations, or spatial inhomogeneity of the mean and fluctuating velocities. Therefore, we propose an additional metric ξ', defined as the ratio of the average displacement of a particle between frames due to turbulent fluctuations to the average separation between particles in a given frame, to more accurately compare the tracking in these two different types of turbulent flows. If there are strong turbulent fluctuations, tracking becomes more difficult because the velocity and acceleration predictions used to continue the tracks become less accurate. Like ξ, when ξ' is small, tracking is trivial because the particles move very little between frames and there are not many particles to consider for track continuation. However, as this ratio increases, tracking becomes more difficult because there are more turbulent fluctuations or there are more particles per image, or both. For $\xi' \lessapprox 0.2$, we see that the 4BE-NNI (HIT) and 4BE-ETI (both Channel and HIT) algorithms perform similarly and have tracking errors lower than 20%. In the channel flow, the 4BE-NNI method performs worse than 4BE-ETI since the initialization fails in an inhomogeneous mean flow (even at smaller ξ', the performance of 4BE-NNI is significantly worse than 4BE-ETI). At higher values of ξ', the results for the two datasets begin to diverge, which is most likely due to increased tracking difficulty at these high ξ' values, where the advantages of the novel 4BE-ETI are more pronounced.

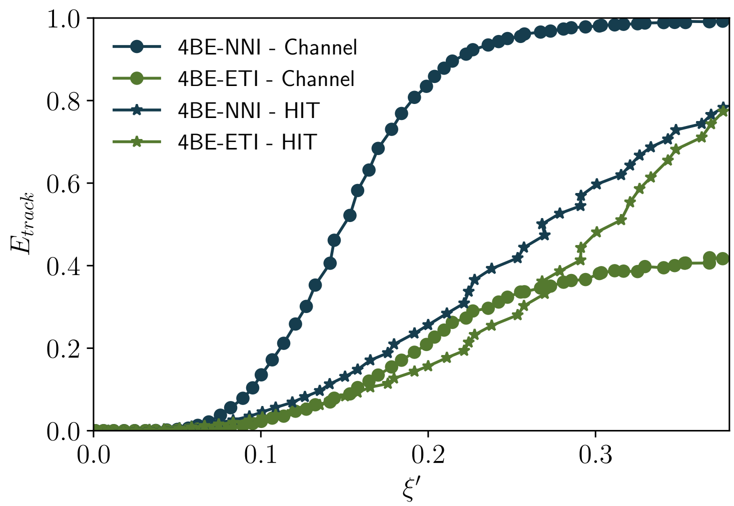

Figure 4.6: Tracking performance of the 4BE-ETI method, compared to the baseline 4BE-NNI, in both forced homogeneous isotropic turbulence and a turbulent channel flow evaluated using ξ', based on turbulent fluctuations.

4.2.4 Conclusion

The method used for initialization of the particle tracks in multiframe PTV influences tracking performance strongly. We have shown that the Enhanced Tracking Initialization proposed allows the four-frame best estimate particle tracking method to perform significantly better than the nearest neighbor initialization. In turbulent channel flow, where the inhomogeneity and anisotropy of the flow presents a challenge to the nearest neighbor, 4BE-ETI has a tracking error up to an order of magnitude lower over a wide range of ξ values, extending its applicability to densely seeded flows or flows where the inter-frame time is limited by the camera frame rate or laser repetition rate. The 4BE-ETI method proposed here also reduces error in tracking by approximately 50%, with respect to the 4BE-NNI, in homogeneous isotropic turbulence. This highlights the flexibility of the 4BE-ETI to choose search region size and shape based on the flow characteristics to optimize accuracy and efficiency without undue increases in computational time. Additionally, automated strategies can be easily implemented by running the tracking on a small subset of particles, equally spaced along the flow domain, with a large initialization region to obtain coarse information about the flow and recursively using this information to refine the initial search region geometry in an increasing number of particles for subsequent passes.

Chapter 5

RESULTS FROM THE ULTRASOUND IMAGING EXPERIMENTS

Chapter 2 discussed the current understanding of the dynamics of microbubbles under different confinement conditions: infinite fields, rigid-walled tubes, and compliant vessels. It also introduced the primary Bjerknes force. The experiments described in this chapter were conducted to explore the behavior of microbubbles under different physiologically-relevant flow conditions and ultrasound parameters. The first experiments will show microbubble behavior in a large (9.5 mm diameter) silicone tube in a quiescent fluid. The experiments were then extended to study of the behavior of microbubbles in steady flow under ultrasound excitation. Finally, the chapter concludes by looking at the response of microbubbles to ultrasound in pulsatile flow. Additionally, the contributions made to the methodology of Particle Tracking Velocimetry (PTV) use for clinical ultrasound imaging are described where appropriate.

5.1 Bjerknes Force on Microbubbles

This chapter uses ultrasound imaging to investigate the behavior of microbubbles under three different flow conditions: no flow, uniform flow, and pulsatile flow. The experimental setup is described in detail in Section 3.3.1. The same peristaltic pump was used for both steady and pulsatile flow experiments. In these experiments, two different pulse dampeners were used to reduce the velocity time variations produced by the pump. The steady flow experiments used a larger pulse dampener to remove the pulsatility from the peristaltic pump from the flow, creating a steady and fully developed velocity field in the test section (the time-dependent fluctuations in velocity coming from the pump are completely damped by the time they reach the test section). The pulsatile flow experiments used a smaller pulse dampener that acts as a low pass filter, reducing the amplitude of potential high frequency fluctuations in the flow. Experiments conducted without a pulse dampener will not be presented in this chapter, as the high frequency decelerations and accelerations in the test section created significant out of plane movement in the flow, causing microbubble tracking to produce inconsistent or inaccurate results. For completeness, Figure 5.1 shows how the velocity waveforms change using no pulse dampener, the small pulse dampener, and the large pulse dampener. When there is no pulse dampener, the velocity amplitude varies between zero and a maximum value that is dependent on the speed of the pump. With the small pulse dampener, the waveform looks very similar; however, the amplitude of the velocity profile is decreased slightly. Finally, with the large pulse dampener, the amplitude is decreased even more significantly and the flow becomes steady.

5.1.1 Experiments of Ultrasound Forcing on Microbubbles with No Flow

Experiments were conducted at different ultrasound parameters without flow. These experiments examine the behavior of microbubbles purely under ultrasound excitation, without the presence of any hydrodynamic forces associated with flow, and gain insight into the parameter space to explore (in terms of pressure amplitude and number of cycles) for the experiments that followed. First, the effect of pressure amplitude on microbubble response was explored. The V303 pushing transducer was turned on for 10 seconds. Ultrasound images were taken during this 10 second period and then continued for another $1 - 2$ seconds after the ultrasound was turned off to examine the void in the microbubbles created by the ultrasound. After each experiment, flow was turned on for 5 seconds to wash out the fluid that had been insonated and flow new microbubbles in solution to replenish the test section. After this time, the microbubbles were allowed to rest for 10 more seconds before the US forcing was turned on again and another experiment was performed.

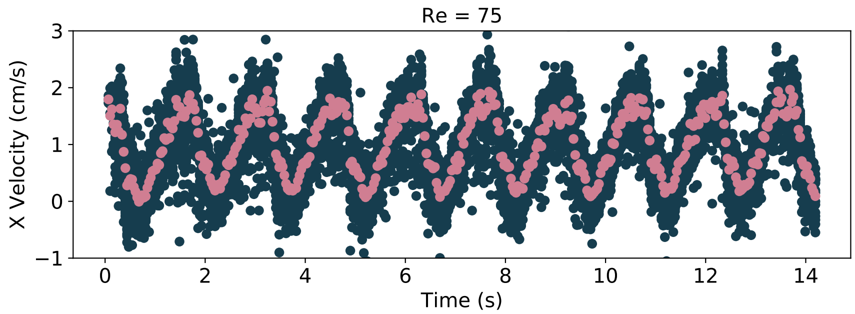

(a)

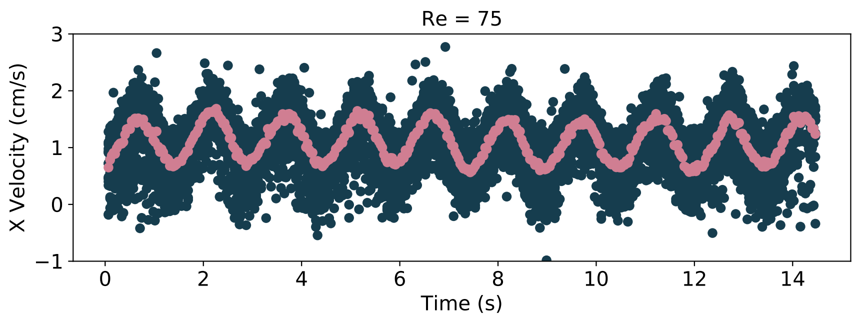

(b)

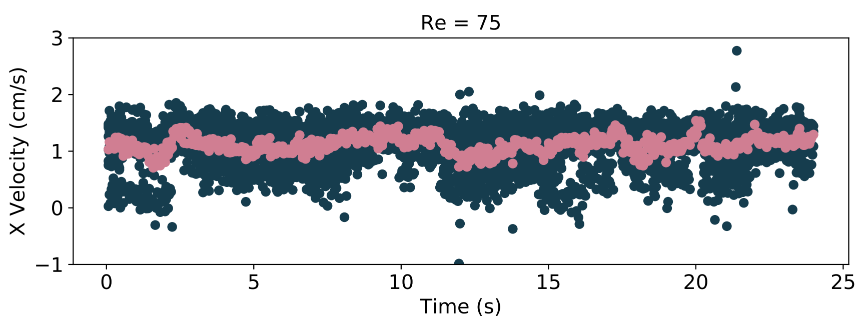

(c)

Figure 5.1: Profiles of x velocity over time obtained from selected ultrasound videos. The blue dots are all the velocity point calculated from the trajectories obtained from using PTV on the ultrasound videos. The pink dots are the spatial average of the x velocity for each image in the video. (a) The velocity waveform obtained using no pulse dampener for$Re = 75$. (b) The velocity waveform obtained using the small pulse dampener for $Re = 75$. The amplitude of the oscillations is decreased due to the pulse dampener. (c) The velocity waveform obtained using the large pulse dampener for $Re = 75$. The amplitude is sufficiently damped and the flow becomes steady.

Figure 5.2 shows the change in the Bjerknes force as a function of pressure amplitude. The void in the tubing shows the extent to which the microbubbles were pushed out of the test section by the propagating ultrasound pressure field. At the smallest amplitudes values ($P_A = 0.05$ MPa), there is no noticeable effect on the microbubbles from the ultrasound. As the pressure is increased up to $P_A = 0.28$ MPa, there are noticeable differences in the microbubble response. At $P_A = 0.11$ MPa, there is a very narrow region void of bubbles along the axis of propagation of the ultrasound beam, where the intensity of the pressure fluctuations is highest. This suggests that microbubbles are only affected by the ultrasound if they are located in the very center of the propagating beam. As the pressure increases further, the size of the void region starts to widen: effective bubble pushing is no longer only localized at the center of the incoming ultrasound beam. At higher pressure amplitudes, it is difficult to discern if the void is caused due to the displacement or destruction of microbubbles. At the highest pressure amplitudes, there is noticeable microbubble destruction, with microbubbles being eliminated from the fluid in the test section along the area insonated by the transducer, as evidenced by the void in the entire imaged area of the tube. Additionally, it was obvious in the experiments that destruction was occurring at these higher pressure values because the void appeared almost instantaneously (on the order of milliseconds); this was much faster than the time scale observed when the microbubbles were being pushed.

Figure 5.3 extends these experiments and shows the change in the Bjerknes force as a function of both pressure amplitude and number of cycles. The pressure amplitudes examined were 0.11 MPa and 0.17 MPa because the dynamics of the microbubbles at these pressure amplitudes is primarily due to pushing (not bubble destruction). Here, the effect of the number of cycles per excitation pulse is examined further. As the number of cycles (and thus the duty cycle) increases, the region void of bubbles gets noticeably larger in the images. However, the effect on the microbubbles due to increasing cycles is much smaller than that observed by increasing pressure amplitudes. It is also interesting to observe that some destruction seems to be occurring at the very center of the ultrasound beam at 0.17 MPa (highlighted by the darker void, clear of even the smallest bubbles, in the center region).

However, unlike at higher pressures, pushing is still occurring at the edges of the ultrasound beam. As a result, 0.17 MPa was chosen as the upper limit of pressure amplitudes to be used in the experiments with steady or pulsatile flow that followed.

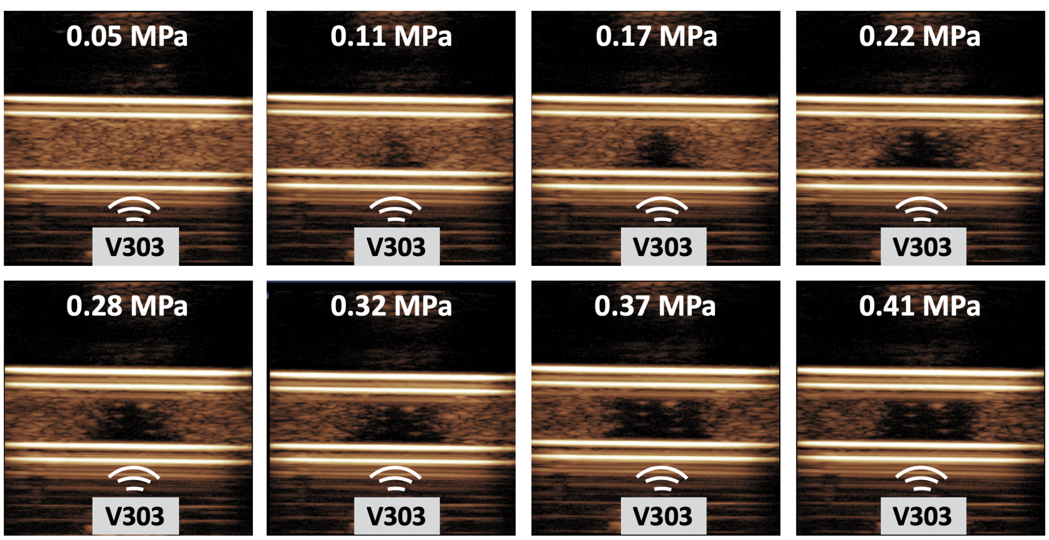

Figure 5.2: Experimental results showing microbubble behavior in a quiescent fluid under ultrasound excitation at different ultrasound pressure amplitudes. As the pressure amplitude is increased, there is a larger region void of bubbles created in the test section. At the highest pressure amplitudes, the shape of the void region changes suggesting that microbubble destruction is occurring.

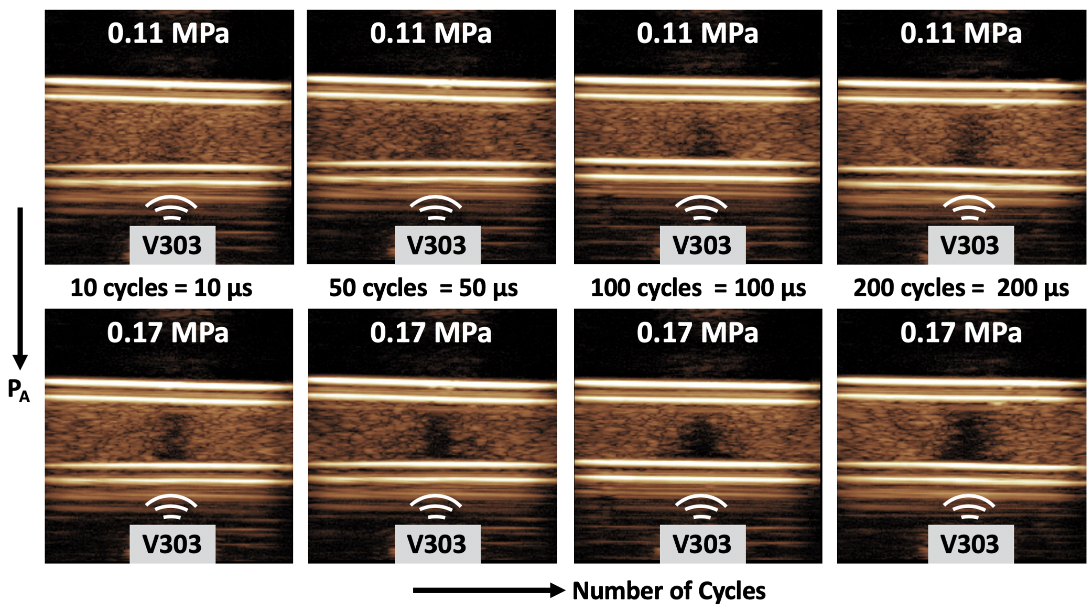

Figure 5.3: Experimental results showing microbubble behavior in a quiescent fluid under ultrasound excitation at different ultrasound pressure amplitudes and cycles. The region void of bubbles becomes larger with both increasing amplitude and number of cycles.

5.1.2 Experiments of Ultrasound Excitation of Microbubbles in Steady, Fully-Developed, Flow

The bubbles-in-quiescent-fluid experiments were then extended to explore the response of microbubbles in steady flow to ultrasound excitation. For these experiments, ultrasound image sequences were taken using the iU22 imaging transducer. These videos typically ranged in duration between 5 and 20 seconds depending on the acquisition speed of the ultrasound imaging transducer. At higher frame rates, the memory buffer filled faster and, therefore, shorter videos (same number of frames but shorter recording time due to the higher frame rates) were acquired. The experiments discussed here are based on videos collected in harmonic imaging mode at 30 Hz. After the videos were recorded, the resulting images were processed in MATLAB according to the methods discussed in Section 4.1.1. Once the centroids of the microbubbles were detected, the trajectories of the microbubbles were calculated using the PTV methods discussed in the previous chapter. Initialization of microbubble trajectories is shown in Figure 5.4. The bounding box sizes used in the PTV code were adjusted to enable the tracking of the microbubble locations in the images, following the angled orientation in the US transducer imaging.

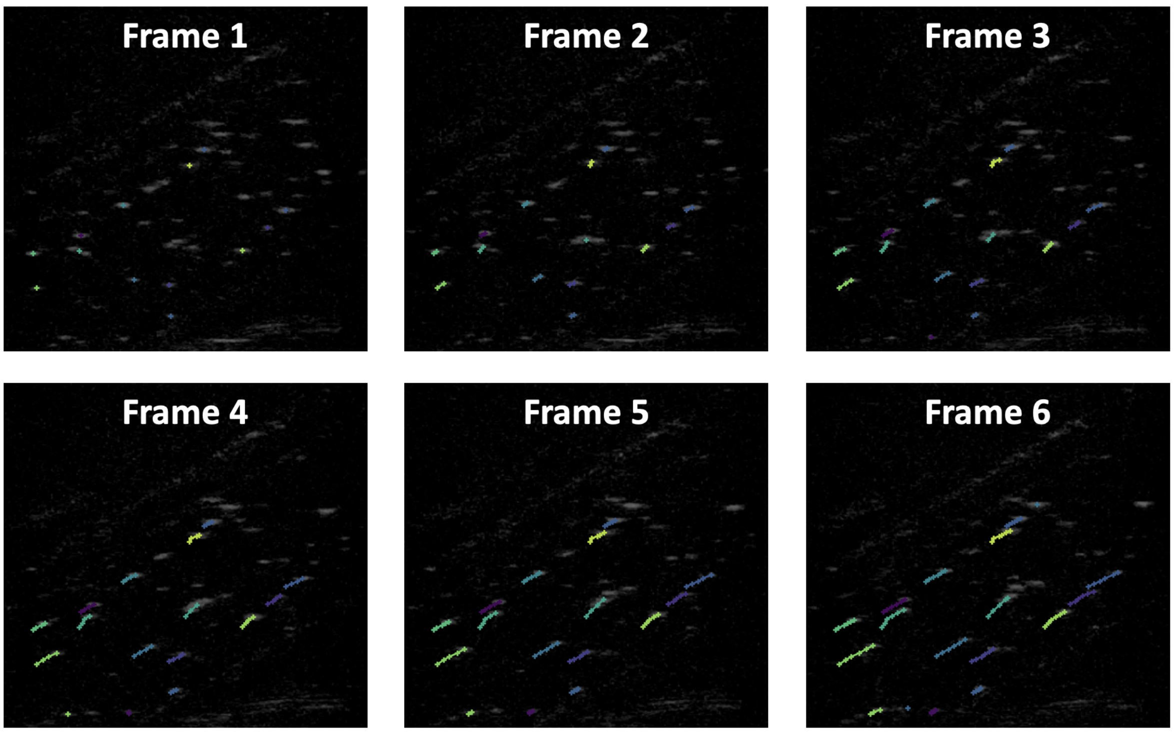

Figure 5.4: Evolution of PTV algorithm in US images. The trajectories are started in Frame 1 and are then built up over the continuing frames.

Figure 5.5 shows trajectories that were obtained from a typical ultrasound video. The microbubbles closer to the inlet of the tube (near the arrow indicating flow direction in the video) are not being affected by the ultrasound. Additionally, the microbubbles in the center of the tube are moving faster than the microbubbles at the edge of the tube, as expected in a Poiseuille flow profile. This can be observed by looking at the spacing between dots (each corresponding to a different image frame). Towards the top of the tube, the dots along a trajectory are very close together, indicating the microbubble did not move much between image frames. In the center of the tube, however, the dots are spaced further apart, indicating that the microbubbles are moving faster in this region. Finally, there is an obvious change in the trajectories of the microbubbles when they cross the ultrasound pressure field. The purple trajectory demonstrates how a microbubble is pushed away from the transducer due to the Bjerknes force as it crosses the US beam.

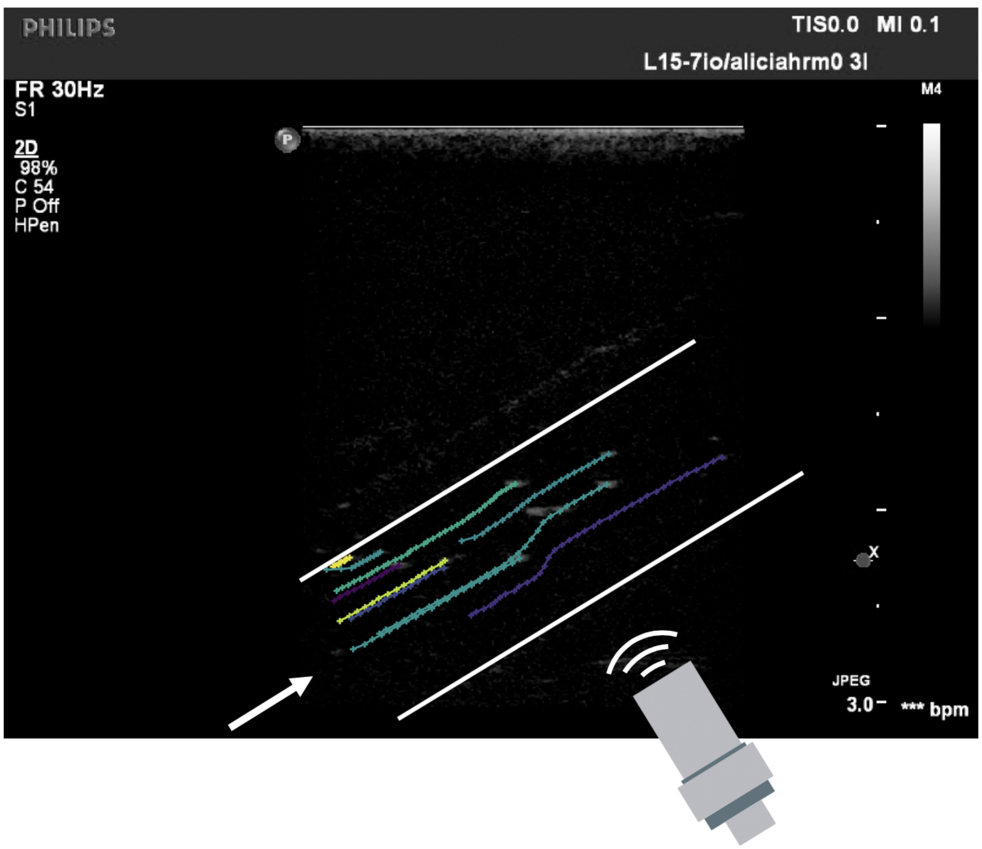

Figure 5.5: Microbubble trajectories obtained using PTV on the US imaging loops. The microbubbles near the front of the transducer are noticeably displaced in the image.

These ultrasound videos were acquired at two Reynolds numbers and a range of ultrasound parameters. Table 5.1 summarizes the experimental conditions for the steady flow experiments.

Re $Re = \frac{\rho v D}{\mu}$	P_A (MPa)	Number of Cycles (Duty Cycle)
75	0.07, 0.10, 0.12, 0.14	13, 26, 40, 53 (10%, 20%, 30%, 40%)
150	0.07, 0.10, 0.12, 0.14	13, 26, 40, 53 (10%, 20%, 30%, 40%)

Table 5.1: Parameters explored in the uniform flow experiments

Figure 5.6 shows the x velocity as a function of tube radius for two Reynolds numbers. Since the flow is steady, the data is temporally averaged and then binned in 10 pixel increments along the radius of the tube. The trajectories have been rotated so that the x axis of the figure is now the plane parallel to the front of the pushing transducer, and the y axis is perpendicular to the front of the pushing transducer. This coordinate system will be used for all experimental results in this chapter, since the focus is on the microbubble response along the axis of the transducer. Figure 5.6 (a) shows the x velocity profile at a Reynolds number of 75 (De = 33). A Poiseuille velocity profile is found at this Reynolds number. As expected, the maximum velocity occurs at the centerline of the tube and the profile is axisymmetric. Figure 5.6 (b) shows the x velocity profile at a Reynolds number of 150. At this higher Reynolds number (De = 65), the velocity profile is shifted towards the upper wall due to the curvature at the inlet of the tubing.

Further analysis can be performed on these ultrasound videos to determine how the pressure amplitude and number of cycles affects the microbubble response to the ultrasound. The y displacement (along the axis perpendicular to the US pushing transducer) was calculated for each video. Figure 5.7 shows how the y displacement was calculated for an individual microbubble trajectory. The radial position of the first four starting points of the trajectory was averaged, as well as the radial positions of the last four end points. The difference between these two average radial positions was then calculated to get an idea of typical microbubble displacement. If the microbubble was not affected by the ultrasound, the y displacement would be zero.

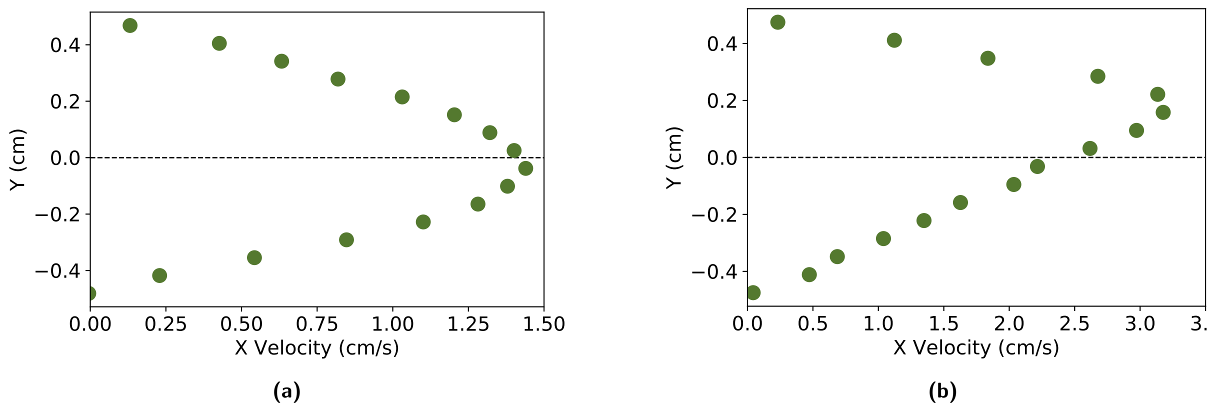

Figure 5.6: Schematic showing the x velocity along the tube axis. (a) At a Reynolds number of 75 ($De = 33$), there is no effect of vessel curvature and the profile is symmetric about the center line. (b) At a larger Reynolds (Re=150) and Dean number ($De = 65$), the velocity profile is shifted due to the curvature of the vessel prior to the test section.

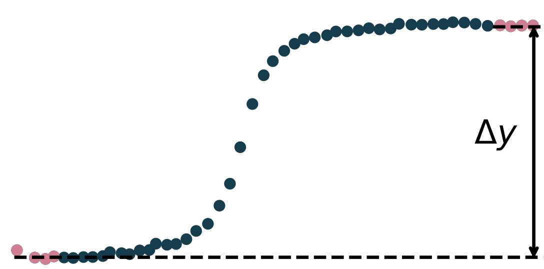

Figure 5.7: Schematic showing the change in a microbubble trajectory due to the primary Bjerknes force. The beginning and end points of the trajectory can be used to calculate the change in y-position Δy. This metric can be used to explore how different pressure amplitudes and ultrasound cycles affect the microbubble displacement.

Figure 5.8 shows graphs of the probability density functions (PDFs) of the y displacement at varying pressure amplitudes from 0.07 to 0.12 MPa and Reynolds numbers of 75 and 150 for a fixed number of ultrasound cycles. For all of the experimental realizations, the mean y displacement is very close to zero (as expected in Poiseuille flow). In the images, the most probable case for the microbubbles being tracked is that they are not being influenced by the ultrasound pressure field. Therefore, the tails of the probability distributions are more interesting than the peak because they represent the displacement of the small number of microbubbles that are being pushed when they cross the ultrasound beam. Figure 5.8 (a) shows the effect of varying pressure amplitude at a Reynolds number of 75. At the lowest pressure value (0.07 MPa), the ultrasound force is very small, so there is only a small probability of a negative (away from the propagating pressure wave) y displacement due to pushing. As the pressure increases, the tails of the PDF get longer and taller, consistent with the theoretical prediction that the Bjerknes force depends quadratically with the pressure amplitude. The microbubbles in these ultrasound fields have a higher probability of sensing more of an effect of the propagating ultrasound wave. Figure 5.8 (b) shows similar trends for a Reynolds number of 150. However, the microbubbles are being displaced less in the y direction for this higher Reynolds number (higher flow rate). This is due to the fact that the microbubbles reside in the ultrasound field for a shorter amount of time than at the slower Reynolds number. This suggests that the beam width of the transducer becomes more important as the Reynolds number increases. For steering applications, a larger diameter transducer may be desired so that the microbubbles spend more time in the ultrasound field.

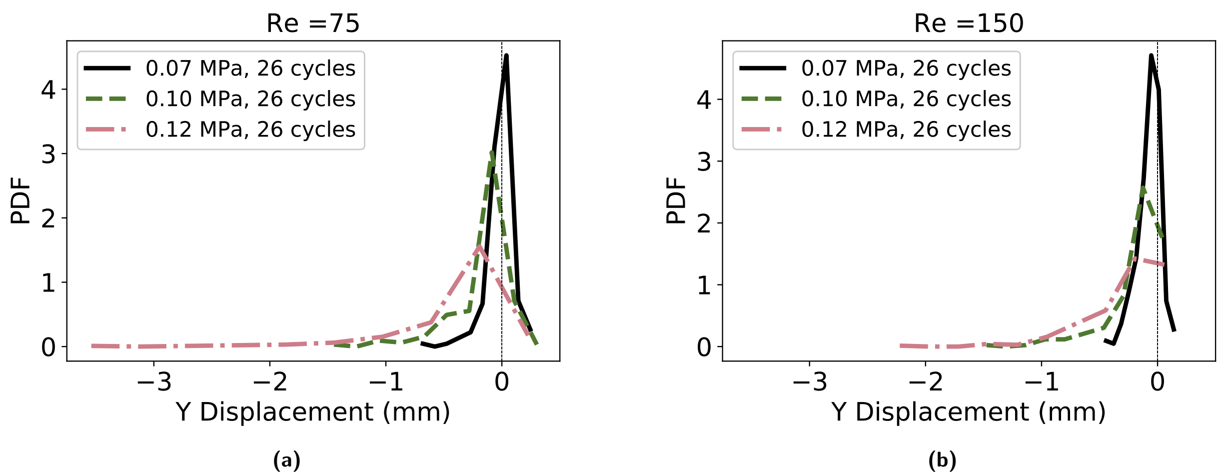

Figure 5.8: Probability density functions (PDF) of the y displacement at varying pressure amplitudes and Reynolds numbers for a fixed number of ultrasound cycles. (a) The y displacement at a Reynolds number of 75. The microbubbles see more of an effect of the ultrasound (corresponding to an increased tail length) as the pressure amplitude is increased. (a) The y displacement at a Reynolds number of 150. The microbubbles still see more of an effect of the ultrasound as the pressure amplitude is increased, although the maximum y displacement is decreased compared to the Reynolds number of 75 case.

Figure 5.9 looks at how the y displacement varies when the number of ultrasound cycles is varied from 13 to 53 (10 to 40% duty cycle) and the pressure amplitude is fixed. Figures 5.9 (c) and (d) show a zoomed in view of the tails of the PDFs. Figure 5.9 (a) shows the effect of varying the number of ultrasound cycles at a Reynolds number of 75. At the lowest number of cycles, the ultrasound force is very small, so there is only a small probability of y displacement due to pushing. As the number of cycles increases, the tails of the PDF get longer. However, unlike in Figure 5.8, the tails of the PDF are more uniformly spaced; there is no large jump between tails as seen previously for the varying pressure amplitudes. This is consistent with the Bjerknes force being linearly proportional to the number of excitation cycles, duty cycle or PRF of the ultrasound, as opposed to the stronger, quadratic, dependency observed for the Bjerknes force with the excitation pressure amplitude. Figure 5.9 (b) shows similar trends for a Reynolds number of 150. However, the microbubbles are being displaced less in the y direction for this higher Reynolds number (higher flow rate) since the microbubbles traverse the ultrasound beam more quickly.

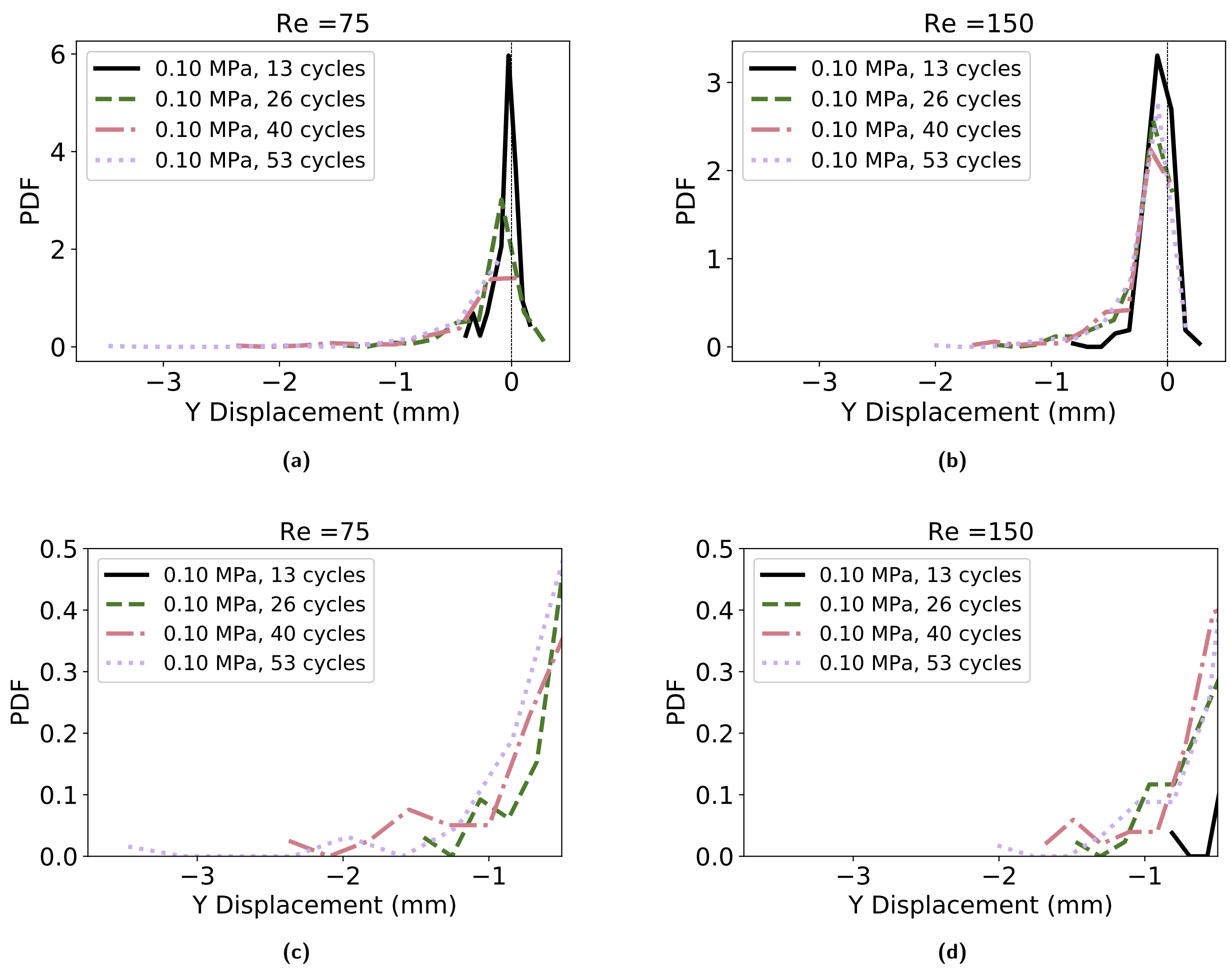

Figure 5.9: Probability density functions (PDF) of the y displacement at varying ultrasound cycles and Reynolds numbers for a fixed pressure amplitude. (a) The y displacement at a Reynolds number of 75. The microbubbles see more of an effect of the ultrasound (corresponding to an increased tail length) as the number of cycles is increased. (a) The y displacement at a Reynolds number of 150. The microbubbles still see more of an effect of the ultrasound as the number of cycles is increased, although the maximum y displacement is decreased compared to the Reynolds number of 75 case. (c) and (d) show a zoomed in version of the tails of the PDFs to get a close up view of how the tail length varies with number of cycles.

PDFs of the y-component of the velocity can also be explored to quantify the Bjerknes force acting on the microbubbles. Figure 5.10 shows graphs of the probability density functions of the y velocity at varying pressure amplitudes and Reynolds numbers for a fixed number of ultrasound cycles. Figure 5.10 (a) shows the effect of varying pressure amplitude at a Reynolds number of 75. At the lowest pressure value (0.07 MPa), the ultrasound force is very small and the tails of the PDF are almost symmetric. However, as the pressure increases, the PDFs lose their symmetry and the tails become longer and taller at negative y velocities, representing the microbubbles that are pushed due to the propagating ultrasound wave. Figure 5.10 (b) shows the effect of varying pressure amplitude at a Reynolds number of 150. The tails of the PDF for negative y velocities increase with increasing pressure amplitudes. At the lowest pressure amplitude (the black lines in the figures), the PDF is almost symmetric since there is not a large effect since the ultrasound is very weak.

The magnitude and probability of negative y velocities at each pressure amplitude are similar to those at the lower Reynolds number ($Re = 75$), showing that the Bjerknes force is acting on the microbubbles regardless of the Reynolds number of the flow. Since the bubbles have no inertia (negligible mass and very small added mass given their small size, $1 - 5$ μm), the forces on the bubble are always in equilibrium. The Bjerknes force is balanced by the y-component of the drag that is linear with the y-component of the bubble velocity at the infinitesimal Reynolds number of the bubble ($Re_{bubble} \approx 10^{-2}\ m/s \cdot 10^{-6}\ m/3.5\ 10^{-6}\ m^2/s \approx 3\ 10^{-3}$). Thus, the magnitude and probability of the Bjerknes force on the microbubbles are similar to the PDFs of the y velocity, showing that it is acting equally on the microbubbles regardless of the flow Reynolds number. This is in contrast with the different displacements for the different Reynolds number cases, which can be easily explained as the displacement is the product of the average velocity experienced by the microbubble as a result of the Bjerknes force (constant with Re) by the residence time in the ultrasound excitation beam, which is linearly proportional to the inverse of the x-component of the velocity (and thus to the Re).

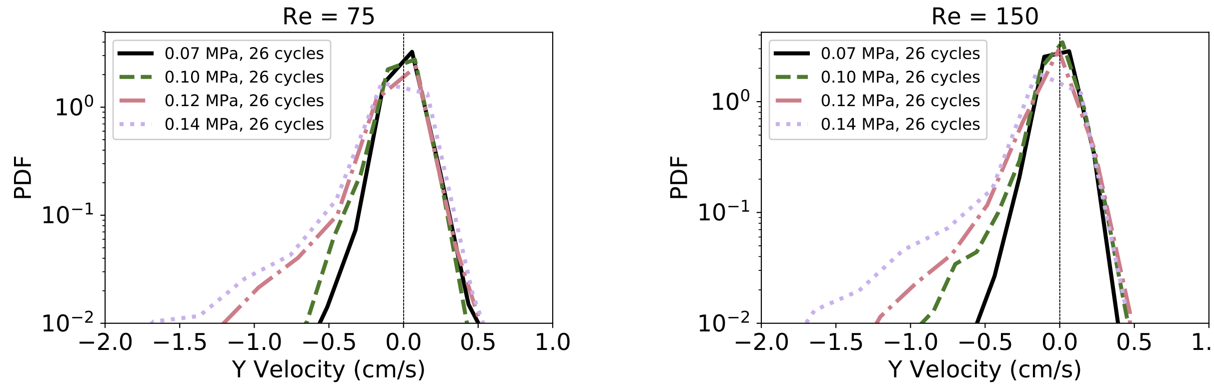

(a) (b)

Figure 5.10: Probability density functions (PDF) of the y velocity at varying pressure amplitudes and Reynolds numbers for a fixed number of ultrasound cycles. (a) The y velocity at a Reynolds number of 75. The microbubbles see more of an effect of the ultrasound (corresponding to an increased tail length) as the pressure amplitude is increased. (a) The y displacement at a Reynolds number of 150. The microbubbles still see more of an effect of the ultrasound as the pressure amplitude is increased, although the maximum y displacement is decreased compared to the Reynolds number of 75 case.

Figure 5.11 shows the probability density functions of the y velocity plotted for varying numbers of ultrasound cycles and Reynolds numbers, at a fixed pressure amplitude. Figure 5.11 (a) shows the effect of varying the number of cycles at a Reynolds number of 75. At the lowest number of ultrasound cycles (13 cycles), the ultrasound force is very small and the tails of the PDF are almost symmetric. However, as the number of cycles increases, the PDFs lose their symmetry and the tails become longer and taller at negative y velocities representing the microbubbles that are subjected to the Bjerknes force by the propagating ultrasound wave. Figure 5.11 (b) shows the effect of varying the number of cycles at a Reynolds number of 150. The tails of the PDF for negative y velocities increase with increasing pressure amplitudes. The length of the tails of the negative y velocities are similar to those at the lower Reynolds number (Re = 75), with the exception of some fluctuations in the tails at 26 and 53 cycles. Finally, the effect of the ultrasound is much less pronounced when the number of cycles is varied compared to when the pressure amplitude is varied. When the pressure is doubled, there is a much greater disparity between the tail lengths than when the number of cycles is doubled, consistent with the Bjerknes force being quadratic with the pressure amplitude but linear with the number of cycles (duty cycle).

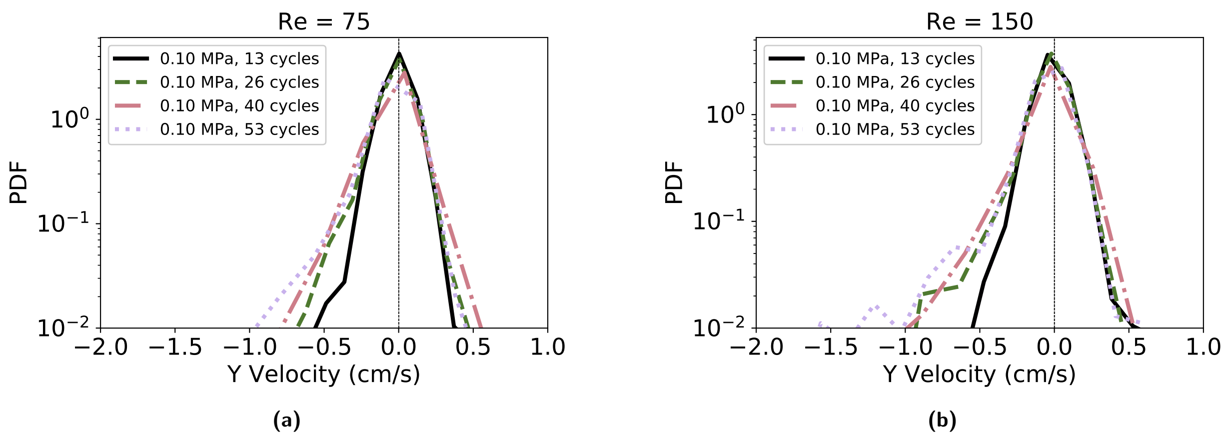

Figure 5.11: Probability density functions (PDF) of the y velocity at varying ultrasound cycles and Reynolds numbers for a fixed pressure amplitude. (a) The y velocity at a Reynolds number of 75. The microbubbles see more of an effect of the ultrasound (corresponding to an increased tail length) as the number of cycles is increased. (a) The y velocity at a Reynolds number of 150. The microbubbles still see more of an effect of the ultrasound as the number of cycles is increased, although the maximum y displacement is decreased compared to the Reynolds number of 75 case.

These experimental results present a significant contribution to experimental studies of the Bjerknes force acting on microbubbles at physiologically-relevant Reynolds number flows. Previous experimental studies examined microbubble behavior under ultrasound excitation in a 200 μm cellulose tube. In our experimental study, for the similar ultrasound settings as seen in [23, 24, 79], we see a much larger y displacement since our tube is an order of magnitude larger. In these previous experimental works, the y displacement was typically on the order of μm; whereas, our results show displacements on the order of mm. Additionally, due to our larger tubing size, we are able to look at higher Reynolds numbers, which are closer to those seen *in vivo*. Finally, we also developed a novel particle tracking velocimetry method that could be used with ultrasound imaging and a clinical ultrasound system. This opens up many possibilities for future studies with ultrasound imaging, especially with the higher frame rates available in research ultrasound systems.

5.1.3 Ultrasound Experiments in Pulsatile Flow

The final set of experiments described in this chapter focuses on the behavior of microbubbles in pulsatile flow at Reynolds numbers of 75, 112, and 150 to determine the change in microbubble dynamics under unsteady flows. The unsteadiness of flow is characterized by the nondimensional Womersley number (Eq. 3.3). Table 5.2 summarizes the experimental conditions for the pulsatile flow experiments.

Reynolds Number $Re = \frac{\rho v D}{\mu}$	Womersley Number $\alpha = \frac{D}{2}\sqrt{\frac{\omega}{\nu}}$	P_A (MPa)	Number of Cycles
75	10.3	0.07, 0.10, 0.12	13, 26, 40
112	12.6	0.07, 0.10, 0.12	13, 26, 40
150	14.6	0.07, 0.10, 0.12	13, 26, 40

Table 5.2: Parameters explored in the pulsatile flow experiments

The small pulse dampener was used to decrease the amplitude of the high frequency fluctuations in these experiments, in order to make the tracking possible to implement while still maintaining the physiologically-relevant pulsatility of the flow. Figure 5.12 highlights the position of the velocity peaks over the cardiac cycle, to help discern the peaks at the higher Reynolds numbers. These peak locations will be used in the data analysis to phase average the data (average tracking data that occurs at the same point in the velocity cycle).

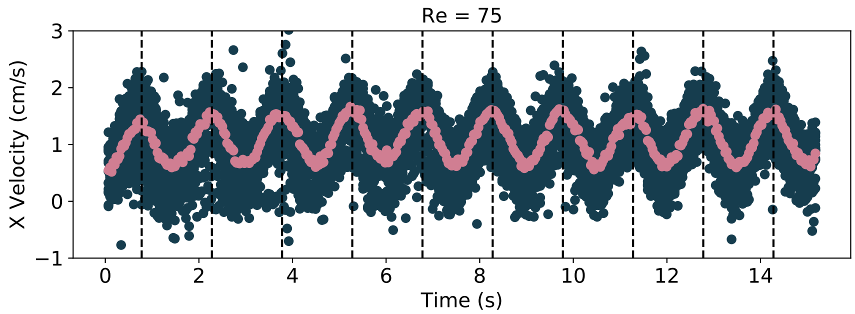

(a)

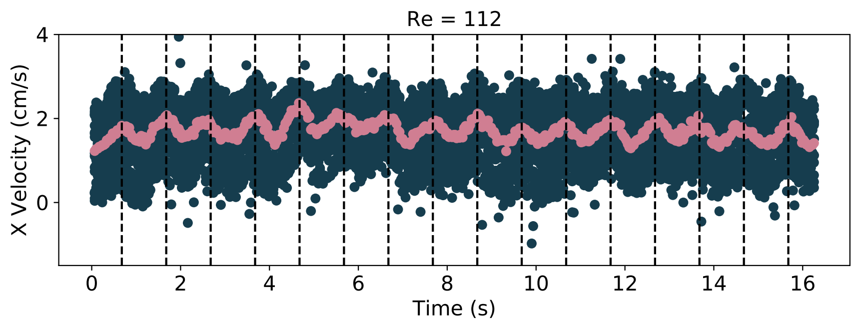

(b)

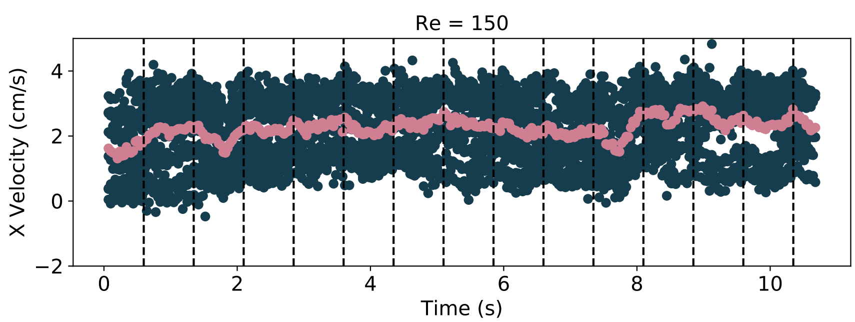

(c)

Figure 5.12: Profiles of x velocity over time obtained from selected ultrasound videos. The blue dots are all the velocity point calculated from the trajectories obtained from using PTV on the ultrasound videos. The pink dots are the spatial average of the x velocity for each image in the video. (a) The velocity waveform obtained using the small pulse dampener for $Re = 75$. (b) The velocity waveform obtained using the small pulse dampener for $Re = 112$. The amplitude of the fluctuations is decreased due to the pulse dampener. (c) The velocity waveform obtained using the small pulse dampener for $Re = 150$. The amplitude is significantly dampened at this higher Reynolds number since the pulse dampener acts as a low pass filter.

Similarly to the uniform flow analysis, we can also explore the y displacement in the pulsatile flow experiments. Figure 5.13 shows PDFs of the y displacement at a fixed Reynolds number ($Re = 75$). Figure 5.13 (a) shows how the y displacement varies when the pressure amplitudes are varied from 0.07 to 0.10 MPa at a fixed number of cycles (26). Figure 5.13 (b) shows how the y displacement varies when the number of ultrasound cycles is varied from 13 to 40 (10 to 30% duty cycle) and the pressure amplitude is fixed at 0.10 MPa. Not surprisingly, the y displacement values are larger than those seen in the steady flow experiments (Figures 5.9 and 5.8). This is due to the pulsatility in the flow: the y velocity measured for the bubbles depends on the phase of the cardiac cycle, associated with the residence time of the bubbles in the acoustic beam. For the phases when the x-velocity is low, bubbles have a much longer residence time in the beam and therefore spend more time moving at the local value of the y-velocity, proportional to the Bjerknes force driven by the local acoustic forcing, reaching a much larger y displacement, as shown in the figure. This behavior is beneficial for pushing applications because it suggests that there is an optimal time in the cardiac waveform to manipulate the microbubbles. For example, if the microbubbles are insonated when the flow is decelerating and approaching its minimum value, the bubbles would be displaced further since they have a longer residence time. Additionally, the duty cycle was kept low to avoid possible cavitation or other thermo-mechanical damage mechanisms.

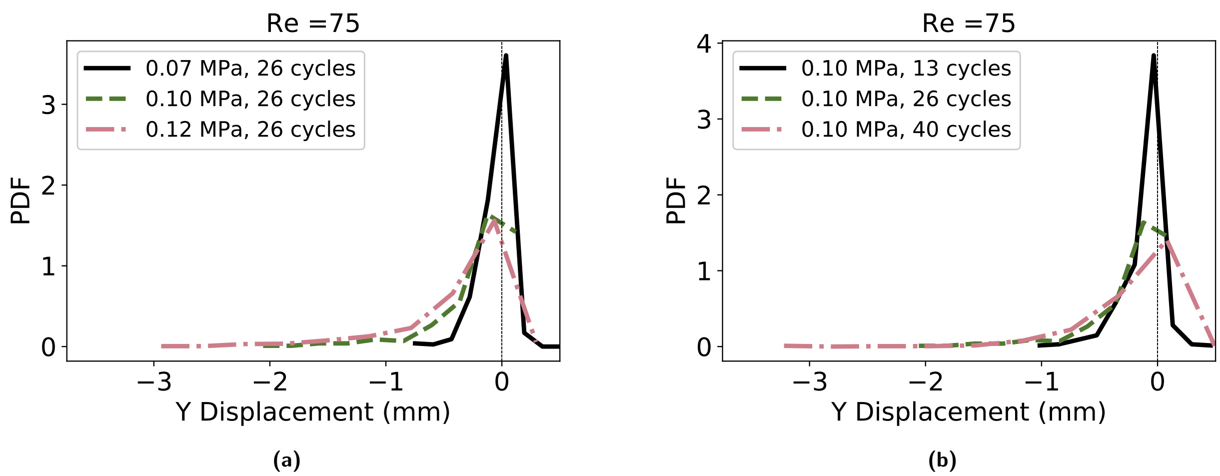

Figure 5.13: Probability density functions (PDF) of the y displacement at a Reynolds number of 75 with varying numbers of cycles and pressure amplitudes. (a) The PDF of y displacement for varying pressure amplitudes at a fixed number of cycles, 26. (b) The PDF of y displacement for a varying number of cycles at a fixed pressure amplitude of 0.10 MPa.

While we expect the y-displacement PDFs to change due to pulsatility, the y velocities would be expected to remain unchanged compared to the steady case. Since, in the absence of inertia, the y velocities are linearly proportional to the Bjerknes force, we expect the y velocity magnitudes to have the same probabilities as in the uniform flow case. Figure 5.14 shows how the y velocity varies with Reynolds number at varying pressure amplitudes and cycles. Figures 5.14 (a), (c), and (e) show the y velocity for different pressure amplitudes (0.07, 0.10, and 0.12 MPa) at 26 cycles. The y velocity is largely invariant of the Reynolds number, with slight variations likely due to limited sample points. Additionally, Figures 5.14 (b), (d), and (f) show the y velocity for different cycles (13, 26, 40) at a fixed pressure amplitude of 0.10 MPa. The y velocities all have similar magnitudes and probabilities for each Reynolds number.

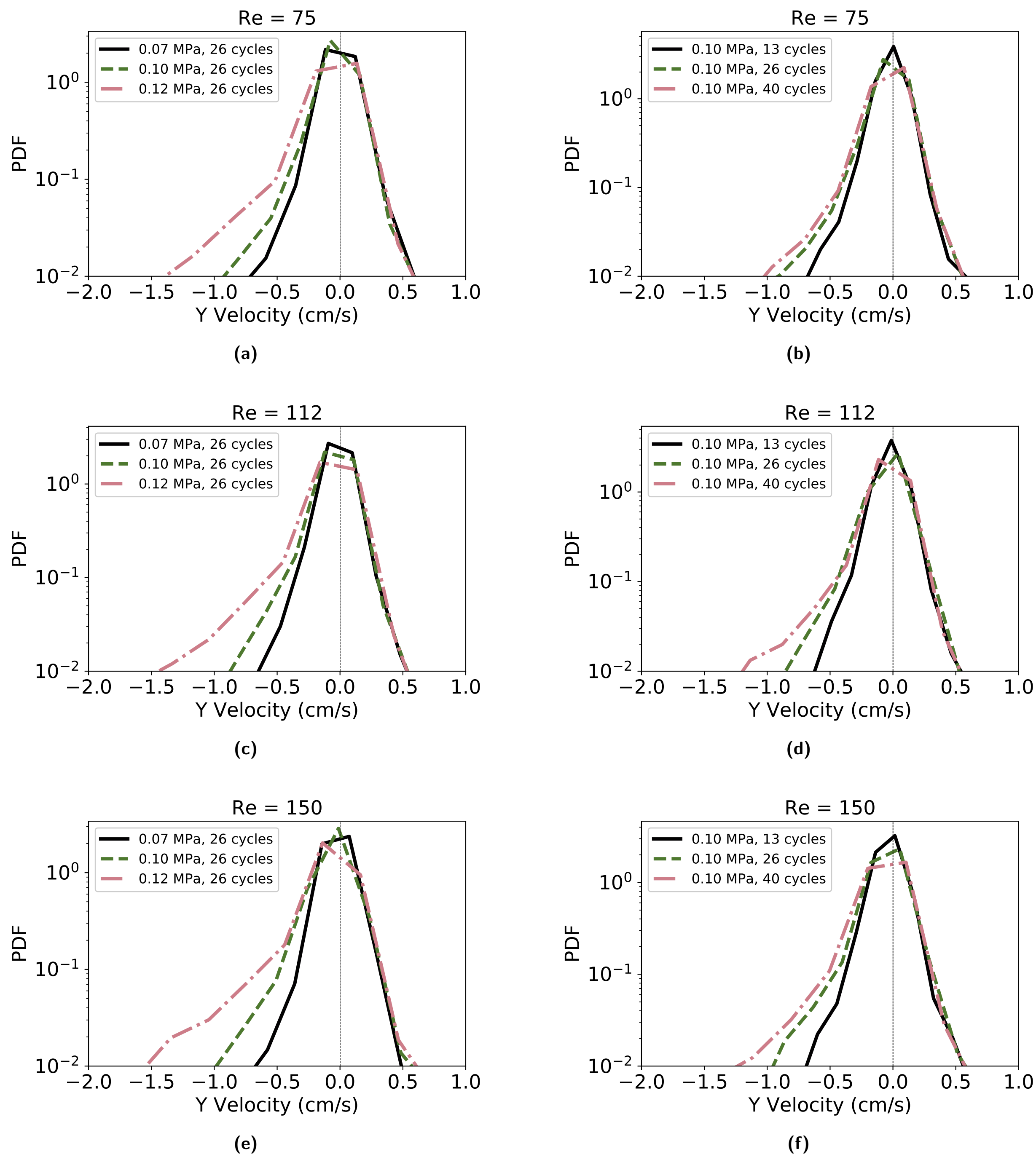

Figure 5.14: Probability density functions (PDF) of the y velocity at varying pressure amplitudes and Reynolds numbers for a fixed number of ultrasound cycles. (a) The y velocity at a Reynolds number of 75. The microbubbles see more of an effect of the ultrasound (corresponding to an increased tail length) as the pressure amplitude is increased. (a) The y displacement at a Reynolds number of 150. The microbubbles still see more of an effect of the ultrasound as the pressure amplitude is increased, although the maximum y displacement is decreased compared to the Reynolds number of 75 case.

Finally, it would be interesting to coordinate pushing events to certain phases in the velocity cycle by using phase averaging, which averages images that occur at the same phase in the cycle. The displacement of microbubbles can then be correlated to different flow velocities. Figure 5.15 shows phase averaged x velocity profiles from three different Reynolds numbers: 75, 112, and 150. Figure 5.15 (a) shows the phase averaged velocity profiles at $Re = 75$ for 5 different phases: 0, $\frac{\pi}{4}$, $\frac{\pi}{2}$, $\frac{5\pi}{4}$, and $\frac{3\pi}{2}$. The x velocity is at its mean value at 0, its minimum value at $\frac{3\pi}{2}$, and it maximum at $\frac{\pi}{2}$, as expected. Figure 5.15 (b) shows the phase averaged velocity profiles for $Re = 112$ at the same phases. The same trends follow as in (a) but now the velocity profiles are closer together due to the pulse dampener. Finally, Figure 5.15 (c) shows the phase averaged velocity profiles for $Re = 150$ at the same phases. The same trends follow as in (a) and (b) but now there is little difference between the velocity profiles at different phases; the flow is almost steady.

5.2 Ultrasound Imaging Conclusions

This chapter shows experimental evidence of how the Bjerknes force varies with pressure amplitude, number of cycles (duty factor), and Reynolds number for three flow conditions: quiescent flow, steady flow, and pulsatile flow.

The Bjerknes force is proven to become stronger at both higher number of cycles and higher pressure amplitudes in the quiescent flow experiments. By studying the void created inside the silicone test section, increases in pressure amplitude are observed to have a larger effect than increases in the number of cycles (duty factor). This agrees with the theoretical expression for the Bjerknes force reported by [45], suggesting that the force grows linearly with cycles and quadratically with pressure amplitude.

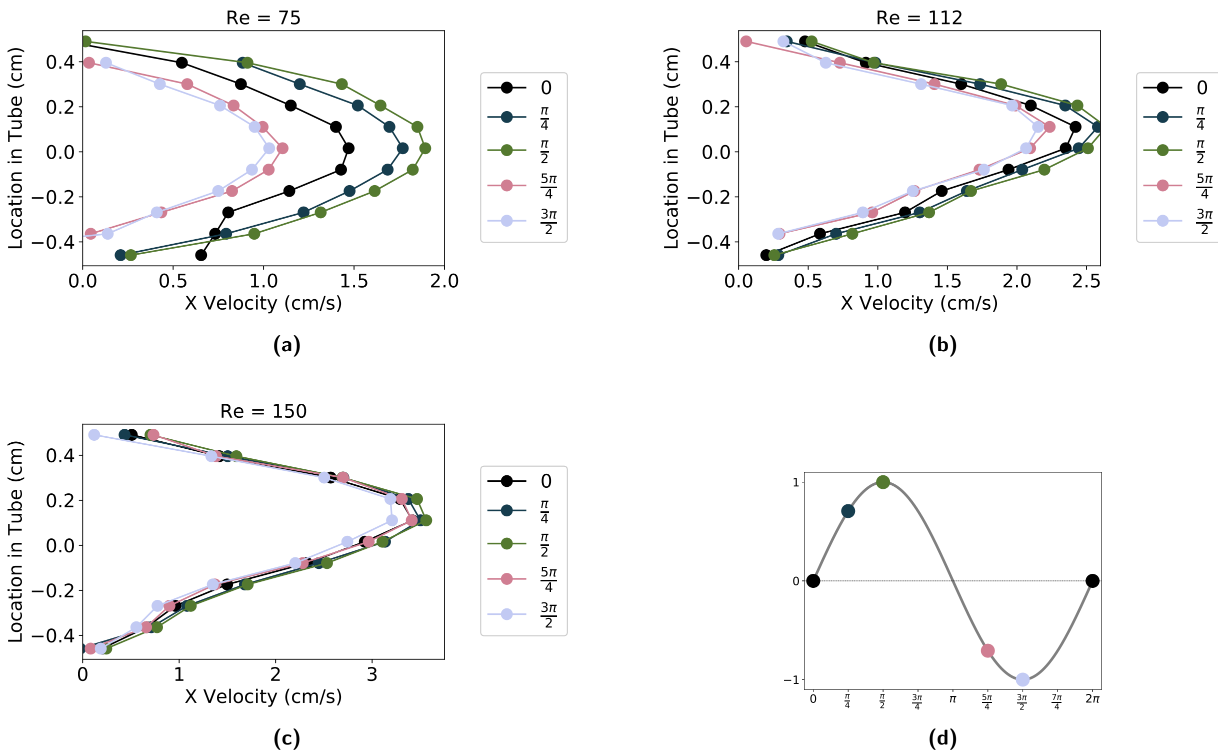

Figure 5.15: The phase averaged x velocity profile across the silicone tube. (a) The phase averaged velocity profiles at $Re = 75$ for 5 different phases: 0, $\frac{\pi}{4}$, $\frac{\pi}{2}$, $\frac{5\pi}{4}$, and $\frac{3\pi}{2}$. (b) The phase averaged velocity profiles at $Re = 112$ at the same phases as (a). (c) The phase averaged velocity profiles at $Re = 150$ at the same phases as (a) and (b). (d) Schematic showing the phases of the cardiac cycle to which the velocity measurements correspond.

The effect of pressure amplitude and number of cycles was then studied under steady flow at two different Reynolds numbers. Microbubble displacement in the direction of ultrasound propagation depends strongly on pressure amplitude, and more weakly on the number of cycles, consistent with the theory and experimental results in the quiescent fluid. In these experiments, the y velocity, which is assumed to be directly proportional to the Bjerknes force, is shown to not depend on the flow Reynolds number in the physiological range studied. This suggests that, for pushing applications, the most important parameter in this problem is the residence time of the microbubbles in the ultrasound beam. If used clinically, a wider transducer beam should be used to increase the residence time of the microbubbles by either using a larger transducer or moving the transducer further away from the pushing area to create a wider beam width.

Finally, pulsatility was studied and how it affects the displacement and velocity of microbubbles at three separate Reynolds numbers was experimentally observed. The displacement of the microbubbles varies throughout the cardiac cycle, due to the pulsatile nature of the flow. Microbubbles are displaced more in the direction of the ultrasound propagation when the flow is decelerating and close to its minimum value. The y velocities are shown to have negligible variations due to the pulsatility, when compared to the y velocities measured in the steady flow experiments. This confirms that, under the conditions explored in this study (low $Re < 200$ and high $Wo > 10$), the flow around the bubbles does not influence the Bjerknes force, which is only a function of the ultrasound beam properties, and the most important parameter in the displacement of microbubbles towards the vascular wall for drug delivery is the residence time of the microbubbles in the beam.

In addition to these findings, a new method to perform PTV in clinical ultrasound images is also introduced. PTV on microbubble images with clinical ultrasound is not found in the open literature. This is a very promising method to study microbubbles, especially with the use of research ultrasound systems with much higher frame rates and resolutions. With this methodology, hundreds to thousands of microbubbles could be tracked throughout ultrasound image sequences, to gain a greater understanding of both *in vitro* and *in vivo* microbbubles under ultrasound excitation. This novel methodology is also translatable to clinical applications where it can quickly determine flow rates and velocity profiles in the vasculature with only minimal microbubble concentrations. For example, the methodology could be used to explore the flow around plaque in a blood vessel; changes from normal flow patterns could help identify vulnerable plaques.

Chapter 6

RESULTS FROM THE OPTICAL IMAGING EXPERIMENTS

Chapter 5 discussed the dynamics of microbubbles under ultrasound excitation imaged with a clinical ultrasound imaging scanner to visualize the bubbles in the experimental setup. However, due to the low spatial and temporal resolution of clinical ultrasound systems, it was not possible to track microbubbles at higher physiological Reynolds numbers. Therefore, these studies were extended by developing an optical experimental setup. This setup allowed the use of higher concentrations of microbubbles and much faster flow rates (Reynolds numbers). Additionally, the higher acquisition rates and resolution of optical imaging allow for measurements of microbubble accelerations extracted from the multi-frame particle trajectories. This chapter focuses on how varying the pressure amplitude and pulse repetition frequency (PRF) of the transducer affects microbubble dynamics, keeping the Reynolds number constant at a high, physiologically relevant value. The dynamics of hundreds of microbubbles under ultrasound excitation has not been previously studied experimentally at a higher physiological Reynolds number using Lagrangian particle tracking, with sufficient statistics to obtain converged values of the velocity, acceleration, and force. The Lagrangian tracking used in this chapter, developed as part of this thesis, is an extremely powerful tool because it allows thousands of microbubble trajectories to be analyzed over an entire video sequence, greatly expanding current knowledge of microbubble response to ultrasound.

This chapter first gives a brief synopsis of how Lagrangian tracking is performed in the optical images. Then, the chapter revisits how the Bjerknes force varies with pressure amplitude and number of cycles in this experimental configuration. Finally, it concludes with suggestions for future studies, including utilizing the silicone phantoms developed in Chapter 3.

6.1 Bjerknes Force on Microbubbles

This chapter uses optical imaging to look at the behavior of microbubbles in steady flow at a constant value of the Reynolds number. The experimental setup was described in detail in Section 3.3.2. A reservoir system is used to create a gravity-driven steady flow. Between experiments, the height of the inlet water reservoir is replenished to provide a repeatable flow rate between experiments. Once the flow is initiated for each test, the ultrasound transducer is turned on and the camera is then triggered to start an acquisition. Each recording lasts for approximately 1 second and captures thousands of microbubbles moving through the imaging plane. During each recording, the change in the height of the inlet reservoir is observed to be negligible and, thus, the flow velocity does not change appreciably in the image acquisition area. Once a video is captured, it is post-processed using Fiji/ImageJ to find the centroid locations of the microbubbles throughout the video. These locations are then linked using the particle tracking velocimetry (PTV) algorithm introduced in Chapter 4. Figure 6.1 shows the initialization of the tracking for the optical images. The search region dimensions used in the PTV code were adjusted based on the maximum microbubble displacement between frames.

Figure 6.2 shows a sample of trajectories that were obtained from a video with this optical setup. The microbubbles at the top and bottom of the tube are moving more slowly as shown by the small spacing between the crosses in each trajectory. At the center of the tube, the microbubbles are moving fastest, as shown by the increased spacing between the crosses in these trajectories. Unlike in the ultrasound images, we are able to track hundreds of microbubbles per frame at subpixel resolution, which allows us to determine the micrometer displacements caused by the incoming ultrasound pressure field. The ultrasound transducer is positioned above the tube and pushes bubbles downwards in these images. This is opposite to the orientation in the ultrasound images described in Chapter 5; however, the movement of microbubbles away from the transducer is still considered as the negative y direction. Looking closely at the top of the image, one can see the top-most microbubbles moving slightly downwards pushed by the Bjerknes force caused by the ultrasound beam propagation downwards.

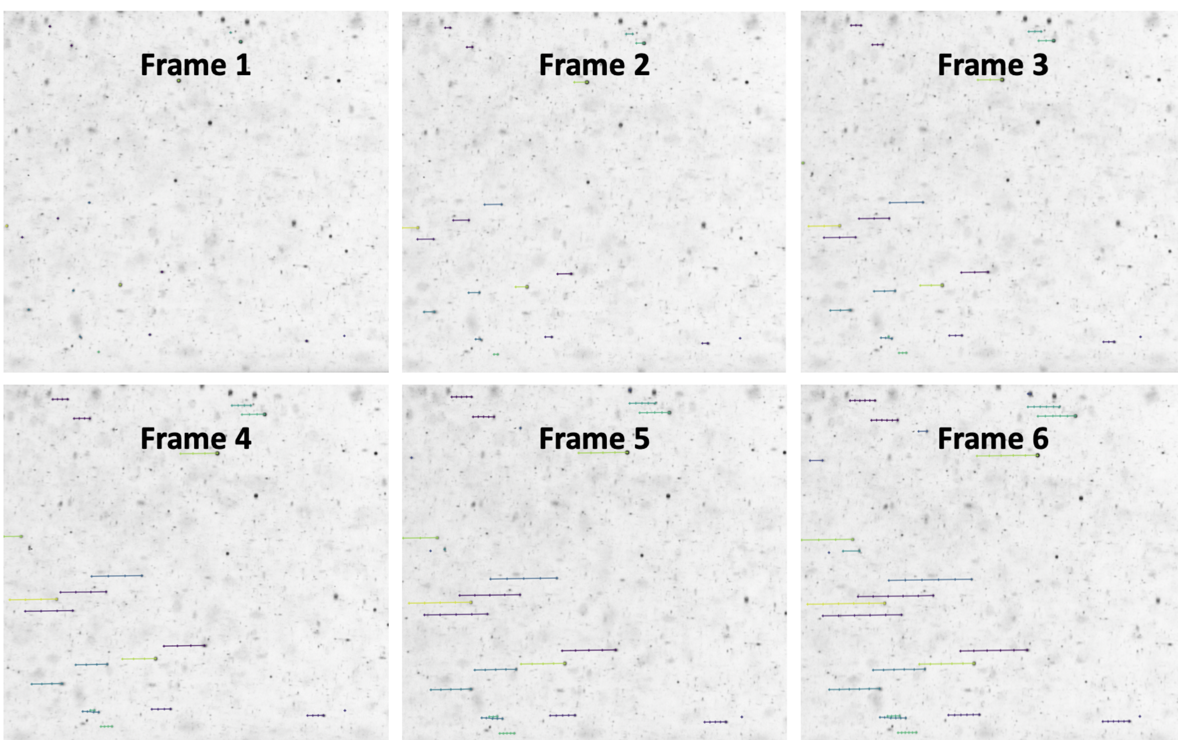

Figure 6.1: Evolution of PTV algorithm in optical images, showing a sub-sample of trajectories being built. The trajectories are started in Frame 1 and are then built up over the continuing frames.

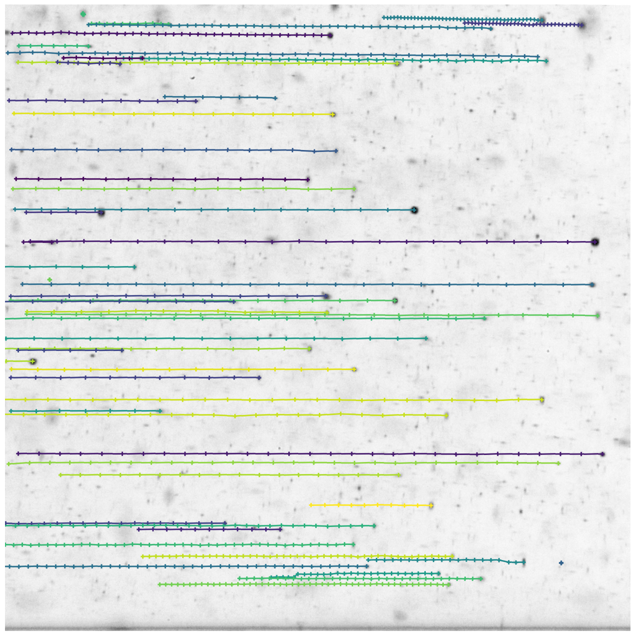

Figure 6.2: Microbubble trajectories sample obtained using PTV on the optical videos. Some microbubbles are displaced very slightly downwards at the top of the image due to the Bjerknes force.

Before examining the dynamics of microbubbles under ultrasound, experimental data was collected first without any external ultrasound forcing. This was done to validate both the tracking performance and observe any hydrodynamic forces present on the microbubbles without the presence of ultrasound. Figure 6.3 (a) shows the x velocity profile in the test section. Since the flow is steady, the data is temporally averaged and then binned along the radius of the vessel. As expected, a Poiseuille profile is obtained with good agreement between the experimental results and the Poiseuille equation:

$$v(r) = 2V\left(1 - \frac{r}{R}^{2}\right) \tag{6.1}$$

where V is the average fluid velocity in the vessel and R is the radius of the vessel. For completeness, the shear rate is also shown in Figure 6.3 (b). The shear-induced lift force is dependent on the shear rate. Finally, the y velocity profile is shown across the tube diameter in Figure 6.3 (c). The microbubbles at the top of the tube are moving downwards towards the center of the vessel. Conversely, the microbubbles at the bottom of the vessel are moving upwards towards the center. This suggests that even without the presence of ultrasound there is a natural migration of bubbles towards the centerline due to shear-induced lift force.

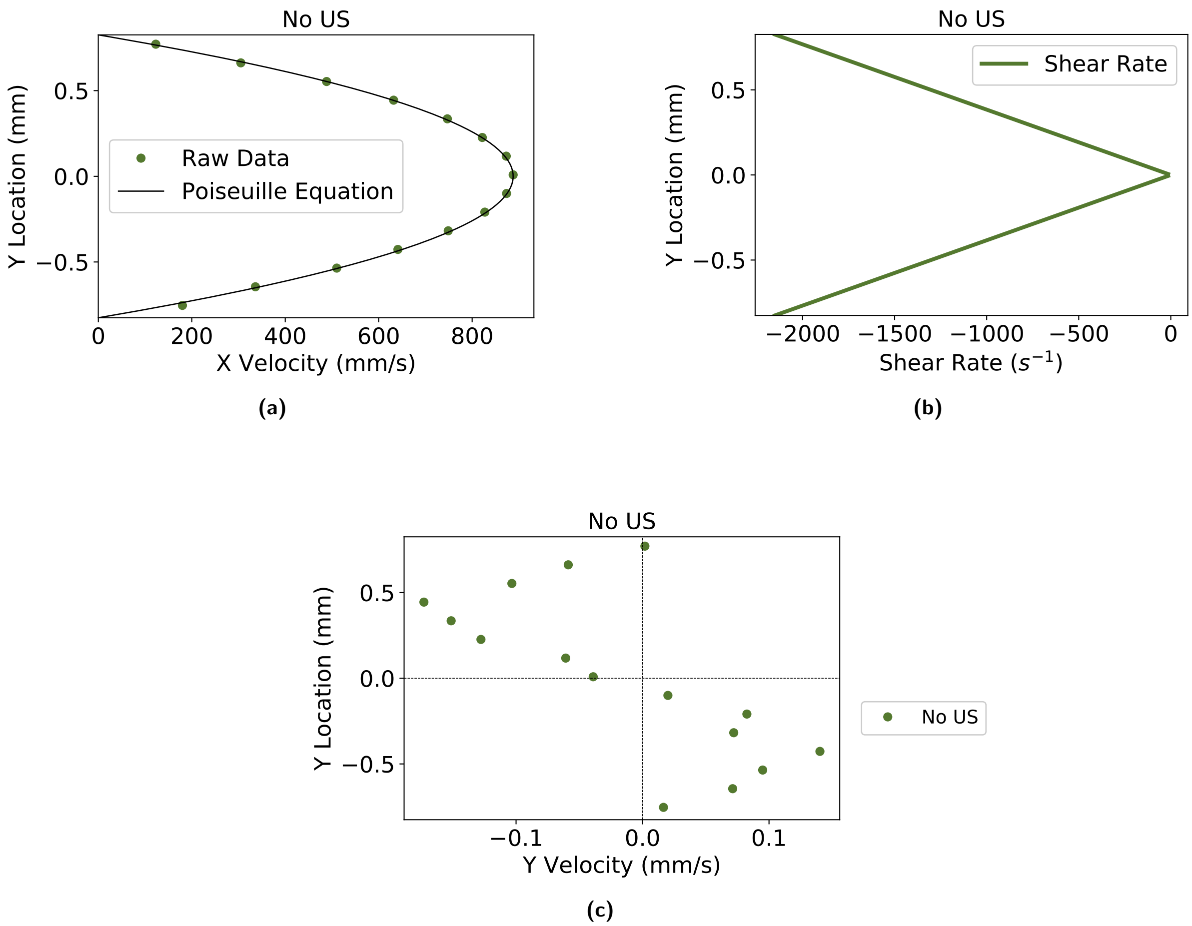

Figure 6.3: Characterization of the flow in the PTFE tubing in the absence of ultrasound forcing. (a) The x velocity profile obtained from PTV with the Poiseuille prediction overlaid. (b) The shear rate as a function of position in the vessel. (c) The y velocity profile across the tube from $-R$ (the vessel radius) to R.

Next, how the Bjerknes force acting on microbubbles varies under different ultrasound conditions is analyzed. Experiments were conducted at a single Reynolds numbers and a range of ultrasound parameters. Table 6.1 summarizes the experimental conditions for the steady flow experiments. The Reynolds number is held constant at 700 in all of the experiments. The pressure amplitude P_A is varied between 0.05 and 0.15 MPa (similar to the pressure range used in the ultrasound imaging experiments). Finally, the PRF was varied between 0 kHz and 10 kHz, resulting in duty cycles between 0 and 5%. These duty cycles were chosen to avoid bubble destruction in the vessel through cavitation and thermal heating of the transducer.

Re $Re = \frac{\rho v D}{\mu}$	P_A (MPa)	PRF (kHz) (Duty Cycle)
700	0, 0.05, 0.12, 0.15	0, 1, 5, 10 (0%, 1%, 2.5%, 5%)

Table 6.1: Parameters explored in the uniform flow experiments (optical imaging)

Figure 6.4 explores how changing the PRF affects the Bjerknes force acting on the microbubbles. Figure 6.4 (a) shows the displacement of the microbubbles at different radial locations within the test section. The microbubbles are displaced downwards near the top of vessel. As the PRF is increased, the microbubbles are displaced downwards more, as expected from the theoretical dependency of the Bjerknes force with the duration of the acoustic excitation. This also agrees well with experimental observations where there was only noticeable displacement near the top vessel wall. Figure 6.4 (b) shows the y velocity of the microbubbles across the vessel. The microbubbles are all being moved downwards at all radial locations in the vessel when the ultrasound is active. The microbubbles at the top wall of the vessel are the most affected by the ultrasound, consistent with the attenuation of the ultrasound with the working fluid, the bubbles, and the test section walls. For all PRFs, the microbubbles reach a maximum negative velocity at around 0.5 mm/s, slightly below the upper vessel wall. Below this location, the velocity starts to increase towards the center of the tube (which corresponds to a reduction of the absolute value of the velocity magnitude, since it is negative). The hypothesis is that this increase in velocity (the velocity tending towards zero) is caused by attenuation from the microbubbles in the tube. The rate of attenuation is clearly different depending on the PRF. Changes in the microbubble downward velocity are hypothesized to be due to the duration of the ultrasound exposure to which the microbubbles are subjected. Since the microbubbles have a fixed residence time in the ultrasound beam (because the flow is steady), the ultrasound affects the microbubbles more when the PRF is higher: each microbubble experiences a larger number of ultrasound pulses while it traverses the ultrasound beam. Figure 6.4 (c) shows the y acceleration across the vessel. The microbubbles accelerate downwards at the highest rate near the top of the vessel when ultrasound is present. Additionally, the acceleration is stronger at higher PRFs. Finally, Figure 6.4 (d) shows the ratio of the y velocity to the x velocity. This is done to more easily compare the effects of PRF on microbubbles displacement, since the x velocities varied slightly between tests (less than 5% difference in peak velocity).

Figures 6.5 (at a fixed PRF of 1 kHz) and 6.6 (at a fixed PRF of 10 kHz) explore how varying the pressure amplitude between 0 and 0.15 MPa affects the Bjerknes force acting on the microbubbles. Figures 6.5 (a) and 6.6 (a) show the y displacement of the microbubbles. In the 1 kHz PRF experiments, there is minimal displacement of the microubbles; at the highest pressure amplitude of 0.15 MPa, the microbubbles are only pushed down 5 μm. At the higher PRF (10 kHz), the displacement is larger, especially at the top wall of the vessel. Figures 6.5 (b) and 6.6 (b) show the y velocities of the microbubbles. Since the magnitude of the ultrasound force is smaller at 1 kHz, the ultrasound only affects the microbubbles in the top of the vessel. At these small pressures, the Bjerknes force at the bottom of the vessel is not strong enough to overcome the shear-induced lift.

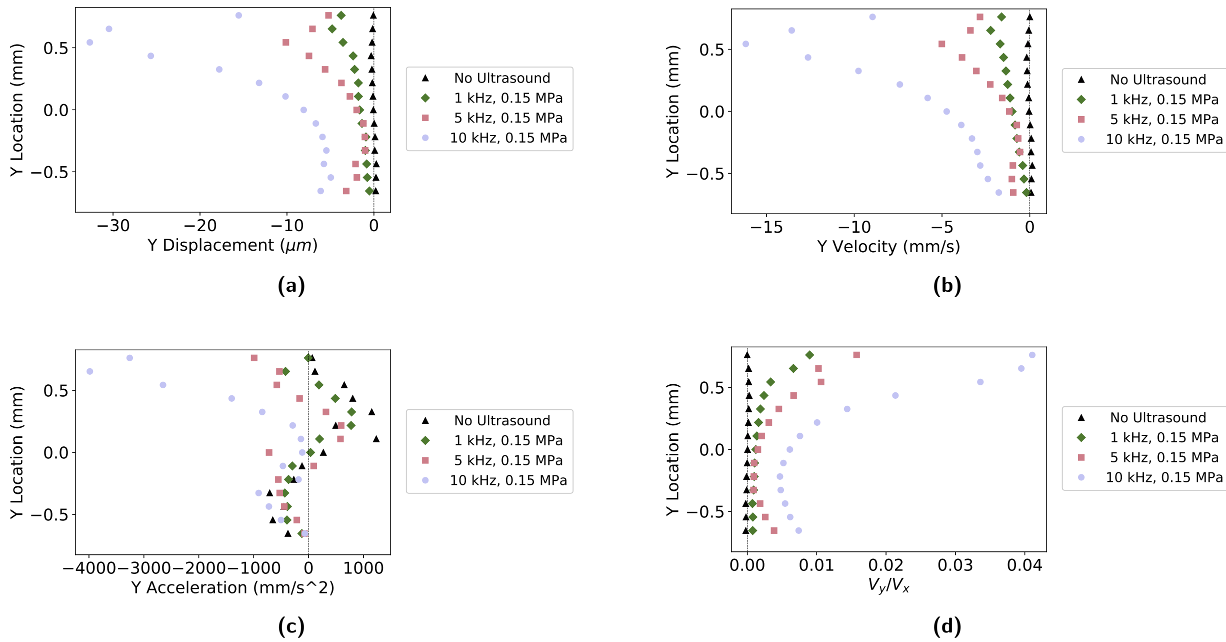

Figure 6.4: The effect of changing the pulse repetition frequency (PRF) of the incoming ultrasound pressure field on (a) the displacement of microbubbles in the y direction, (b) the velocity of the microbubbles in the y direction, (c) the acceleration of microbubbles in the y direction, and (d) the ratio of the y velocity to the x velocity. The PRF was varied from 0 to 10 kHz.

At 10 kHz, similar trends are observed, but the microbubbles in the bottom part of the vessel no longer move towards the center since the ultrasound force is strong enough to overcome the shear-induced lift. This was also evident visually in the experiments because there was noticeable deposition of microbubbles on the bottom wall of the tube. Figures 6.5 (c) and 6.6 (c) show the acceleration of the microbubbles. For the 1 kHz PRF experiments, the microbubbles are decelerating (negative velocity but positive acceleration) as they move from the upper part of the tube towards the center. In the bottom part, the Bjerknes force does not overcome the shear-induced lift and the bubbles are moving toward the center of the vessel while decelerating, except at the highest pressure (0.15 MPa) where the ultrasound-induced downward motion persists, with negative velocity and acceleration. Similar trends are observed for the 10 kHz PRF experiments. However, for these experiments, the microbubbles move towards the bottom of the vessel (negative velocity and negative acceleration) at all pressure amplitudes since the Bjerknes force is always strong enough to overcome the shear-induced lift force. Finally, Figures 6.5 (d) and 6.6 (d) show the magnitude of the ratio of y velocity to the x velocity. For both the 1 kHz and 10 kHz experiments, the y component of the velocity grows faster with respect to the local advective velocity (x-component), as the pressure increases from 0 MPa to 0.15 MPa.

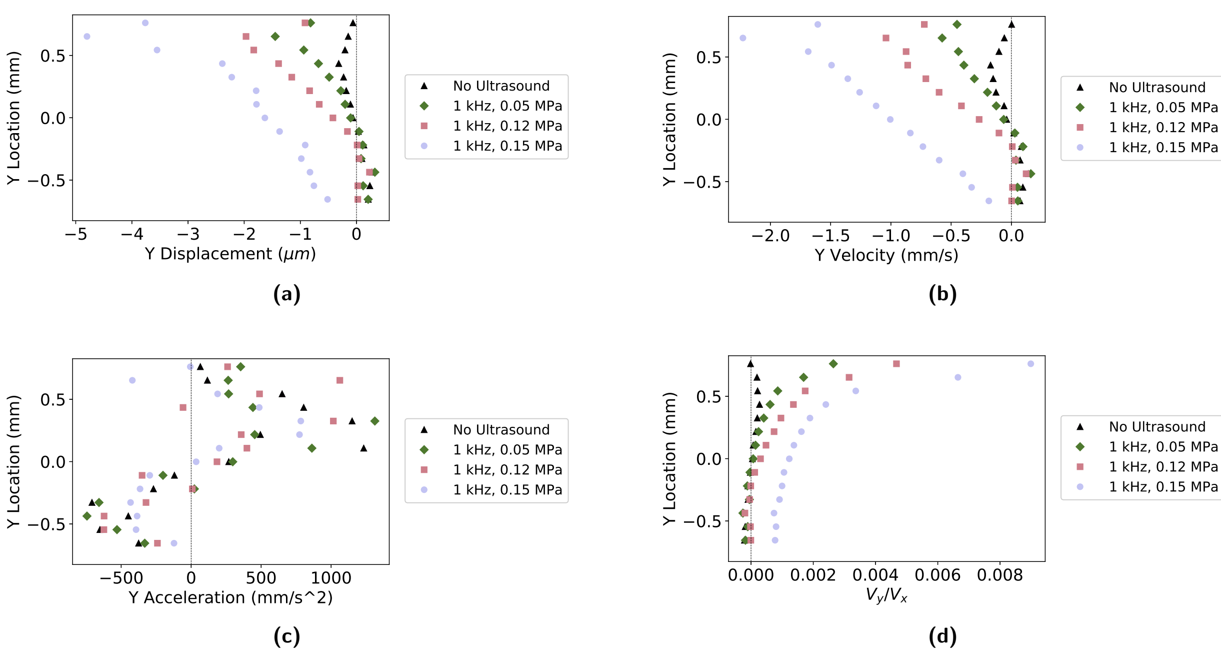

Figure 6.5: The effect of changing the pressure amplitude of the incoming ultrasound pressure field at a fixed PRF of 1 kHz on (a) the displacement of microbubbles in the y direction, (b) the velocity of the microbubbles in the y direction, (c) the acceleration of microbubbles in the y direction, and (d) the ratio of the y velocity to the x velocity. The pressure was varied from 0 MPa to 0.15 MPa.

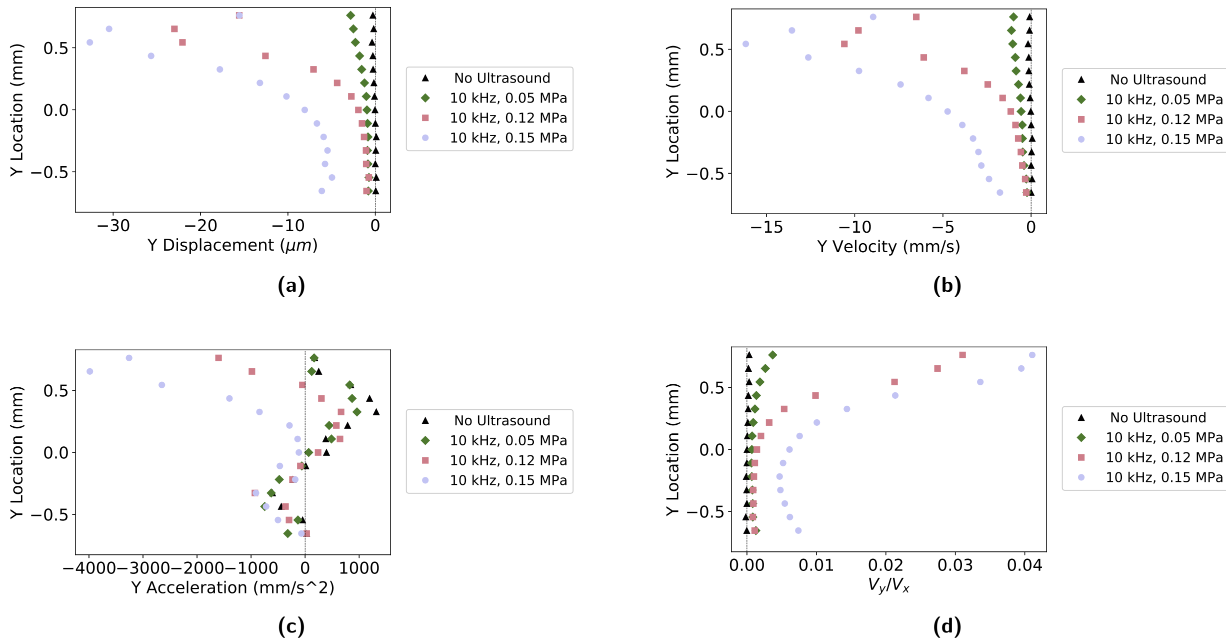

Figure 6.6: The effect of changing the pressure amplitude of the incoming ultrasound pressure field at a fixed PRF of 10 kHz on (a) the displacement of microbubbles in the y direction, (b) the velocity of the microbubbles in the y direction, (c) the acceleration of microbubbles in the y direction, and (d) the ratio of the y velocity to the x velocity. The pressure was varied from 0 MPa to 0.15 MPa.

6.2 Optical Imaging Conclusions

This chapter shows experimental evidence that, and quantifies how, the Bjerknes force varies with pressure amplitude and PRF for steady flow at a physiologically relevant Reynolds number of 700.

The Bjerknes force is shown to become stronger at both increased PRF and higher pressure amplitude in the experiments. Microbubble displacement in the direction of ultrasound propagation depends strongly on pressure amplitude, and more weakly on the PRF, consistent with the theory and experimental results obtained in Chapter 5. In these experiments, the interaction between the Bjerknes force and the shear-induced lift force is analyzed, since at very low pressures and low duty cycles the two forces are comparable and compete to drive the velocity of the microbubbles across the streamlines. The higher concentration of microbubbles used in these optical experiments produces non-negligible attenuation of the ultrasound excitation, highlighting differences between the behaviour of the bubbles near the top (highest ultrasound intensity closest to the transducer) and the bottom (weakest ultrasound excitation farthest from the transducer). At the weakest ultrasound pressure (0.05 MPa), the ultrasound only influences the microbubbles near the top of the vessel, closest to the transducer; the microbubbles near the bottom of the vessel responded similarly to the control experiment microbubbles where the bubbles were not insonated by ultrasound. However, as the excitation pressure increased, the Bjerknes force was strong enough to overcome the shear-induced lift and continue to push the bubbles downwards, towards the bottom vessel wall (opposite the transducer).

Future experiments could be conducted at higher pressure amplitudes to increase the magnitude of the Bjerknes force. In the current experimental setup, only the microbubbles at the top of the vessel were significantly displaced. For pushing applications, it would be necessary to increase the uniformity of the Bjerknes force across the test section, in addition to using higher pressures or duty cycles to increase the downward displacement of the microbubbles. The concentration of microbubbles is also very important in pushing applications since larger concentrations of microbubbles tend to shield the microbubbles below them, by attenuating the pressure field [38, 43]. It would be extremely interesting to repeat these experiments at different microbubble concentrations to explore how the Bjerknes force is related to microbubble concentration. Similarly, it would be interesting to use these analysis techniques in a patient-specific flow geometry to explore pushing in a realistic vessel. The work performed in this thesis to develop patient-specific silicone phantoms could potentially be used for this application.

Chapter 7

CONCLUSIONS AND FUTURE WORK

This chapter summarizes the conclusions and contributions made throughout this dissertation. Each section summarizes the important scientific contributions obtained in each chapter (beginning with Chapter 3). The chapter concludes by offering some potential aims for future research related to this work and summarizes the main findings of this research.

7.0.1 Experimental Development

In Chapter 3, the microbubbles and ultrasound transducer used for the experiments were introduced. Commerical Sonazoid microbubbles were used for the ultrasound imaging experiments, and in-house microbubbles were used for the optical imaging experiments. These microbubbles are both lipid-shelled with perfluorobutane gas cores; however, they may have slightly different shell properties, causing them to respond differently to the incoming ultrasound pressure field. Despite this, the trends presented from both the ultrasound-imaging results and the optical-imaging results remain fairly consistent. The Bjerknes force increases strongly with pressure amplitude and weakly with duty cycle. This is consistent with the theoretical framework for small amplitude volume oscillations that predicts quadratic dependency of Bjerknes force with pressure amplitude and linear dependency with duty cycle.

This chapter also introduced the development of two separate experimental setups: an ultrasound imaging setup and an optical imaging setup. There were pros and cons to both experimental setups. The ultrasound experimental setup allowed imaging of the microbubbles in non-transparent silicone tubing that was 'transparent' to ultrasound ($< 5\%$ losses through the tube wall). It also enabled the use of a clinical ultrasound system which is an additional factor to make this research more clinically relevant. Despite these advantages, the acquisition rates of the ultrasound system are in the Hertz to hundreds of Hertz range, which makes it impossible to track microbubbles at much faster flow rates (corresponding to higher Reynolds numbers). Additionally, the resolution of a clinical ultrasound system is lower than an optical imaging system, which makes it nearly impossible to discern if individual microbubbles or clusters of microbubbles are being tracked. Therefore, to complement these studies, an optical imaging experimental setup was developed to examine the Bjerknes force acting on the microbubbles. This system had a much higher acquisition rate (Hertz to kiloHertz) and higher resolution (on the micrometer scale). This allowed individual microbubbles to be tracked with high spatial and temporal resolution. However, while this setup does offer advantages, it was difficult to find materials that would be both ultrasound transparent and optically transparent. Numerous different types of tubing and gel materials (such as poly(vinyl alcohol) (PVA), commonly used as an ultrasound phantom) were explored in the development of the optical experimental setup. In the end, it was decided to use PTFE tubing for the experimental setup because it was optically transparent and allowed sufficient ultrasound transmission. In the future, it would be interesting to redo these experiments with better optically and acoustically transparent phantom materials.

7.0.2 Segmenting Microbubbles from Images and Particle Tracking Velocimetry (PTV)

Chapter 4 explores the post-processing performed on the videos obtained from both the ultrasound imaging and the optical imaging experimental setup. The microbubbles are segmented from the ultrasound and optical images differently. The centroid detection, however, performs well in both cases, with only a slightly larger error in the segmentation done in the ultrasound images, due to the low image resolution and contrast. Subsequently, the chapter discusses the new method using a modified initialization introduced to the four-frame best estimate PTV algorithm. With only a simple change in initialization, the tracking performance improves significantly compared to a nearest neighbor initialization method, and this is shown by evaluating tracking performance on a homogenous isotropic turbulence dataset and a turbulent channel flow dataset. This improvement to the algorithm increases performance in conditions where tracking is typically very difficult (such as large particle displacements between frames), which is very helpful in the evaluation of microbubble trajectories in both the ultrasound and optical experiments. The chapter also introduces a new metric for evaluating tracking performance, ξ'. This metric could be useful for experimentalists when they are deciding particle seedings or adjusting the displacement of particles between image frames.

7.0.3 Ultrasound Experiments

Chapter 5 explores how the Bjerknes force acting on the microbubbles varies in different flow and ultrasound conditions. Experiments were conducted in a quiescent fluid, a steady flow, and a pulsatile flow. In each of these flow conditions, ultrasound pressure amplitudes and number of cycles (duty cycle) were varied to explore how these ultrasound properties affect the microbubble response. The quiescent fluid experiments showed that more microbubbles are displaced (by observing a larger void in the tube) as the pressure amplitude is increased and as the number of cycles is increased. Bubble destruction is observed starting at amplitudes around 0.2 MPa. These experiments informed the next experiments in both this chapter and the optical imaging chapter, putting an upper bound on the pressure amplitude used to excite the bubbles, at around 0.17 MPa for the in-house microbubbles. The same limit was also used for the Sonazoid microbubbles.

Experiments were then conducted at two Reynolds numbers ($Re = 75$, 150) in a steady flow. In these experiments, the pressure amplitude was varied between 0.07 and 0.14 MPa and the number of cycles was varied between 13 and 53 cycles, giving duty cycles between 10% and 40%. Similar trends were observed at both Reynolds numbers. The Bjerknes force acting on the microbubbles (proportional to the y velocity of the microbubbles) increases with increasing pressure and number of cycles. The force is found to not depend on the Reynolds number, however, the net displacement of the microbubbles is a function of the Reynolds number since the bubble displacement is related to the microbubble residence time in the ultrasound excitation beam.

Finally, experiments were conducted to study microbubble response with pulsatility at three different Reynolds numbers: 75, 112, and 150. In these experiments, the pressure amplitude was varied between 0.07 and 0.12 MPa and the number of cycles was varied between 13 and 40 (10% to 30% duty cycle). The trends remain consistent with those described from the steady flow experiments, with an increase in Bjerknes force magnitude with pressure amplitude and number of cycles and no appreciable change in force with changing Reynolds number. However, the microbubbles are displaced further in these experiments. This occurs because the microbubbles, especially near the vessel walls, have a longer residence time in the ultrasound beam when the flow is decelerating and reversing, allowing the microbubbles to experience the Bjerknes force for a larger period of time. This is due to the Womerseley velocity profile carrying the microbubbles along different trajectories than the Poiseuille flow profile, even when the bulk flow rates are matched.

These experiments also introduced the multiframe PTV technique to clinical ultrasound imaging. This new technique pioneered in this thesis has potential future clinical applications. For example, PTV could be used to quickly determine flow rates and velocity profiles in the vasculature with only minimal microbubble concentrations. Another area of interest would be having the ability to further study cavitation breakup at higher ultrasound pressure amplitudes.

7.0.4 Optical Experiments

Finally, Chapter 6 examines the dynamics of microbubbles under ultrasound excitation using optical imaging at a higher physiologically relevant Reynolds number ($Re = 700$). In these experiments, the pressure amplitude was varied between 0 and 0.15 MPa and the PRF was varied between 0 and 10, resulting in duty cycles between 0% and 5%. Due to the increased imaging resolution, micrometer-scale microbubble displacements, due to the incoming ultrasound waveform, were observable . This provides an improved understanding of the complicated and interesting microbubble dynamics. Without the presence of ultrasound, it is observed that there is a shear-induced lift force acting on the microbubbles that pushes them towards the center of the vessel. At the lowest duty cycle, this lift force dominates the trajectories of the microbubbles near the bottom of the vessel, even at the highest ultrasound pressures. This suggests that the Bjerknes force due to ultrasound is very weak in the bottom part of the vessel. However, there is still noticeable displacement of microbubbles from the top of the vessel downwards towards the center of the tube, even at this low PRF. This decrease in displacement across the vessel, from the part closest to the transducer to the one farthest from it, is likely due to attenuation of the propagating ultrasound by the microbubbles. At a higher PRF of 10 kHz, the lift force has minimal effect compared to Bjerknes force at pressures above 0.05 MPa. At 0.15 MPa, the Bjerknes force dominates and displaces microbubbles downwards throughout the entire cross section of the vessel. The microbubbles are still, however, displaced more near the top of the vessel tube than near the bottom, due to non-negligible attenuation.

Additionally, the trends shown in this chapter agree with the trends presented in Chapter 5. The Bjerknes force increases strongly with increasing pressure amplitude (quadratically) and weakly with PRF/duty cycle (linearly).

7.0.5 Future Studies

It would be interesting to extend both the ultrasound imaging and optical imaging experiments in the future to explore an even larger range of ultrasound parameters to further fine tune the dependence of the Bjerknes force on these ultrasound parameters. For example, it would be interesting to consider if the linear dependence of the Bjerknes force on PRF holds even up to very high PRFs (duty cycles) since previous research has suggested that secondary Bjerknes forces become important in this regime ([51] and references within). While conducting the optical experiments, secondary Bjerknes forces were only noticed when the Reynolds number was very low (in between experiments when the flow was stopped), suggesting a large dependence on bubble residence time for these secondary forces.

Another important parameter that could be further evaluated experimentally is the magnitude of the Bjerknes force as a function of the concentration of microbubbles. This is an extremely difficult problem to address because there is variability in sizes and concentrations between different microbubble batches. In addition, once activated, there is a decrease in microbubble concentration over time. An estimate of microbubble concentration can be obtained from the optical images, since individual bubbles were resolved, but these measurements could potentially be difficult to correlate to microbubble concentration since the imaging only characterizes the microbubble size and concentration at a small region of the test section. A wide range of images spanning the entire test section in length, width and depth would need to be automatized to get accurate results. Similarly, a research ultrasound system imaging at a much higher frequency could also be used for this study since it would also be capable of resolving individual microbubbles.

Finally, it would be interesting to perform pulsatile flow studies with the optical-imaging setup. In this thesis, the optical experimental setup is susceptible to leaking at very drastic changes in pressure, so it would have to be modified for pulsatile flow before conducting the proposed study. However, the silicone models that were developed in this thesis could be extremely useful for this application. It would be interesting to explore different pulse cycles for pushing in pulsatile flow. For example, it may be possible to maximize the Bjerknes force effect by insonating the microbubbles at a high duty cycle only during a certain phase in the cardiac cycle (diastole), producing a much higher displacement than continuously running the transducer at a lower duty cycle, while maintaining the same net heating.

7.0.6 Implications of This Work

To conclude, **this thesis developed a novel particle tracking technique and two experimental setups**, and answered the following three questions:

- How do the dynamics of microbubbles under ultrasound excitation change when there is inhomogeneous (sheared) and pulsatile flow around them (in millimeter- or larger scale vessels)?

- How to properly model the interaction between the microbubbles and the flow around them, specifically the coupling of volume oscillations with hydrodynamic lift and drag?
- Do the ultrasound-induced forces have the ability to modify microbubble trajectories, overcoming the dominance of drag and altering lift, to transport microbubbles towards the vessel walls or a specific branch in a bifurcation?

We showed that the Bjerknes force acting on the microbubbles is not dependent on the Reynolds number, obtaining similar y velocities (an estimator of the Bjerknes force) in both the ultrasound and optical imaging experiments. Rather, the net y displacement of the microbubbles, which is desired for pushing applications, is largely dependent on the flow velocity and the corresponding residence time of the microbubbles in the ultrasound beam. In the ultrasound experiments, the ultrasound is shown to be able to displace some microbubbles across the entire vessel even at fairly high Reynolds numbers (on the order of 100). At even higher pressures (not shown in this dissertation), the ultrasound could push all the microbubbles in the vessel to the far tube wall. Very similar trends for the Bjerknes force were found in the pulsatile flow experiments, with an even larger increase in microbubble displacement during flow deceleration due to the increased bubble residence time.

Finally, an improved understanding of the interaction between the drag, lift, and Bjerknes forces was gained from the optical experiments. For large enough pressure amplitudes and PRFs, the Bjerknes force was shown to dominate over sheared-induced lift, and the microbubbles were easily displaced in the direction of propagation of the ultrasound excitation beam, against the natural tendency of the lift to push the bubbles away from the walls of the vessel.

BIBLIOGRAPHY

[1] Open source particle tracking velocimetry - openptv. https://github.com/OpenPTV.

[2] A. Aliseda and J. Lasheras. Effect of buoyancy on the dynamics of a turbulent boundary layer laden with microbubbles. *Journal of Fluid Mechanics*, 559:307–334, 2006.

[3] A. Aliseda, A. Cartellier, F. Hainaux, and J. Lasheras. Effect of preferential concentration on the settling velocity of heavy particles in homogeneous isotropic turbulence. *Journal of Fluid Mechanics*, 468:77–105, 2002.

[4] C. R. Anderson, X. Hu, H. Zhang, J. Tlaxca, A.-E. Declèves, R. Houghtaling, K. Sharma, M. Lawrence, K. W. Ferrara, and J. J. Rychak. Ultrasound molecular imaging of tumor angiogenesis with an integrin targeted microbubble contrast agent. *Investigative Radiology*, 46:215–224, 2011.

[5] C. P. Bateson and A. Aliseda. Wind tunnel measurements of the preferential concentration of inertial droplets in homogeneous isotropic turbulence. *Experiments in Fluids*, 52:1373–1387, 2012.

[6] V. Bjerknes. *Fields of Force*. The Columbia University Press, New York, 1906.

[7] R. Bordás, C. Roloff, D. Thévenin, and R. Shaw. Experimental determination of droplet collision rates in turbulence. *New Journal of Physics*, 15:045010, 2013.

[8] N. A. Buchmann, M. C. Jermy, and C. V. Nguyen. Experimental investigation of carotid artery haemodynamics in an anatomically realistic model. *International Journal of Experimental and Computational Biomechanics*, 1(2):172–192, 2009.

[9] N. A. Buchmann, C. Atkinson, M. C. Jeremy, and J. Soria. Tomographic particle image velocimetry investigation of the flow in a modeled human carotid artery bifurcation. *Experiments in Fluids*, 50:1131–1151, 2011.

[10] R. Budwig. Refractive index matching methods for liquid flow investigations. *Experiments in Fluids*, 17(5):350–355, 1994.

[11] A. Cafarelli, A. Verbeni, A. Poliziani, P. Dario, A. Menciassi, and L. Ricotti. Tuning acoustic and mechanical properties of materials for ultrasound phantoms and smart substrates for cell cultures. *Acta Biomaterialia*, 49:368–378, 2017.

[12] P. Charoenphol, R. B. Huang, and O. Eniola-Adefeso. Potential role of size and hemodynamics in the efficacy of vascular-targeted spherical drug carriers. *Biomaterials*, 31: 1392–1402, 2010.

[13] P. Charoenphol, S. Mocherla, D. Bouis, K. Namdee, D. J. Pinsky, and O. Eniola-Adefeso. Targeting therapeutics to the vascular wall in atherosclerosis – carrier size matters. *Atherosclerosis*, 217:364–370, 2011.

[14] P. Charoenphol, P. J. Onyskiw, M. Carrasco-Teja, and O. Eniola-Adefeso. Particle-cell dynamics in human blood flow: Implications for vascular-targeted drug delivery. *Journal of Biomechanics*, 45:2822–2828, 2012.

[15] C. Cierpka, B. Lütke, and C. J. Kähler. Higher order multi-frame particle tracking velocimetry. *Experiments in Fluids*, 54:1533, 2013.

[16] M. Cisse, E. Saw, M. Gibert, E. Bodenschatz, and J. Bec. Turbulence attenuation by large neutrally buoyant particles. *Physics of Fluids*, 27:061702, 2015.

[17] I. D. Cock, E. Zagato, K. Braeckmans, Y. Luan, N. de Jong, S. C. D. Smedt, and I. Lentackera. Ultrasound and microbubble mediated drug delivery: acoustic pressure as determinant for uptake via membrane pores or endocytosis. *Journal of Controlled Release*, 197:20–28, 2015.

[18] B. C. Cole, G. G. Marcus, S. Parsa, S. Kramel, R. Ni, and G. A. Voth. Methods for measuring the orientation and rotation rate of 3d-printed particles in turbulence. *Journal of Visualized Experiments*, 112:53599, 2016. doi: 10.3791/53599.

[19] D. Cosgrove. Ultrasound contrast agents: An overview. *European Journal of Radiology*, 60(3):324 – 330, 2006.

[20] L. Crum and A. Prosperetti. Nonlinear oscillations of gas bubbles in liquids: an interpretation of some experimental results. *The Journal of the Acoustical Society of America*, 73(1):121–127, 1983.

[21] L. A. Crum. Bjerknes forces on bubbles in a stationary sound field. *The Journal of the Acoustical Society of America*, 57:1363–1370, 1975.

[22] S. Datta, C.-C. Coussios, A. Y. Ammi, T. D. Mast, G. M. de Courten-Myers, and C. K. Holland. Ultrasound-enhanced thrombolysis using definity® as a cavitation nucleation agent. *Ultrasound in Medicine and Biology*, 34(9):1421 – 1433, 2008.

[23] P. A. Dayton, J. S. Allen, and K. W. Ferrara. The magnitude of radiation force on ultrasound contrast agents. *The Journal of the Acoustical Society of America*, 112: 2183–2192, 2002.

[24] P. A. Dayton, K. E. Morgan, A. L. Klibanov, G. Brandenburger, K. R. Nightingale, and K. W. Ferrara. A preliminary evaluation of the effects of the primary and secondary radiation forces on acoustic contrast agents. *IEEE Transactions on Ultrasonics, Ferroelectrics, and Frequency Control*, 62:176–184, 2015.

[25] Z. Dou, P. J. Ireland, A. D. Bragg, Z. Liang, L. R. Collins, and H. Meng. Particle-pair relative velocity measurement in high-reynolds-number homogeneous and isotropic turbulence using 4-frame particle tracking velocimetry. *Experiments in Fluids*, 59:30, 2018.

[26] D. B. Ellegala, H. Leong-Poi, J. E. Carpenter, A. L. Klibanov, S. Kaul, M. E. Shaffrey, J. Sklenar, and J. R. Lindner. Imaging tumor angiogenesis with contrast ultrasound and microbubbles targeted to $\alpha_v\beta_3$. *Circulation*, 108(3):336–341, 2003.

[27] A. Eller. Force on a Bubble in a Standing Acoustic Wave. *Journal of Acoustical Society of America*, 43(1):170–171, 1967.

[28] J. M. Escoffre, J. Piron, A. Novell, and A. Bouakaz. Doxorubicin delivery into tumor cells with ultrasound and microbubbles. *Molecular Pharmaceutics*, 8:799–806, 2011.

[29] Z. Feng and L. Leal. Nonlinear bubble dynamics. *Annual Review of Fluid Mechanics*, 29:201–43, 1997.

[30] K. Ferrara, R. Pollard, and M. Borden. Ultrasound microbubble contrast agents: fundamentals and application to gene and drug delivery. *Annual Review of Biomedical Engineering*, 9:415–447, 2007.

[31] P. H. Geoghegan, N. A. Buchmann, C. J. T. Spence, S. Moore, and M. Jermy. Fabrication of rigid and flexible refractive-index-matched flow phantoms for flow visualisation and optical flow measurements. *Experiments in Fluids*, 2012.

[32] M. Ghobadi and Y. S. Muzychka. A review of heat transfer and pressure drop correlations for laminar flow in curved circular ducts. *Heat Transfer Engineering*, 37:815–839, 2016.

[33] J. Graham, K. Kanov, X. I. A. Yang, M. Lee, N. Malaya, C. C. Lalescu, R. Burns, G. Eyink, A. Szalay, R. D. Moser, and C. Meneveau. A web services accessible database of turbulent channel flow and its use for testing a new integral wall model for les. *Journal of Turbulence*, 17(2):181–215, 2016. doi: 10.1080/14685248.2015.1088656.

[34] S. Hernot and A. Klibanov. Microbubbles in ultrasound-triggered drug and gene delivery. *Advanced Drug Delivery Reviews*, 60(10):1153–1166, 2008.

[35] L. M. Hopkins, J. T. Kelly, A. S. Wexler, and A. K. Prasad. Particle image velocimetry measurements in complex geometries. *Experiments in Fluids*, 29:91–95, 2000.

[36] P. Huck, C. Bateson, R. Volk, A. Cartellier, M. Bourgoin, and A. Aliseda. The role of collective effects on settling velocity enhancement for inertial particles in turbulence. *Journal of Fluid Mechanics*, 846:1059–1075, 2018.

[37] *K2 Objective Options*. Infinity Optics, 2016. URL `http://www.edmundoptics.com/imaging-lenses/variable-magnification-lenses/infinity-k2-distamax-long-distance-video-microscopes/1477/`.

[38] C. Keravnou, C. Mannaris, and M. Averkiou. Accurate measurement of microbubble response to ultrasound with a diagnostic ultrasound scanner. *IEEE Transactions on Ultrasonics, Ferroelectrics, and Frequency Control*, 62:176–184, 2015.

[39] D. B. Khismatullin. Resonance frequency of microbubbles: Effect of viscosity. *The Journal of the Acoustical Society of America*, 116(3):1463, 2004.

[40] D. M. King, C. M. Moran, J. D. McNamara, A. J. Fagan, and J. E. Browne. Development of a vessel-mimicking material for use in anatomically realistic doppler flow phantoms. *Ultrasound in Medicine and Biology*, 37:813–826, 2011.

[41] A. Klibanov. Microbubble contrast agents: targeted ultrasound imaging and ultrasound-assisted drug-delivery applications. *Investigative Radiology*, 41(3):354–362, 2006.

[42] D. N. Ku. Blood flow in arteries. *Annual Review of Fluid Mechanics*, 29:399–434, 1997.

[43] M. Lampaskis and M. Averkiou. Investigation of the relationship of nonlinear backscattered ultrasound intensity with microbubble concentration at low mi. *Ultrasound in Medicine and Biology*, 36:306–312, 2010.

[44] J. M. Lawson, E. Bodenschatz, C. C. Lalescu, and M. Wilczek. Bias in particle tracking acceleration measurement. *Experiments in Fluids*, 59:172, Nov. 2018.

[45] T. Leighton. *The Acoustic Bubble*. Academic Press Inc, 1994.

[46] D. Li, Y. Zhang, Y. Sun, and W. Yan. A multi-frame particle tracking algorithm robust against input noise. *Measurement Science and Technology*, 29:105401, 2008.

[47] Y. Li, E. Perlman, M. Wan, Y. Yang, C. Meneveau, R. Burns, S. Chen, A. Szalay, and G. Eyink. A public turbulence database cluster and applications to study lagrangian evolution of velocity increments in turbulence. *Journal of Turbulence*, 9(31):1–29, 2008.

[48] C.-Y. Lin, J.-R. Li, H.-C. Tseng, M.-F. Wu, and W.-L. Lin. Enhancement of focused ultrasound with microbubbles on the treatments of anticancer nanodrug in mouse tumors. *Nanomedicine*, 8(6):900 – 907, 2012.

[49] N. Machicoane, M. López-Caballero, M. Bourgoin, A. Aliseda, and R. Volk. A multi-time-step noise reduction method for measuring velocity statistics from particle tracking velocimetry. *Measurement Science and Technology*, 28(10):107002, 2017.

[50] N. A. Malik, T. Dracos, and D. A. Papantoniou. Particle tracking velocimetry in three-dimensional flows part ii: Particle tracking. *Experiments in Fluids*, 15:279–294, 1993.

[51] C. Mannaris and M. Averkiou. Investigation of microbubble response to long pulses used in ultrasound-enhanced drug delivery. *Ultrasound in Medicine and Biology*, 38: 681–691, 2012.

[52] T. J. Matula, S. M. Cordry, R. A. Roy, and L. A. Crum. Bjerknes force and bubble levitation under single-bubble sonoluminescence conditions. *The Journal of the Acoustical Society of America*, 102:1522–1527, 1997.

[53] S. Meagher, T. L. Poepping, K. V. Ramnarine, R. A. Black, and P. R. Hoskins. Anatomical flow phantoms of the nonplanar carotid bifurcation, Part II: Experimental validation with Doppler ultrasound. *Ultrasound in Medicine and Biology*, 2007.

[54] M. Minnaert. On musical air-bubbles and sounds of running water. *The London, Edinburgh, and Dublin Philosophical Magazine and Journal of Science*, 16:235–248, 1933.

[55] C. Molina, M. Ribo, M. Rubiera, J. Montaner, E. Santamarina, D. Raquel, J. Arenillas, R. Huertas, F. Purroy, P. Delgado, and A. José. Microbubble administration accelerates clot lysis during continuous 2-MHz ultrasound monitoring in stroke patients treated with intravenous tissue plasminogen activator. *Stroke*, 37(2):425–429, 2006.

[56] K. Namdee, A. J. Thompson, P. Charoenphol, and O. Eniola-Adefeso. Margination propensity of vascular-targeted spheres from blood flow in a microfluidic model of human microvessels. *Langmuir*, 29:2530–2535, 2013.

[57] E. Neppiras and B. Noltingk. Cavitation produced by ultrasonics: theoretical predictions for the onset of cavitation. *Proceedings of the Physical Society*, B64:1032–1038, 1951.

[58] T. T. Nguyen, Y. Biadillah, R. Mongrain, J. Brunette, J.-C. Tardif, and O. F. Bertrand. A Method for Matching the Refractive Index and Kinematic Viscosity of a Blood Analog for Flow Visualization in Hydraulic Cardiovascular Models. *Journal of Biomechanical Engineering*, 126(4):529, 2004.

[59] R. Ni, S. Kramel, N. T. Ouellette, and G. A. Voth. Measurements of the coupling between the tumbling of rods and the velocity gradient tensor in turbulence. *Journal of Fluid Mechanics*, 766:202–225, 2015.

[60] D. I. Nikitichev, A. Barburas, K. McPherson, J.-M. Mari, S. J. West, and A. E. Desjardins. Construction of 3-dimensional printed ultrasound phantoms with wall-less vessels. *Journal of Ultrasound in Medicine*, 35:1333–1339, 2016.

[61] B. Noltingk and E. Neppiras. Cavitation produced by ultrasonics. *Proceedings of the Physical Society*, B63:674–685, 1950.

[62] H. Oguz and A. Prosperetti. The natural frequency of oscillation of gas bubbles in tubes. *The Journal of the Acoustical Society of America*, 103(July 1997):3301–3308, 1998.

[63] K. Ohmi and H.-Y. Li. Particle-tracking velocimetry with new algorithms. *Measurement Science and Technology*, 11:603–616, 2000.

[64] *Tables of Acoustic Properties of Materials*. Onda Corporation, 2016. URL `http://www.ondacorp.com/tecref_acoustictable.shtml`.

[65] N. T. Ouellette, H. Xu, and E. Bodenschatz. A quantitative study of three-dimensional lagrangian particle tracking algorithms. *Experiments in Fluids*, 40(2):301–313, 2006.

[66] J. Owen, P. Grove, P. Rademeyer, and E. Stride. The influence of blood on targeted microbubbles. *Journal of the Royal Society Interface*, 11:20140622, 2014.

[67] N. A. Pelekasis, A. Gaki, A. Doinikov, and J. A. Tsamopoulos. Secondary bjerknes forces between two bubbles and the phenomenon of acoustic streamers. *Journal of Fluid Mechanics*, 500:313–347, 2004.

[68] E. Perlman, R. Burns, Y. Li, and C. Meneveau. Data exploration of turbulence simulations using a database cluster. In *SC '07: Proceedings of the 2007 ACM/IEEE Conference on Supercomputing*, pages 1–11, November 2007. doi: 10.1145/1362622.1362654.

[69] N. Phansalkar, S. More, A. Sabale, and M. Joshi. Adaptive local thresholding for detection of nuclei in diversity stained cytology images. In *2011 International Conference on Communications and Signal Processing*, pages 218–220, 2011.

[70] M. Plesset. The dynamics of cavitation bubbles. *Journal of Applied Mechanics*, 16: 277–282, 1949.

[71] T. L. Poepping, H. N. Nikolov, M. L. Thorne, and D. W. Holdsworth. A thin-walled carotid vessel phantom for Doppler ultrasound flow studies. *Ultrasound in Medicine and Biology*, 2004.

[72] H. Poritsky. The collapse or growth of a spherical bubble or cavity in a viscous fluid. *Proceedings of the First US National Congress on Applied Mathematics*, pages 813–821, 1952.

[73] A. Prosperetti, L. A. Crum, and K. W. Commander. Nonlinear bubble dynamics. *The Journal of the Acoustical Society of America*, 83:502–514, 1988.

[74] S. Qin and K. W. Ferrara. Acoustic response of compliable microvessels containing ultrasound contrast agents. *Physics in Medicine and Biology*, 51(20):5065–88, Oct. 2006.

[75] L. Rayleigh. On the pressure developed in a liquid during the collapse of a spherical cavity. *The London, Edinburgh, and Dublin Philosophical Magazine and Journal of Science*, 34:94–98, 1917.

[76] E. Sassaroli and K. Hynynen. Resonance frequency of microbubbles in small blood vessels: a numerical study. *Physics in Medicine and Biology*, 50(22):5293–305, Nov. 2005.

[77] J. Sauvola and M. Pietikäinen. Adaptive document image binarization. *Pattern Recognition*, 33(2):225–236, 2000.

[78] D. Schanz, S. Gesemann, and A. Schröder. Shake-the-box: Lagrangian particle tracking at high particle image densities. *Experiments in Fluids*, 57:70, 2016.

[79] T. Segers and M. Versluis. Acoustic bubble sorting for ultrasound contrast agent enrichment. *Lab on a Chip*, 14:1705–1714, 2014.

[80] E. Sheiner, J. Freeman, and J. Abramowicz. Acoustic output as measured by mechanical and thermal indices during routine obstetric ultrasound examinations. *Journal of Ultrasound in Medicine*, 24(12):1665–1670, 2005.

[81] P. C. Sontum. Physicochemical characteristics of sonazoid^{TM}, a new contrast agent for ultrasound imaging. *Ultrasound in Medicine and Biology*, 34:824–833, 2008.

[82] N. Stelzenmuller, J. I. Polanco, L. Vignal, I. Vinkovic, and N. Mordant. Lagrangian acceleration statistics in a turbulent channel flow. *Physical Review Fluids*, 2:054602, 2017.

[83] D. S. S.V. Pantankar, V.S. Pratap. Prediction of turbulent flow in curved pipes. *Journal of Fluids Mechanics*, 67:583–595, 1975.

[84] M.-L. D. Temmerman, H. Dewitte, R. E. Vandenbroucke, B. Lucas, C. Libert, J. Demeester, S. C. D. Smedt, I. Lentacker, and J. Rejman. mrna-lipoplex loaded microbubble contrast agents for ultrasound-assisted transfection of dendritic cells. *Biomaterials*, 32: 9128–9135, 2011.

[85] F. Toschi and E. Bodenschatz. Lagrangian properties of particles in turbulence. *Annual Review of Fluid Mechanics*, 41:375–404, 2009.

[86] E. Unger, T. Porter, W. Culp, R. Labell, T. Matsunaga, and R. Zutshi. Therapeutic applications of lipid-coated microbubbles. *Advanced Drug Delivery Reviews*, 56(9):1291–1314, 2004.

[87] G. A. Voth and A. Soldati. Anisotropic particles in turbulence. *Annual Review of Fluid Mechanics*, 49:249–276, 2017.

[88] G. A. Voth, A. L. Porta, A. M. Crawford, J. Alexander, and E. Bodenschatz. Measurement of particle accelerations in fully developed turbulence. *Journal of Fluid Mechanics*, 469:121–160, 2002. doi: 10.1017/S0022112002001842.

[89] J. Willneff. *A Spatio-Temporal Matching Algorithm for 3D Particle Tracking Velocimetry*. PhD thesis, Swiss Federal Institute of Technology Zurich, 2003.

[90] H. Xu, M. Bourgoin, N. T. Ouellette, and E. Bodenschatz. High order lagrangian velocity statistics in turbulence. *Physics Review Letters*, 96:024503, 2006.

[91] H. Yu, K. Kanov, E. Perlman, J. Graham, E. Frederix, R. Burns, A. Szalay, G. Eyink, and C. Meneveau. Studying lagrangian dynamics of turbulence using on-demand fluid particle tracking in a public turbulence database. *Journal of Turbulence*, 13:12, 2012.

[92] K. Zell, J. Sperl, M. Vogel, R. Niessner, and C. Haisch. Acoustical properties of selected tissue phantom materials for ultrasound imaging. *Physics in Medicine and Biology*, 52: N475–N484, 2007.